DISSERTATION

submitted to the

Combined Faculty of Natural Sciences and Mathematics
of the Ruperto-Carola-University of Heidelberg, Germany

for the degree of

Doctor of Natural Sciences

Put forward by
Sofía, Rojas-Ruiz
born in: Bogotá D.C., Colombia
Oral examination: June 28,th 2023

ACCRETING SUPERMASSIVE BLACK HOLES IN THE FIRST BILLION YEARS: IMPACT ON THEIR ENVIRONMENTS FROM PARSECS TO MEGAPARSECS

Referees: Prof. Dr. Jochen Heidt
Dr. Nadine Neumayer

ABSTRACT

Studying the environments of quasars in the first Gyr of the universe, or at $z > 5.5$, is crucial to understand their growth and evolution from such early times. These massive quasars with $\sim 10^8 - 10^9$ $M_\odot$ black holes are predicted to be born in the most massive halos of the underlying dark matter distribution and thus would be immersed in protoclusters of galaxies. However, the impact of a quasar's powerful radiation on the formation and growth of galaxies in its Mpc-scale environment is still debated observationally. Additionally, the different components contributing to the quasar activity from subpc- to kpc-scales can affect the gas and dust used to form stars in its host galaxy, thus impacting the black hole–host galaxy co-evolution. This thesis aims at providing more understanding of the different scales of quasar environments by investigating two exemplary quasars. We investigated the luminous quasar ULAS J1342+0928 at $z = 7.54$ and looked for galaxies in its $\sim 1\,\mathrm{pMpc}^2$ environment. We found one UV-bright Lyman-break galaxy candidate in addition to a [C II]-emitter associated with the quasar environment and clustered within a projected distance of $\lesssim 220\,\mathrm{pkpc}$ from the quasar. Future observations in the near-IR and mm would be necessary to confirm the redshift and physical properties of these galaxies and assess the number density of one of the earliest quasar large-scale environments yet explored. We also studied extensively the radio-loud quasar P352–15 at $z = 5.832$; the only source found thus far with evidence of a kpc-scale extended jet. Thus, this quasar is the ideal laboratory to investigate the first stages of black hole–jet–host galaxy co-evolution. We first studied the cold dust and [C II] gas of the host galaxy of P352–15 to explore whether the jet presence affects the host galaxy properties. The results on the inferred star formation rate and far-infrared luminosity were found to be comparable to studies on the radio-quiet quasar population. However, we found evidence of a spectral break in the jet synchrotron emission affecting the cold dust emission of the host galaxy. We further investigated the effect of the synchrotron spectral break by requesting additional Karl G. Jansky Very Large Array (VLA) radio observations. Using these new data, we found the frequency of the spectral break, we were able to calculate the jet age since its time of launch. We compared this jet timescale to the quasar lifetime, or the time since the last black hole accretion event. Both timescales were found to be comparatively young of just $\lesssim 10^4$ yrs within their uncertainties, evidencing a fairly recent quasar activity of P352–15. The work in this thesis shows that studying different scales of quasar environments at $z \gtrsim 6$ is essential to understanding the formation and evolution of galaxies and black holes in the early universe.

ZUSAMMENFASSUNG

Die Untersuchung der Umgebung von Quasaren in den ersten Gyr des Universums oder bei $z > 5,5$ ist von entscheidender Bedeutung für das Verständnis ihres Wachstums und ihrer Entwicklung in solch frühen Zeiten. Man geht davon aus, dass diese massereichen Quasare mit $\sim 10^8 - 10^9$ $M_\odot$ schwarzen Löchern in den massereichsten Halos der zugrundeliegenden dunklen Materieverteilung geboren werden und somit in Protoclustern von Galaxien eingebettet sind. Die Auswirkungen der starken Strahlung eines Quasars auf die Entstehung und das Wachstum von Galaxien in seiner Umgebung auf der Mpc-Skala sind jedoch immer noch Gegenstand von Beobachtungsdiskussionen. Darüber hinaus können die verschiedenen Komponenten, die zur Quasaraktivität von subpc- bis kpc-Skalen beitragen, das Gas und den Staub beeinflussen, aus denen sich in der Wirtsgalaxie Sterne bilden, und somit die Koevolution zwischen Schwarzem Loch und Wirtsgalaxie beeinflussen. Diese Arbeit zielt darauf ab, ein besseres Verständnis für die verschiedenen Skalen der Quasarumgebungen zu erlangen, indem zwei exemplarische Quasare untersucht werden. Wir untersuchten den leuchtenden Quasar ULAS J1342+0928 bei $z = 7,54$ und suchten nach Galaxien in seiner $\sim 1\,\mathrm{pMpc}^2$ Umgebung. Wir fanden einen UV-hellen Lyman-Break-Galaxienkandidaten zuätzlich zu einem [C II]-Emitter, der mit der Umgebung des Quasars assoziiert ist und in einer projizierten Entfernung von $\lesssim 220\,\mathrm{pkpc}$ vom Quasar gehäuft ist. Zukünftige Beobachtungen im nahen IR und im Millimeterbereich wären notwendig, um die Rotverschiebung und die physikalischen Eigenschaften dieser Galaxien zu bestätigen und die Anzahldichte einer der frühesten bisher erforschten Quasarumgebungen zu bestimmen. Wir haben auch den radioaktiven Quasar P352–15 bei $z = 5.832$ eingehend untersucht, die einzige bisher gefundene Quelle mit Anzeichen eines ausgedehnten Jets auf kpc-Ebene. Damit ist dieser Quasar das ideale Labor, um die ersten Stadien der Koevolution von Schwarzem Loch, Jet und Wirtsgalaxie zu untersuchen. Wir haben zunächst den kalten Staub und das [C II] Gas der Wirtsgalaxie von P352–15 untersucht, um herauszufinden, ob das Vorhandensein des Jets die Eigenschaften der Wirtsgalaxie beeinflusst. Die Ergebnisse bezüglich der Sternentstehungsrate und der Leuchtkraft im fernen Infrarot waren vergleichbar mit den Ergebnissen von Studien über die ruhige Quasar-Population. Wir fanden jedoch Hinweise auf einen spektralen Bruch in der Synchrotronemission des Jets, der die kalte Staubemission der Wirtsgalaxie beeinflusst. Wir haben die Auswirkung des Synchrotron-Spektrumsbruchs weiter untersucht, indem wir zusätzliche VLA-Radiobeobachtungen angefordert haben. Anhand dieser neuen Daten konnten wir die Frequenz des spektralen Bruchs bestimmen und das Alter des Jets seit seinem Start berechnen. Wir verglichen diese Jet-Zeitskala mit der Quasar-Lebensdauer bzw. der Zeit seit dem letzten Akkretionsereignis des Schwarzen Lochs. Beide Zeitskalen erwiesen sich mit nur $\lesssim 10^4$ yrs innerhalb ihrer Unsicherheiten als

vergleichsweise jung, was auf eine relativ junge Quasaraktivität von P352–15 hindeutet. Die Arbeit in dieser Dissertation zeigt, dass die Untersuchung verschiedener Skalen von Quasarumgebungen bei $z \gtrsim 6$ wesentlich für das Verständnis der Entstehung und Entwicklung von Galaxien und Schwarzen Löchern im frühen Universum ist.

Para mi familia y todos los niños de Colombia que sueñan en grande y echan pa' lante.

PUBLICATIONS

This thesis includes work from the following first-author publications:

Rojas-Ruiz, Sofía (2022). "The Role of Powerful Radio Jets in the Host Galaxy of a Quasar in the First Gyr of the Universe." In: *10.5281/zenodo.7104569*. Conference Name: Hypatia Colloquium.

Rojas-Ruiz, Sofía et al. (2021). "The Impact of Powerful Jets on the Far-infrared Emission of an Extreme Radio Quasar at z ~ 6." In: *ApJ* 920, p. 150. DOI: 10.3847/1538-4357/ac1a13.

Other first author publications are:

Rojas-Ruiz, Sofía et al. 2020. "Probing the Bright End of the Rest-frame Ultraviolet Luminosity Function at z = 8-10 with Hubble Pure-parallel Imaging", ApJ, 891, 146

Rojas-Ruiz, Sofía et al. 2023. "Exploring the Mpc Environment of the Quasar ULAS J1342+0928 at z = 7.54", Submitted to the AAS Journals.

ACKNOWLEDGMENTS

The pathway to completing this Ph.D. thesis has been possible thanks to the tremendous support from a lot of people I have met along the way.

I would like to firstly thank Eduardo Bañados and Fred Davies for giving me the opportunity of doing this Ph.D. and for opening the doors to the wonderful universe of high-z quasars. I greatly appreciate your trust in my scientific skills and your support thus far. I am grateful for learning so much from the knowledge and passion of everyone in the *high-z* group at MPIA. I thank Chiara Mazzucchelli for her encouragement and support in developing a lot of the work in this thesis. I would also like to thank Emmanuel Momjian for sharing his passion for radio astronomy with me. You have been the best radio mentor and colleague that I could have asked for. Your enthusiasm, hard work, and perspective have left an important mark on my working philosophy. Immense thanks to Steve Finkelstein for being my first supervisor and guide through my scientific career. You have always had faith in me and pushed me to become a better scientist and person, and for that, I will always be grateful. I would like to thank Rebecca Larson, you were the first astronomy student I met even before starting my undergraduate. You have been an amazing mentor, friend, colleague, and inspiration; I could not be more proud of you. I thank Nadine Neumayer for her support during my thesis and in difficult times during my stay in Heidelberg. Also would like to thank her and Jochen Heidt for advising my Ph.D. track during the past 4 years and now for agreeing to referee this thesis.

I could not be finishing this Ph.D. without all the amazing friends and colleagues I have been able to meet in Colombia, the U.S., and Germany. I would like to thank the RECA community; you made my Ph.D. more fun and helped me find purpose in teaching astronomy not only in Colombia but everywhere in the world. Learning astronomy is exciting, but sharing it with the world is a joyous gift. Special thanks to my family, who always believed in me even when my dream of becoming a Colombian astronomer seemed unattainable just 10 years ago.

Quiero reconocer especialmente el arduo trabajo de mi mamá Sandra y a mi papá Hernando para sacarme adelante y ser mis compañeros en esta travesía de la vida. Gracias a todos mis abuelos por criarme en un hogar humilde y amorso, por introducirme a la ciencia, la lectura y deliciosas recetas. Muchas gracias a mis tíos y tías que me han acogido y apoyado en diferentes momentos en los que tuve que trabajar mucho y sentir soledad por primera vez en un país extranjero. Gracias especiales a Tíjaro por ser el mejor amigo por tantos años y apoyarme en los momentos más difíciles sin importar la distancia. Finalmente, agradezco haber tenido una amiga del alma como Paula que me introdujo desde pequeña al mundo de las matemáticas y me enseñó la importancia de vivir alegre y sencilla por este paso que es la vida.

CONTENTS

LIST OF FIGURES

LIST OF TABLES

ACRONYMS

AGN Active Galactic Nuclei

ALLWISE the Wide-field Infrared Survey Explorer

ALMA Atacama Large Millimeter/sub-millimeter Array

CANDELS Cosmic Assembly Near-Infrared Deep Extragalactic Legacy Survey

BLR broad line region

CMB Cosmic Microwave Background

DECaLS the DECam Legacy Survey

DLA Damped Lyα

ESU elctrostatic units

FIR Far-Infrared

GMRT Giant Metrewave Radio Telescope
HST Hubble Space Telescope
IGM intergalactic medium
ISM interstellar medium
IRAM Institut de radioastronomie millimétrique
JWST James Webb Space Telescope
LAE Lyman ALpha Emitter
LBG Lyman-Break Galaxy
LLS Lyman limit System
MBB Modified Black Body
MWA Murchison Widefield Array
NOEMA IRAM NOrthern Extended Millimeter Array
NRAO National Radio Astronomy Observatory
PAN-STARRS1 Panoramic Survey Telescope & Rapid Response System 1
PCA principal component analysis
PWV precipitable water vapor
SED Spectal Energy Distribution
SMBH Super Massive Black Hole
STScI Space Telescope Science Institute
UKIDSS the United Kingdom Infrared Telescope Infrared Deep Sky Survey
VLA Karl G. Jansky Very Large Array
VLBA Very Long Baseline Array
VLT Very Large Telescope

1

INTRODUCTION

This thesis presents recent work in one of the most active fields of modern cosmology: the first galaxies and quasars born in the universe, their properties, and their role in the epoch of reionization. In order to understand the importance of studying this field and contextualizing this work with the different methodologies and historical background, it is necessary to first introduce the current standard cosmological model. We will then take on a cosmic voyage and focus on the times from the Big Bang to the first billion years of the universe. At this time, our primitive universe is going through its first evolutionary stages when the first stars, galaxies, and AGN begin to form and evolve.

Some of the most curious objects that have been observed within the first Gyr of the universe are Super Massive Black Hole (SMBH)s of $M_{BH} \sim 10^8 - 10^9 M_\odot$, which we call quasars. The existence of these massive and bright sources in the early universe provokes a lot of big questions: How common are these quasars? What are the environmental conditions in which they form? How can such a massive black hole form in the universe when just the first galaxy structures are assembling? Do these black holes have jets, how powerful are these and do they affect galaxy growth? These are some of the questions we explore in this thesis.

This thesis is organized in the following order: This current section serves as an introduction to cosmological concepts, the history of the universe, and the science we aim to explore in the work of the next few chapters. Then, we will first focus in Chapter 2 on studying the environment of one of the earliest quasars known in the universe, ULAS J1342+0928 present within the first ~ 700 Myrs of the universe. Thus, we will introduce quasar environments and their relationship to protoclusters from a theoretical and observational point of view. Later on, we will concentrate on a subcategory of quasars observed within the first billion years of the universe that are bright in radio wavelengths, where the synchrotron emission from the jet is observed. We present recent studies on the host galaxy of the radio-loud quasar P352–15 in Chapter 3. We then explore the age of the jet and quasar lifetime of P352–15 in Chapter 4. Finally Chapter 5 presents a summary from the work in this thesis.

* This Chapter has sections partly based on work from Rojas-Ruiz et al. (2021) and two works of Rojas-Ruiz, S et al. 2022 submitted and to be submitted to the *Astrophysical Journal*.

1.1 THE STANDARD COSMOLOGICAL MODEL

This section is inspired by the works from Peebles (1993) and Ryden (2003).

1.1.1 *Principles of Cosmology and Hubble-Lemaître Law*

Modern cosmology describes the large-scale structure and evolution of the universe based on the principle that the universe can be considered as homogeneous and isotropic on scales of roughly $> 100\,\mathrm{Mpc}$. This cosmological principle allows us to incorporate Einstein's theory of general relativity, which provides a framework for understanding the behavior of gravity. As a result, Einstein was able to make a model that describes the curvature of space-time related to the distribution of matter and energy in the universe from the *field equations*. In particular, the equations predict that the universe should either be expanding or contracting, depending on the distribution of matter and energy.

The universe is certainly expanding based on multiple observations showing that galaxies in the universe appear to be moving away from one another. In fact, the farther apart two galaxies are, the faster they are moving away from each other. This relationship is known as the Hubble-Lemaître Law where the recession velocity $v(t)$ is related to the distance at a given time $r(t)$ by the Hubble constant H_0:

$$H_0 = \frac{v(t)}{r(t)} \tag{1.1}$$

Different observations and methodologies have been applied to measure the Hubble constant H_0 such as using the distance ladder with Type Ia Supernovae or the tip of the red giant branch, measuring time delay among double imaged lensed quasars or from gravitational wave events, and more (e.g. Freedman et al., 2001; Birrer et al., 2019; Riess et al., 2021; Anand et al., 2022; Palmese et al., 2023). For all the works in this thesis, we assume H_0= 70 km s^{-1} Mpc^{-1}. From our local point of view, the light from distant galaxies is receding, meaning that the emitted light from a galaxy at a certain wavelength is redshifted towards longer wavelengths. Therefore, this cosmological redshift z allows the determination of the distance to a galaxy accounting for cosmic expansion, or *Hubble Flow*. In other words, the cosmological redshift is related to the scale at which the universe is expanding $a(t)$, or *scale factor* such that:

$$z = \frac{\lambda_o}{\lambda_e} - 1 = \frac{a(t_o)}{a(t_e)} - 1 \tag{1.2}$$

where $\lambda(t_o)$,$a(t_o)$ and $\lambda(t_e)$,$a(t_e)$ are the wavelength and *scale factor* at the time of observation and when the light from the galaxy is emitted, respectively. Since the time of observation is now, the scale factor $a(t_o) = 1$, simplifying this equation to:

$$1 + z = \frac{1}{a(t_e)} \tag{1.3}$$

The expansion of the universe is intimately connected to Einstein's field equations, the cornerstone of modern cosmology. These equations include the effects of dark matter and dark energy. Therefore, the expansion rate of the universe is related to the energy density of the universe, and the geometry, or curvature, of the universe. This relationship is expressed in the Friedman equation:

$$H^2 = \left(\frac{\dot{a}}{a}\right)^2 = \frac{8\pi G}{3}\rho - \frac{\kappa c^2}{a^2} + \frac{\Lambda c^2}{3} \tag{1.4}$$

where H is the Hubble parameter, G is the gravitational constant, ρ is the energy density of matter and radiation, a is the scale factor, κ is the spatial curvature of the universe, and Λ is the cosmological constant.

The Friedmann equation shows that the expansion rate is determined by the density of matter and energy in the universe. We can calculate the rate of change of the expansion rate of the universe from this equation and fluid dynamics such that the acceleration is described as:

$$\frac{\ddot{a}}{a} = -\frac{4\pi G}{3}(\rho + 3p) + \frac{\Lambda c^2}{3} \tag{1.5}$$

The acceleration equation takes into account the pressure of matter and radiation p, as well as the cosmological constant Λ and importantly the density ρ. This powerful equation shows that if the density ρ is high, the expansion rate will be slow and the universe will eventually collapse. On the other hand, if the density is low, the expansion rate will be fast and the universe will continue to expand indefinitely.

We can compare the density of the universe ρ to the current critical density of the universe from the Friedmann equation by setting $\Lambda = 0$ and accounting for the curvature of the universe. Recent studies have determined that the universe is flat, i.e. $k = 0$ (Planck Collaboration et al., 2020). Thus, rearranging the Friedmann equation, the critical density of the universe ρ_c is:

$$\rho_c = \frac{3H^2}{8\pi G} \tag{1.6}$$

The current value of the critical density within about 6% is $(1.28 \pm 0.08) \times 10^{11}$ $M_\odot$ Mpc^{-3}, which is equivalent to a density of one proton per 200 liters, and slightly higher than the mean energy density of the universe on 100 Mpc scales (Ryden, 2003). Knowing this and looking back at equation 1.5, the universe is expanding. Actually,

based on observations of supernovae explosions acting as standard candles to measure distances in the universe, it has been determined that the cosmos is actually expanding at an accelerated rate (Riess et al., 1998; Perlmutter et al., 1998). This accelerated expansion of the universe is ultimately caused by dark energy and is accounted for in the Friedmann equation with the cosmological constant Λ.

When adopting a cosmology for our studies, it is often useful to define a dimensionless density parameter by considering the mass density ratio of the universe from matter ρ_m, radiation ρ_r, and the cosmological constant energy density ρ_Λ to the current critical density of the cosmosρ_c:

$$\Omega_m = \frac{\rho_m}{\rho_c}; \quad \Omega_r = \frac{\rho_r}{\rho_c}; \quad \Omega_\Lambda = \frac{\rho_\Lambda}{\rho_c} \tag{1.7}$$

The sum of these density parameters represents the geometry of the universe:

$$\Omega_0 = \Omega_m + \Omega_r + \Omega_\Lambda; \quad \Omega_0 = 1 \quad \text{for a flat universe} \quad (k = 0) \tag{1.8}$$

The Friedmann equation can now be reformulated in terms of density parameters as:

$$H^2 = \left(\frac{\dot{a}}{a}\right)^2 = H_0^2 \left[\Omega_r a^{-4} + \Omega_m a^{-3} + \Omega_\Lambda \left(1 - \Omega_0\right) a^{-2}\right]. \tag{1.9}$$

This new expression shows the history of the universe divided into three main phases: a radiation-dominated era at very early times ($t < 47{,}000\,\text{yr}$), succeeded by a matter-dominated era ($47{,}000\,\text{yr} < t < 9.8\,\text{Gyr}$), and the present day dominated by the cosmological constant.

Integrating this Equation 1.9 provides an estimate of the age of the universe as a function of the scale factor:

$$t(a) = \frac{1}{H_0} \int_0^{a'} \left(\Omega_r a^{-2} + \Omega_m a^{-1} + (1 - \Omega_0) + \Omega_\Lambda a^2\right)^{1/2} da \tag{1.10}$$

Using the Friedmann equation from 1.4 we can find the density parameter for matter and dark energy in the present day. Considering that the current $\Omega_r = 10^{-14}$, it can be ignored:

$$\Omega_m = \frac{8\pi G \rho_0}{3H_0^2}; \quad \Omega_\Lambda = \frac{\Lambda c^2}{3H_0^2} \tag{1.11}$$

Re-organizing the Friedmann equation 1.4, assuming a flat geometry, ignoring Ω_r which does not dominate in the universe during the cosmic epochs we study in this thesis, and using the redshift–scale factor relationship from Equation 1.3, We can evaluate the Hubble parameter at a given redshift z in the following manner:

$$H(z) = H_0 \sqrt{\Omega_m (1+z)^3 + \Omega_\Lambda} \tag{1.12}$$

where z is the redshift at which we evaluate the Hubble parameter, Ω_m is the matter density parameter, Ω_Λ is the dark energy density parameter, and H_0 is the present-day value of the Hubble parameter.

Note: Given this brief introduction to the cosmological parameters, for the work presented in all the Chapters of this thesis we use the cosmology H_0= 70 km s^{-1} Mpc^{-1}, Ω_m= 0.3, Ω_Λ = 0.7. Using this cosmology, the $z = 7.5$ quasar we investigate in Chapter 2 is present when the universe was just 690 Myrs old, and for the quasar studied in Chapters 3-4 at $z = 5.8$, the universe was 948 Myrs. Finally, the universe today ($z = 0$) is 13.462 Gyrs.

1.1.2 *Cosmological Distances*

In this thesis, we focus on finding some of the first galaxies and quasars in the beginning of the universe and studying their physical properties. We have already established the definition of redshift that we use to measure the distance to these distant objects. However, we also often measure for instance the spatial distance between two sources at high redshift, their angular appearance, and luminosity. Thus, we need to introduce other metric systems often use in cosmology and in this work associated with redshift and accounting for the expansion of the universe.

PROPER DISTANCE Let us imagine two galaxies recently formed in the early universe and that we are interested in measuring their spatial distance (d) at the time (t) we are observing them. Therefore, their proper distance $d_p(t)$ is the length of the spatial geodesic between the two galaxies at a fixed scale factor $a(t)$. However, the universe is not static but rather is expanding, therefore this distance will change over time.

COMOVING DISTANCE We often need to compare the properties of objects at different distances and times in the history of the universe. The comoving distance d_c provides a consistent measure of distance that is not affected by the expansion of the universe. It represents the proper distance d_p between e.g. two galaxies at a given time, corrected for the expansion of the universe since the time of their separation.

$$d_c = a(t_0) \int_{t_e}^{t_0} \frac{c\,dt}{a(t)}; \quad d_c = \frac{d_p}{a(t)} = d_p(1+z) \tag{1.13}$$

where d_c is the comoving distance between our two galaxies, $a(t)$ is the scale factor at time t, t_e is the time of emission of the light from the distant object, and t_0 is the present time. The integral term represents the proper distance between the objects at the time of emission, which is corrected for the expansion of the universe by multiplying by the scale factor at the present time. Notice that at

the current time when $a(t_0) = 1$, the comoving and proper distance are the same.

LUMINOSITY DISTANCE In order to measure cosmological distances, for instance to a faraway galaxy, we need to rely on the object's intrinsic properties. Using our telescope we can observe the flux f of the galaxy which integrated over all frequencies gives the bolometric flux S, and using the bolometric luminosity L of the object, we obtain the function for luminosity distance as:

$$d_L = (\frac{L}{4\pi S})^{1/2} = d_c(1+z) = d_p(1+z)^2 \tag{1.14}$$

We can compute the intrinsic luminosities L of Type Ia Supernovae and therefore these are excellent standard candles to calculate distances in the cosmos (e.g. Riess et al., 1998; Perlmutter et al., 1998)

ANGULAR DIAMETER DISTANCE We observe distant galaxies with telescopes and thus measure their angular sizes or separation. It is necessary to convert these measurements from the images to the proper scales of the galaxy. This conversion can be achieved with the angular diameter distance d_A such that for a given galaxy of diameter ℓ observed at an angular distance δ_θ:

$$d_A = \frac{\ell}{\delta_\theta} \tag{1.15}$$

The angular diameter distance is related to the comoving distance such that:

$$d_A = \frac{d_c}{(1+z)} \tag{1.16}$$

Taking the limit $z \to 0$ for the resulting expression of Equation 1.16 for $z << 1$, results in $d_A \approx d_L \approx d_p(t_0)$. However, when $z \to \infty$, or at higher redshifts, d_A approaches zero.

The evolution towards higher redshifts is slow and thus the effect is not greatly noticeable. For instance, for the works described in Chapters 2-4 1" corresponds to 4.99 and 5.8 proper-kpc at $z = 7.5$ and $z = 5.83$, respectively.

1.2 A COSMIC VOYAGE

It all started with the Big Bang about 13.8 Gyrs ago, and ever since the universe has gone through major evolutionary stages (see Figure 1.1) briefly described here. In the beginning, the universe was highly energetic and dense but then at $t_{age} \sim 10^{-36}$ sec. the universe experienced an exponential expansion ending at around $t_{age} \sim 10^{-33}$ sec. at which point the universe supercooled by more than 28 orders of magnitude. This phase transition is known as the *inflationary theory* and is the most accepted theory

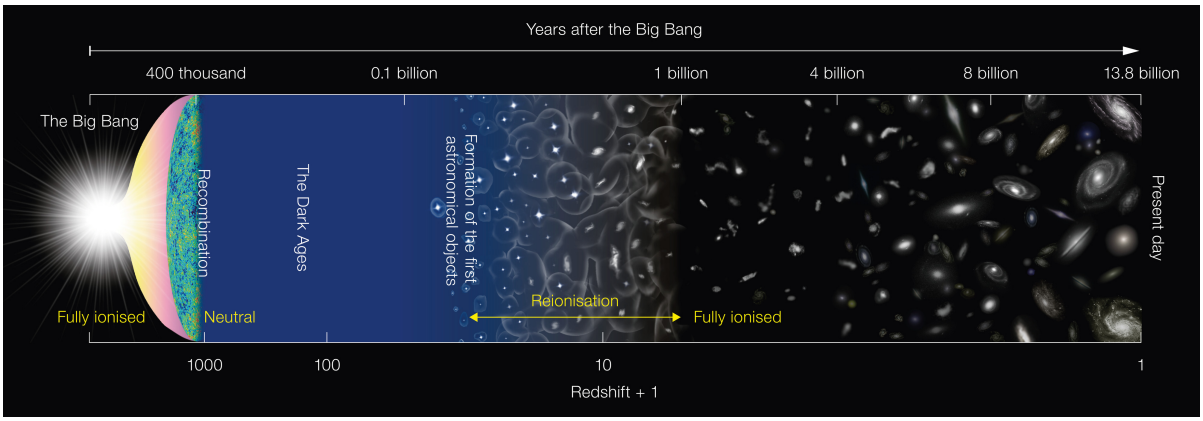

Figure 1.1: This illustration presents the major evolutionary stages in the history of the universe. This thesis focuses on studying galaxies and quasars in the Epoch of Reionization. Credits: NAOJ.

so far that explains the flatness of the universe we observe, and that all regions, even the causally disconnected ones, are observed to be at the same temperature (Guth, 1981). The universe continues to expand at a slower pace and the strong force allows the first photons, electrons, neutrinos, protons, and neutrons to exist.

As the universe is expanding and cooling down, the photons, baryons, and electrons that had been interacting freely are slowing down. Thus, the first elements begin to form at $t_{age} \sim 200 - 1200\,sec.$; mainly hydrogen (H, ^{2}H, ^{3}H), Helium (^{3}He, ^{4}He), and traces of Lithium (^{7}Li) and Beryllium (^{7}Be) during the *Big Bang Nucleosynthesis* (Alpher, Bethe, and Gamow, 1948). The universe so far has been radiation dominated, until $z \sim 3500$ when it reached matter-radiation equality. Soon after, the universe became matter-dominated but it is not until *recombination* at $z \sim 1,100$ or $t_{age} \sim 380,000\,yrs$ that hydrogen recombines, photons decouple and we can see the last scattering surface imprinted in the Cosmic Microwave Background (CMB) (Penzias and Wilson, 1965). Primordial density perturbations in the early universe have produced an inhomogeneous CMB. Fluctuations in the CMB can constrain the geometry, age, and size of the universe (Planck Collaboration et al., 2020), and evidence for dark matter. This is as far back as we have been able to observe with our telescopes and is thus the earliest laboratory we have. However, current efforts are aiming to identify perturbations on smaller scales than what has been probed so far, probing times as early as $\sim 10^{-14}\,sec$. This can be achieved through analysis of gravitational wave signals in the millihertz regime (Biscoveanu et al., 2020). Future observatories would be able to achieve these frequencies at an optimal sensitivity (e.g., LIGO and LISA Ligo Collaboration et al., 2015; Amaro-Seoane et al., 2023).

The period of the *dark ages* followed when small primordial density perturbations are accentuated under the effect of gravity, eventually leading to the formation of dark matter halos in a web-like framework, forming the backbone of the large-scale structure. The remaining baryonic matter fell into the potential well of these dark matter halos, forming clouds predominantly of hydrogen that collapsed and formed the first stars at $z \sim 30$, $\sim 100Myrs$. This first generation of stars, referred to as Pop

III, were extremely massive sources of UV-radiation ($\gtrsim 100-200 M_\odot$ Bromm, Coppi, and Larson, 1999; Abel, Bryan, and Norman, 2000; Klessen and Glover, 2023). They were short-lived (tens of Myr) and quickly enriched their environment with the first elements heavier than hydrogen/helium, referred to as metals. Stars with heavier elements formed, and the first galaxies began to assemble. These primitive galaxies were powerful sources of UV radiation that began to ionize their surrounding medium in bubble-like structures. Thus, the intergalactic medium (IGM) started to get ionized and the universe began to enter the last major phase transition called the *epoch of reionization*.

It is not entirely certain from which age *reionization* begins or ends, but is approximately $z \sim 15-5.5$ or $t_{age} \sim 250\,\mathrm{Myrs} - 1\,\mathrm{Gyr}$ (e.g. Bosman et al., 2022). The evolution and the sources responsible for this era are one of the most active research areas in astronomy (see e.g. Loeb and Barkana, 2001; Fan et al., 2006; McQuinn, 2016; Namikawa, 2018). During this time we find galaxies of all masses, and some of them are even capable of hosting AGN with $M_{BH} \sim 10^6 M_\odot$ as early as $z = 8.68$ or $\sim 570\,\mathrm{Myrs}$ from recent observations (Larson et al., 2023). These AGN are progenitors of the first SMBH of $M_{BH} \sim 10^8 M_\odot$, or quasars, thus far known to be present at $z \sim 7.5$ or $t_{age} \sim 680\,\mathrm{Myrs}$, and they are the protagonists in this thesis.

After reionization ends, the universe continued to expand and galaxies continued evolving through the peak of star formation and quasar activity occurs at $z \sim 2$ or $t_{age} \sim 3.2\,\mathrm{Gyrs}$ (Madau and Dickinson, 2014). Later at $z = 0.3$ or $t_{age} \sim 10\,\mathrm{Gyrs}$ the universe became dark energy-dominated and the universe's expansion began to accelerate exponentially all the way to today at $z = 0$, and we expect this accelerated expansion to continue into the cosmic future.

1.3 THE INTERGALACTIC MEDIUM DURING REIONIZATION

Hydrogen is the most abundant element in the early universe and is a major component in the first generation of stars. It is only natural to predict that the earliest galaxies, AGNs, and quasars similarly contain substantial amounts of hydrogen. Given the high redshift nature of these sources, the Lyman series is the bluest hydrogen spectral set of lines that one could observe. However, the neutral hydrogen gas in a galaxy, or the IGM along the line of sight can absorb photons with energy higher than the Lyα emission at $\lambda_{rest} = 1216\,\text{Å}$. This absorption effect appears in the spectrum of a bright galaxy or quasar as a forest of spikes at the wavelength of the redshifted Lyα transition of the intervening gas and is called the Lyα-forest (Lynds, 1971), see Figure 1.2. As we observe deeper into *reionization* times, the Lyα-forest becomes denser leaving only a small fraction of the intrinsic flux bluewards of Lyα, resulting in the "Gunn-Peterson" effect (Gunn and Peterson, 1965) (bottom panel in Figure 1.2). Since most of the emitting light from the galaxy or quasar that we observe is redward of $\lambda_{rest} = 1216\,\text{Å}$, we can calculate the distances to such high-redshift objects as:

$$z = \frac{\lambda_o}{1216\,\text{Å}} - 1,$$

where λ_o is the wavelength at which we begin to observe the light from the source.

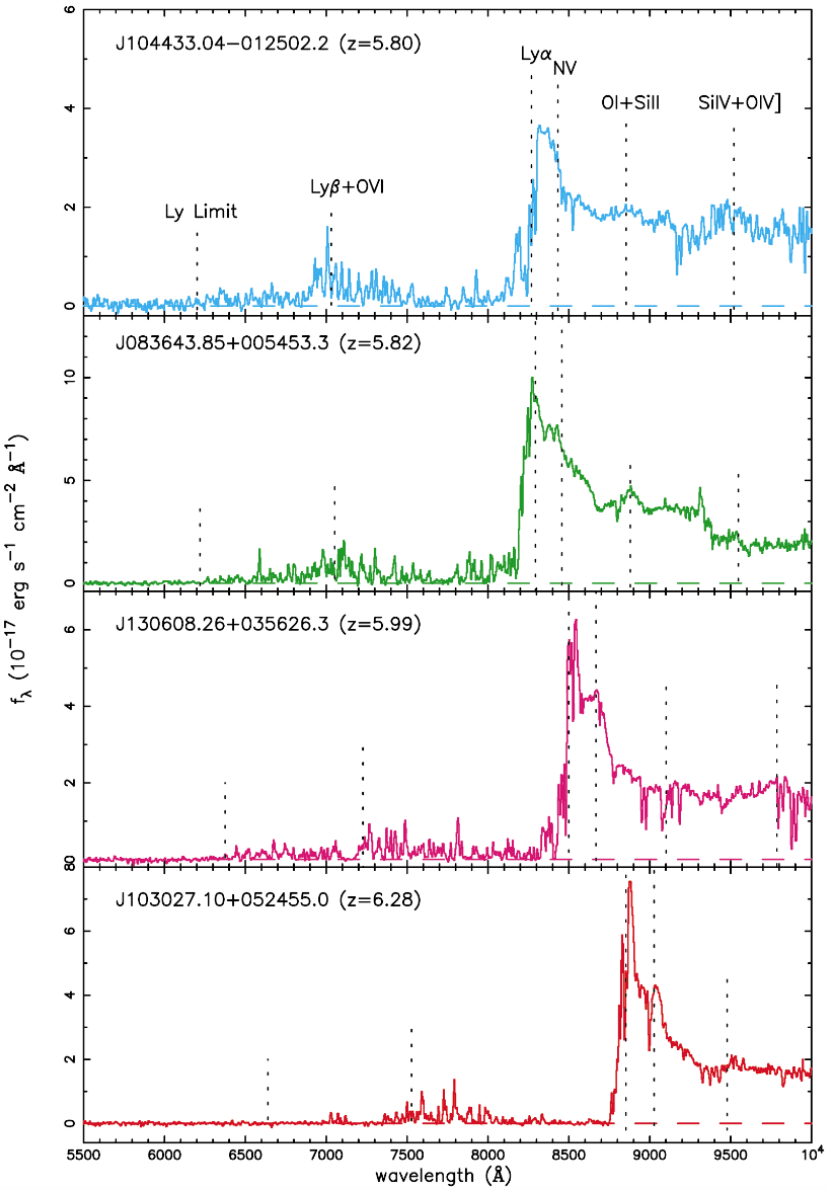

Figure 1.2: Example from Becker et al., 2001 showing the Lyα-forest in the spectra of quasars (three top panels), and the Gunn-Peterson trough (bottom panel). Closer to the epoch of reionization, when the density of hydrogen is higher, this trough is more evident.

Studying the Lyα-forest allows us to measure the density of neutral hydrogen up to a certain redshift $n_{\mathbf{HI}}(z)$. This experiment is possible when the ionizing source is powerful and the Lyα-forest is more visible, which is the case of quasars that often hold absolute AB magnitudes up to $M_{AB} \lesssim -23$ (Schmidt and Green, 1983). Thus, quasar spectra are often used to study the physics of the IGM and measure $n_{\mathbf{HI}}(z)$ at $2 < z < 6$ (e.g., Becker, Bolton, and Lidz, 2015; McQuinn, 2016; Simcoe et al., 2020, and references within). The observed Lyα-forest traces the density and opacity fluctuations of the IGM along the cosmic web at all the different cosmic epochs. Thus it is possible to see the evolution of the IGM gas with redshift. Specifically, we can

identify the redshift at which the neutral hydrogen in the IGM becomes ionized, i.e. the end of *reionization*. In the past 20 years, more quasar surveys have become available to more accurately constrain this measurement, and recent studies have pushed the end of cosmic reionization towards lower redshifts (from first identifications at $z \sim 6$ to now $z \sim 5.3$) (e.g. Becker et al., 2001; Bosman et al., 2022; Fan, Banados, and Simcoe, 2022).

1.4 FIRST GALAXIES

What did the first galaxies look like? In order to answer this question we need to be able to characterize some of these galaxies' properties such as their luminosity, mass, morphology, stellar population, and their ionizing fraction contributing to *reionization*. It is necessary to first find these high-redshift galaxies. They are much fainter than quasars ($M_{AB} \gtrsim -22$) and thus the Gunn-Peterson trough is not easily observed. Therefore, the spectrum of a high-redshift galaxy presents a clear-cut at the Lyα line. This signature is referred to as the Lyα-break and can be identified with photometry in consecutive filters and galaxies found with this method are called a Lyman-Break Galaxy (LBG). The method relies on identifying a region in a color-color space that is inhabited by galaxies at the redshift of interest (Steidel et al., 1996). This involves measuring the photometry of the galaxies in at least a pair of filters bracketing the Lyα-break to provide a red color, and a pair of filters just redward of the break to provide a blue color. A related method for finding these breaks involves fitting a suite of model template spectra to the observed SED of the galaxy candidate, finding the redshift for which the model fits best, known as photometric redshift fitting (see Figure 1.3). Both of these methods are explored in Chapter 2.

Studying the galaxies bright in rest-frame UV wavelengths ($-22 \lesssim M_{AB} \lesssim -19$) reveals the interplay of different physical processes responsible for star formation efficiencies such as supernovae and AGN feedback, dust attenuation, and the build-up of dark matter halos in the first evolutionary stages of galaxy formation (e.g., Somerville et al., 2008; Bower, Benson, and Crain, 2012; Finkelstein et al., 2012). The *Hubble Space Telescope (HST)* has been used to find UV-bright galaxy candidates at high redshift ($z \lesssim 11$, or $t_{age} \sim 400$ Myrs; Oesch et al., 2016; Jiang et al., 2020). Well-known examples are searches in deep fields such as the Cosmic Assembly Near-infrared Deep Extragalactic Legacy Survey (CANDELS), the Hubble Ultra Deep Field, and the Hubble Frontier Fields; but nearly all of the $z > 8$ galaxy candidates were selected from only a few *HST* filters covering the reddest bands (J and H), or even some robustly detected in only one filter (e.g., Coe et al., 2013; Oesch et al., 2013; Oesch et al., 2014; Bouwens et al., 2015; Bouwens et al., 2016; Bouwens et al., 2019; Bouwens et al., 2021; Finkelstein, 2016; Finkelstein et al., 2022).

Other strategies are pure parallel programs – where random field pointings result in completely independent, uncorrelated observations – providing an excellent opportunity to observe a population of rare bright sources that may not be fully sampled by deep surveys covering the same area in contiguous fields (e.g., Trenti and

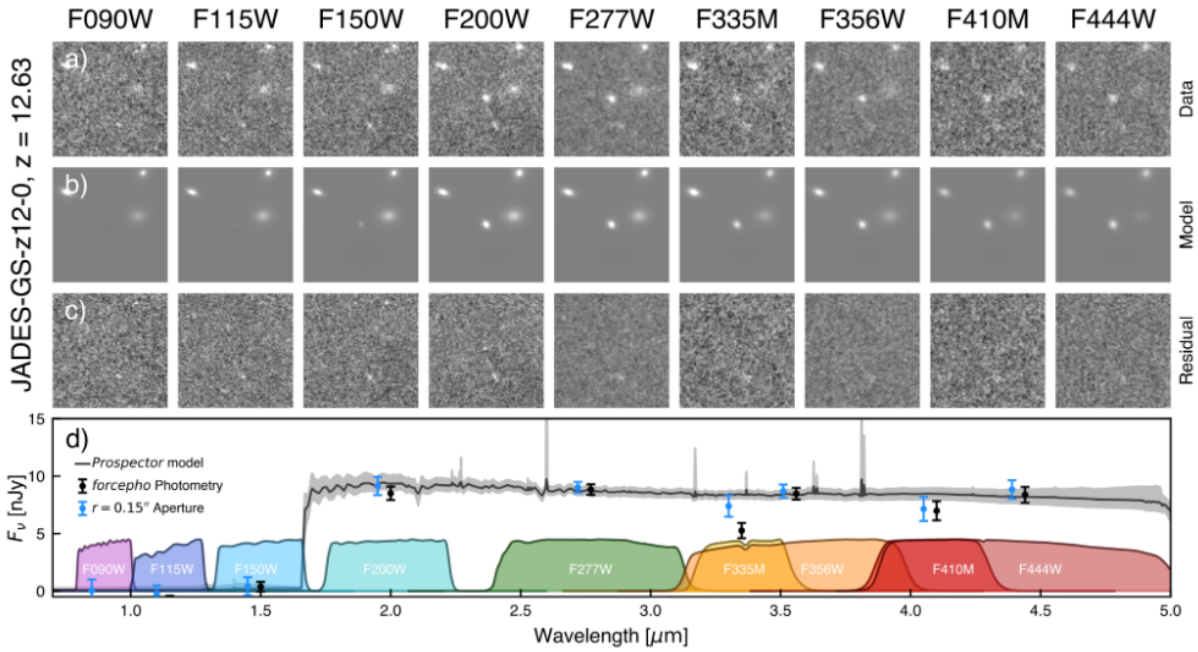

Figure 1.3: Example from (Robertson et al., 2022) of precision photometry and spectral energy distribution (SED) modeling of JADES–GS–z12–0 with photometric redshift $z_{\rm phot} = 12.90$. (a) Photometry in all *JWST*/NIRCam bands (b) Model reconstruction of the observations and (c) the slight residuals. The source fluxes are then used as constraints for SED fitting to the photometry (d). Note the Lyα-break from the best-fit SED model.

Stiavelli, 2008; Trenti et al., 2011; Bradley et al., 2012; Calvi et al., 2016; Morishita et al., 2018; Rojas-Ruiz et al., 2020; Roberts-Borsani et al., 2022; Bagley et al., 2022). Currently, the density of UV-bright galaxies is presently ill-constrained at $z > 8$ and it is imperative to find more bright galaxy candidates. *James Webb Space Telescope (JWST)* is now revealing a large fraction of high-z galaxy candidates and spectroscopically confirmed galaxies at $z > 8$ (see Figure 1.3, Robertson et al., 2022; Curtis-Lake et al., 2022).

All the strategies mentioned thus far focus on looking photometrically for the Lyα-break and then confirm the redshift of the galaxy by looking at its Lyα emission line from the galaxy (see Figure 1.4). However, photons at this wavelength are highly resonant as they try to escape the clumpy interstellar medium (ISM) of the galaxy (e.g., Hansen and Oh, 2006; Dijkstra and Loeb, 2008; Zheng et al., 2010). Thus, the Lyα emission line can often be absorbed completely. It becomes necessary to look for other characteristic lines from the galaxy that can be observed. Such is the case of strong nebular emission lines from massive stars in the galaxy; mainly [O II] $\lambda\lambda$3727,3729, Hβ (λ4861), and [O III] $\lambda\lambda$4959,5007 (e.g. Shapley et al., 2003; Erb et al., 2010; Ravindranath et al., 2020). These emission lines are now observable with *JWST*and have indeed revealed more galaxies at $z > 7$. Furthermore, we are now learning about their ionizing power through tests such as the ratio =O32 (e.g., Steidel et al. (2016)), crucial for studying *reionization*.

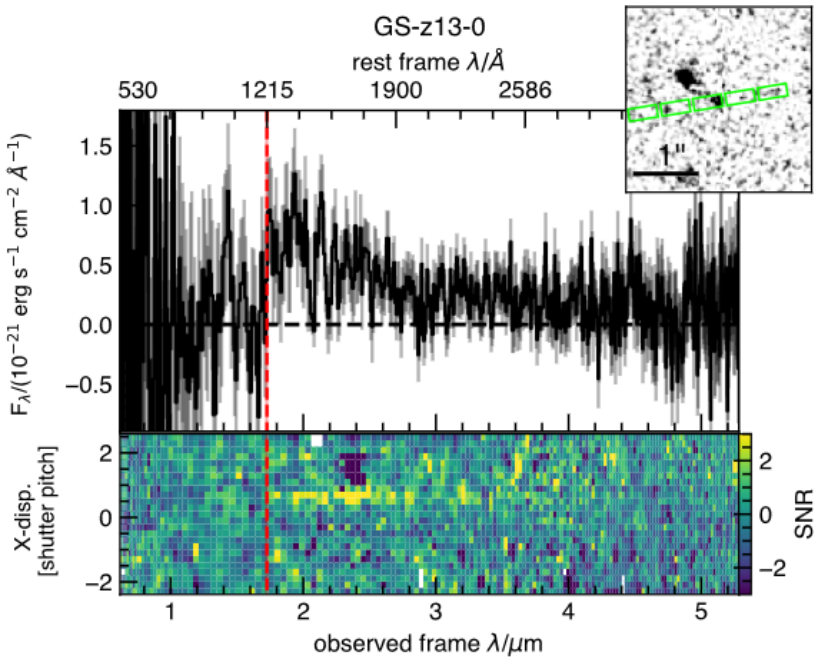

Figure 1.4: *JWST* NIRSpec prism spectrum at resolution R ~ 100 for JADES-GS-z13-0 (Curtis-Lake et al., 2022). At the top is the 1D spectrum has associated 1σ uncertainties. In the bottom panel is the 2D signal-to-noise ratio plot. The inset panel in the top right-hand corner shows the NIRCam F444W filter image with the three nodding positions of the NIRSpec micro-shutter 3-slitlet array aperture shown in green. The red dashed line shows the wavelength of rest-frame Lyα, showing also a clean break.

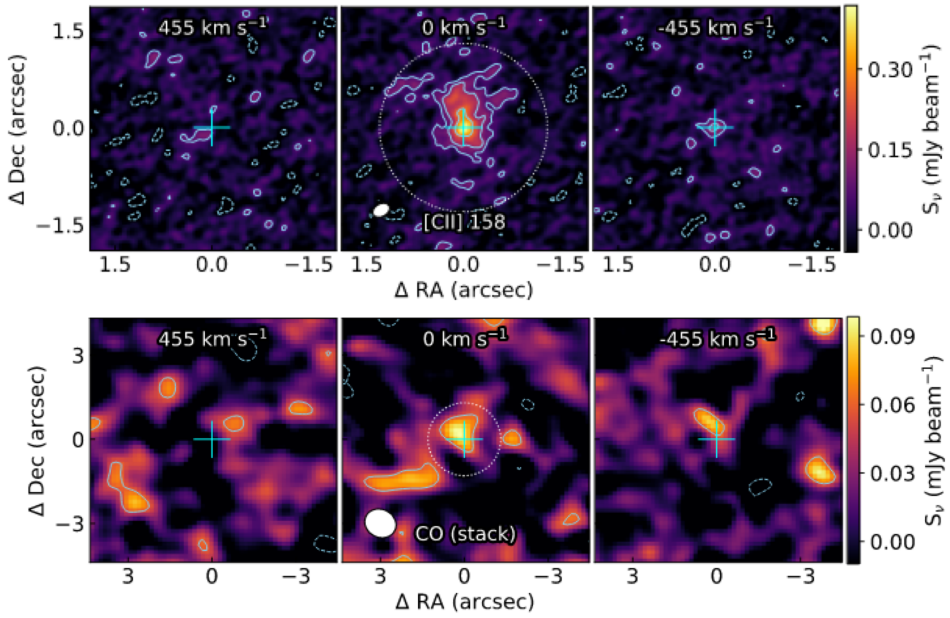

Figure 1.5: Cutouts of the host galaxy of quasar ULAS J1342+0928 observed with Atacama Large Millimeter/sub-millimeter Array (ALMA)showing the emission line in the central panel of [C II] (top), and a stack of CO (7–6), (8–7), (10–9), and (11–10) molecular emission lines (bottom). Figure adapted from Novak et al. (2019).

Alternatively, one can observe the cold gas and dust from the galaxy by observing at redder wavelengths. Such is the case of the [C II]-158μm fine-structure emission, which is the main coolant of the ISM and easily observable due to its high brightness compared to the rest of the galaxy's rest-frame Far-Infrared (FIR) emission (e.g., Wang et al., 2013; Herrera-Camus et al., 2015). This line allows to infer kinematics, star-formation properties and masses of the galaxy (see reviews from Carilli and Walter 2013; Díaz-Santos et al. 2017). Other good tracers of cool gas in galaxies are the different excitation levels of CO molecules, determined by the number of collisions with H_2 molecules, as they are very abundant, massive, and have a high cross-section (Carilli and Walter, 2013). Galaxies at $z \lesssim 8$ have all these emission lines redshifted to the sub-millimeter and thus can be observed with facilities like ALMA or IRAM NOrthern Extended Millimeter Array (NOEMA).

The redshift determination for high-redshift quasars is often non-trivial as winds produced from the black hole accretion often broaden, blue- or redshift emission lines coming from the source, as later seen in §1.5. Therefore, these molecular lines provide a systemic redshift z_{sys} for the quasar. Specifically, the CO (6–5) and CO (7–6) molecular lines are expected to be among the strongest CO transitions in galaxies hosting an AGN (e.g., Carilli and Walter, 2013). Furthermore, the study of these tracers in radio-loud AGN and quasars can reveal whether the jets are affecting the gas for star formation in the host galaxy. Similar cool gas tracers are explored for the radio-loud quasar P352–15 at $z = 5.83$ in Chapter 3.

1.5 QUASARS: THE ALL-TIME BRIGHTEST SOURCES

Quasars are the most luminous non-transient sources in the universe throughout all cosmic times (e.g. Fan, Banados, and Simcoe, 2022). They were first discovered as bright point-like radio emitters in the sky, similar to stars in brightness but at much larger distances. Thus, they received the original name of "quasi-stellar radio sources" (e.g. 3C 273 at $z = 0.16$, Hazard, Mackey, and Shimmins, 1963; Schmidt, 1963). Shortly after, more sources with similar spectral features in the rest-UV regime were identified but did not present strong radio emission (Sandage, 1965). Thus, it was determined that all these sources fall into the same category and were simply called "quasi-stellar objects", "QSOs", or *quasars*, as will continue to be referenced in this thesis.

Quasars' extreme surface brightness is due to the active SMBH of $M_{BH} \sim 10^{7-10}\,M_{\odot}$ at the center of the galaxy, making this object a type of AGN. The black hole accretion acts as a powerful engine emitting light at all wavelengths from radio to gamma-rays, as it swirls gas and dust from the host galaxy. Different physical mechanisms brighten the quasar at specific wavelengths of the electromagnetic spectrum. The viewing angle affects the observable characteristics of the quasar. The composition of a quasar can be summarized as follows:

The accretion disk emits large amounts of energy in the rest–frame UV/optical range as this is the material closest to the black hole that is being swirled in with a non-null angular momentum. The X-ray corona is a hot (10^7 K) region above and below the accretion disk. Further out and within a parsec (pc) from the black hole is the broad line region (BLR) composed of high-velocity gas "clouds", which are evidenced in the rest-frame UV/optical spectrum as broadened emission lines. Several pc out from the black hole, there is an obscuring dusty torus that absorbs part of the energy from the accretion disk and re-emits it in the infrared ($\lambda \sim 3\mu$m). At ~0.1 kpc scales a gas region moving at velocities of $\sim$ 300–500 km s^{-1} produces narrow emission lines in the UV/optical spectrum. At even larger kpc-scales, two (or one depending on the viewing angle) jets are generated by the material getting wrapped around the magnetic field from the accreting black hole, and that is ejected at relativistic speeds. Jets are thought to be a stage in the AGN/quasar evolution and are present in $\sim$ 10% of quasars that have been observed at all cosmic times. For decades, various observational and theoretical studies have worked towards a "unified model" of AGN and quasars to understand the observed emission from the different components (Antonucci, 1993; Urry and Padovani, 1995; Ramos Almeida and Ricci, 2017, e.g.). The different components of an AGN based on viewing angle, jet emission, black hole accretion rate, and spectral region of observed emission are presented in Figure 1.6.

Despite the complexity of AGN and quasar properties, this AGN unified model classification helps introduce the two quasars we investigate in this thesis. It is possible to see that quasars classify under the high electromagnetic power region, unsurprisingly as they host a SMBH (left top and bottom quadrants in Figure 1.6). Depending on the viewing angle, a division of radio-loud and radio-quiet quasars depends on the observability of a jet, which emits strongly in radio synchrotron radiation (more

description is offered in §1.7). Note that if the jet is pointed close to or directly to the line-of-sight the object is categorized as a “blazar". Finally, Type I and II quasars are classified depending on the observed emission from the BLR which is closest to the accretion disk, and is obscured for Type II quasars as the emission is absorbed by dust and gas in the torus.

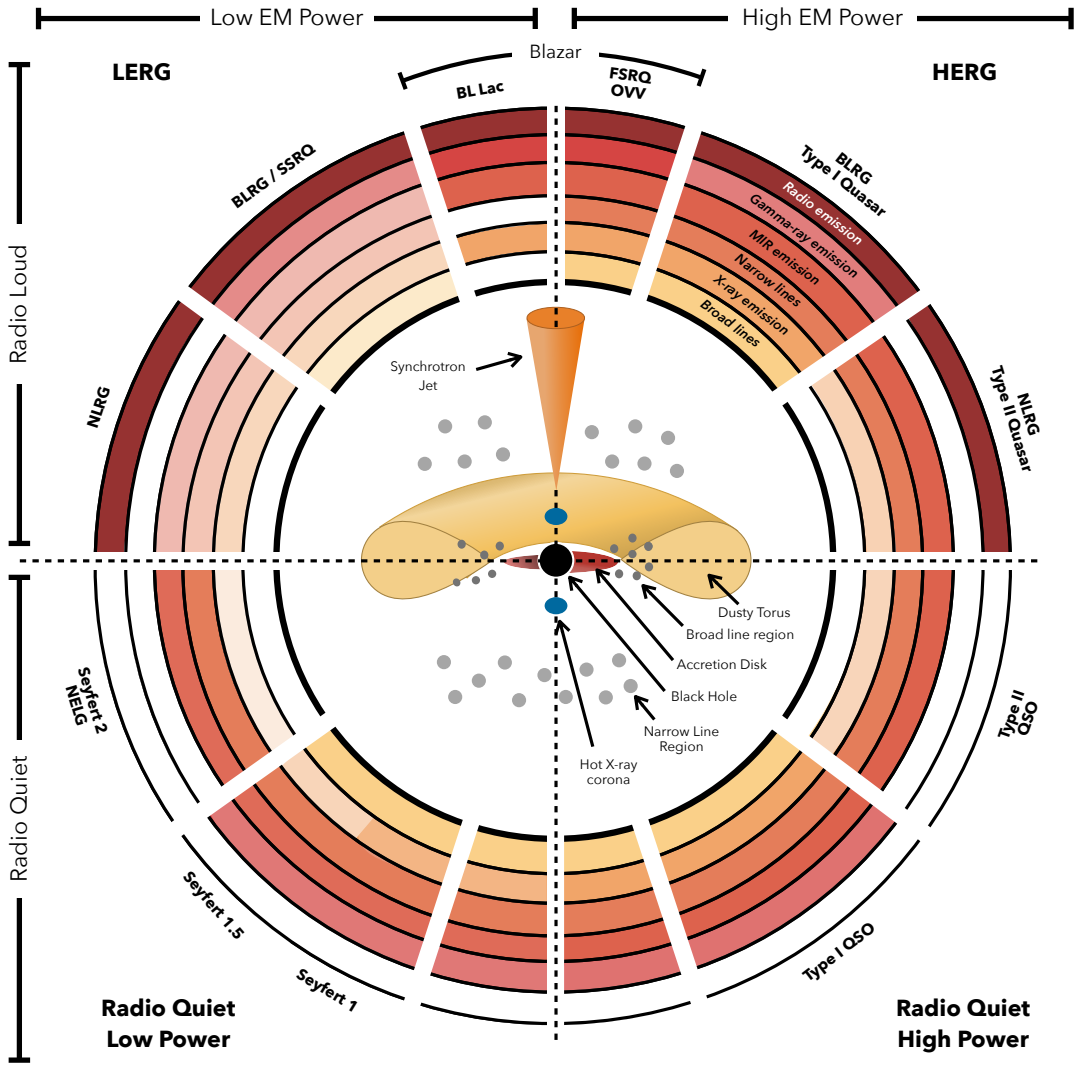

Figure 1.6: Schematic representation of our understanding of AGN in the orientation unified scheme. The type of object seen depends on the viewing angle, whether or not the AGN produces a significant jet (radio-loud or radio-quiet), and the rate of accretion onto the central SMBH (low or high electromagnetic power). Figure taken from Thorne et al. (2022b), see also Thorne et al. 2022a for references therein.

1.6 QUASAR LARGE-SCALE ENVIRONMENTS IN THE EARLY UNIVERSE

Quasars are noticeably rare sources in the early universe (~ 1 per Gpc^3 at $t_{age} < 1$ Gyr, Schindler et al., 2022). However, multiple observational search efforts during the past decade have revealed a significant (> 400) population of quasars in the epoch of reionization within the first billion years of the universe, at redshift $z > 5.5$ (e.g Venemans et al., 2013; Venemans et al., 2015; Bañados et al., 2016; Mazzucchelli et al., 2017b; Matsuoka et al., 2019; Reed et al., 2019; Yang et al., 2019; Gloudemans et al., 2022). These observations evidence a dramatic decline of the spatial density of luminous quasars at $z > 6$ and suggest that we are closing into the epoch when the first generation of SMBH emerged in the early universe (Wang et al., 2019a). The presence of these $\gtrsim 10^8$ SMBHs posits challenges on theories of black hole formation (e.g., Habouzit et al., 2016a; Habouzit et al., 2016b; Volonteri, Habouzit, and Colpi, 2021). Some of the leading black hole seed scenarios are shown in Figure 1.7 and briefly described here. As presented in Amaro-Seoane et al. (2023), black hole formation theory for $z > 6$ quasars points to the possibilities of the collapse of Pop III stars resulting in a black hole mass $M_{BH} \lesssim 10^3 M_\odot$, the collapse of Very Massive Stars formed through runaway collisions in compact stellar clusters ($10^3 M_\odot \lesssim M_{BH} \lesssim 10^4$ $M_\odot$), the collapse of Super Massive Stars ($M_{BH} \gtrsim 10^3 M_\odot$) and, the collapse of cosmological density perturbations (primordial BHs, $1 M_\odot \lesssim M_{BH} \lesssim 10^{10}$ $M_\odot$).

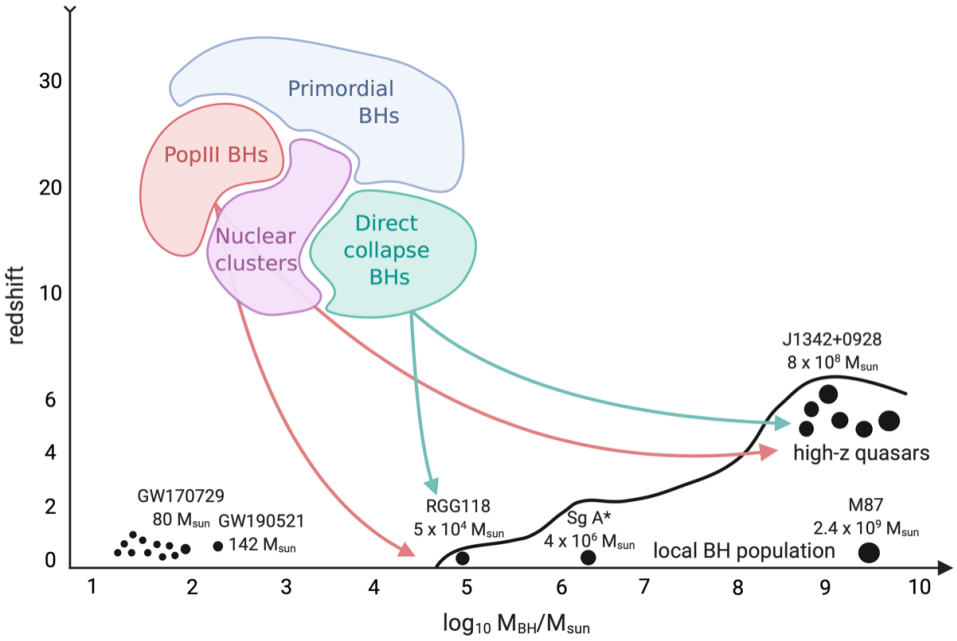

Figure 1.7: Illustration of the theoretical seeds for black hole formation resulting in a variety of black hole masses observed at different redshifts. Figure credit: Melanie Habouzit, for more reference see Figure 2.7 in Amaro-Seoane et al. (2023).

Similarly, the presence of these early SMBHs challenges large-scale structure assembly and clustering given that these systems are already formed and evolved in a short time by $z \sim 6$. For instance, finding quasar pairs would provide constraints on

black hole growth by accretion or by merger events (e.g., Greiner et al., 2021). Furthermore, quasars could affect the growth of galaxies in their surroundings through feedback in the environment such as UV-winds inhibiting star formation (e.g., Habouzit et al., 2019). To answer these open questions, it is crucial to observationally inspect the *Mpc-scale environments of quasars at the highest redshifts known*.

Only eight quasars are known at $z > 7$, and three are at $z > 7.5$, which is the current redshift frontier of SMBH research: J0313–1806 at $z = 7.64$ (Wang et al., 2021), J1342+0928 at $z = 7.54$ (Bañados et al., 2018b), and J1007+2115 at $z = 7.52$ (Yang et al., 2020). These early quasars are powered by $\gtrsim 10^8$ $M_\odot$ black holes (e.g Yang et al., 2021; Farina et al., 2022) and the large majority reside in galaxies with extremely large star formation rates ($> 100 - 1000$ $M_\odot$ /yr; e.g. Venemans et al. 2020). In order to sustain both the tremendous black hole growth and the intense star formation, current theoretical models posit that these systems lie in highly biased regions of the universe at that time, where gas can fragment and form a large number of surrounding galaxies (e.g. Springel et al., 2005; Volonteri and Rees, 2006; Costa et al., 2014). An overdensity can be traced by a larger number of surrounding galaxies with respect to an average blank field of view. These quasar environments could possibly host powerful sources of ionizing photons such as bright Lyman-α emitters or have nearby halos hosting these galaxies (Overzier et al., 2009). Consequently, these massive quasars are thought to be indicators of protoclusters which, as defined in Overzier (2016), are galaxy overdensities that will evolve by $z \sim 0$ into the most massive virialized clusters ($\geqslant 10^{14}$ $M_\odot$). Accordingly, studying the environment of quasars hosting SMBHs as early as at $z \sim 7.5$ is crucial to understand the large-scale structure and the feeding of the first massive galaxies and black holes in the universe.

In order to probe for the presence of such protoclusters, one can perform deep imaging observations around the first quasars to select galaxy candidates, and compare their number density to that observed in "blank fields", i.e. field without a quasar. Spectroscopic confirmation of the galaxy candidates around the quasar would strengthen our understanding of their environments. However, whether quasars at $z \sim 6$ reside in overdense regions is heavily debated in the literature. Discrepancies in these findings can be explained by the different observational techniques used to identify galaxies around quasars. For instance, photometric searches for Lyman-break galaxies (e.g., Zheng et al., 2006; Morselli et al., 2014; Simpson et al., 2014), for Lyman-α emitters (e.g., Mazzucchelli et al., 2017a), or for a combination of both (e.g., Ota et al., 2018), spectroscopic confirmations of galaxies (e.g., Bosman et al., 2020; Mignoli et al., 2020), or [C II] emitters and sub-millimeter galaxy searches (e.g., Decarli et al., 2017; Champagne et al., 2018; Meyer et al., 2022). Additionally, these works cover different physical areas and ways of assessing the presence of an overdensity (e.g., Overzier, 2022). Finally, the results are affected by cosmic variance given the handful of known $z \sim 6$ quasars (García-Vergara et al., 2019).

The highest-redshift with zoom-in simulations available from Costa et al. (2014) demonstrate that overdensities of Lyman-break galaxies (LBG) and young Lyman-α emitting galaxies (LAE) around quasars up to $z \sim 6.2$ can be probed within a 1.2 proper-Mpc^2 environment using the *HST* ACS Wide Field Chanel. As predicted

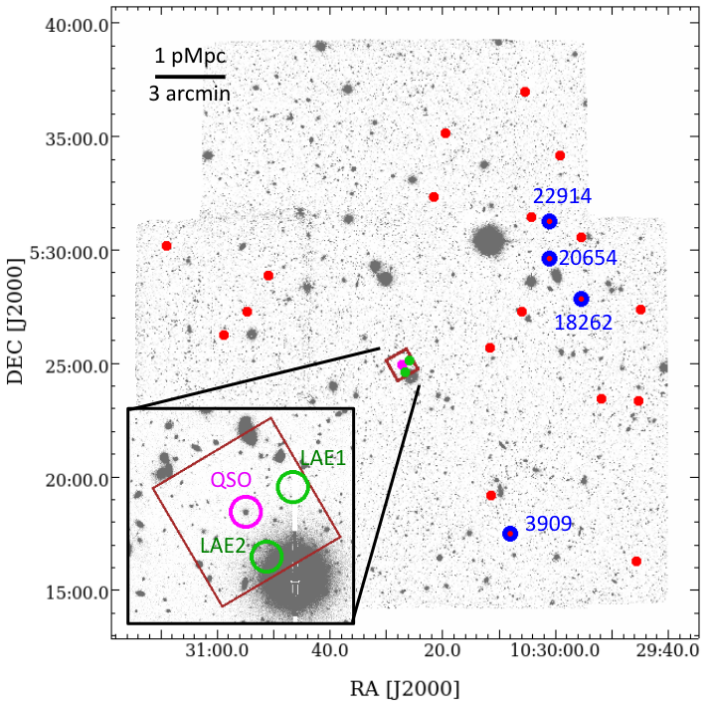

Figure 1.8: The highest redshift galaxy overdense field around $z = 6.32$ quasar SDSS J1030+0524 evidenced in Mignoli et al. (2020). Six confirmed neighboring galaxies are found, two are Lyman ALpha Emitter (LAE) (green) and 4 are LBG (blue). These observations illustrate the web-like structure of galaxy assembly in the early universe.

from these simulations, an example of a $z = 6.3$ overdense quasar field was selected with this instrument, and later confirmed with multiple ground-based telescope observations (see Figure 1.8 Mignoli et al., 2020). This system is to this day the highest redshift galaxy overdensity in a quasar field. A quasar at higher redshift, ULAS J1120+0641 at $z = 7.1$, was studied with the same *HST*ACS strategy but does not report an overdensity (Simpson et al., 2014). Nevertheless, the Mpc-scale environments of quasars at the highest known redshifts, i.e. $z \sim 7.5$, had not been studied yet. The first study looking at the environment of one of these three $z \sim 7.5$ quasars is developed in this thesis and presented in Chapter 2. Future JWST program GO/cy1 1764[1] will aim at observing part of the environments of the three quasars currently known at $z \sim 7.5$, pushing even further the frontier of large-scale environments around the earliest quasars.

1.7 HOST GALAXY ENVIRONMENTS OF RADIO-LOUD QUASARS

The host galaxies of quasars at $z \gtrsim 5.5$ or $t_{age} \lesssim 1$ Gyr have revealed star formation rates (SFR) reaching up to $100 - 2500$ $M_\odot$ yr^{-1} (e.g., Decarli et al., 2018; Shao et al., 2019). The emergent picture is that the ratio of black hole mass to host galaxy

1 https://www.stsci.edu/jwst/science-execution/program-information.html?id=1764

dynamical mass is higher by a factor of 3–4 than expected from local relations (e.g., Venemans et al., 2016; Neeleman et al., 2021), suggesting that the black holes are growing more rapidly than their host galaxies. However, thus far all results within the first Gyr of the Universe are based solely on radio-quiet quasars, i.e. when no jet emission is observed or it is considerably weak (refer to §1.5 above and Figure 1.6).

As discussed previously in §1.6, quasars at $z \sim 6$ challenge evolutionary models of galaxies and AGN, as they have to be able to form and grow billion-solar-mass black holes in less than a Gyr (e.g., Inayoshi, Visbal, and Haiman, 2020). In this context, radio jets are a possible mechanism to aid such a rapid growth by enhancing the black hole accretion rates (e.g., Jolley and Kuncic, 2008; Ghisellini et al., 2010; Ghisellini et al., 2015; Volonteri, Silk, and Dubus, 2015; Regan et al., 2019). Furthermore, the interplay between radio jets and the interstellar medium is thought to be an important mechanism responsible for the tight correlation between the mass of a galaxy and its central black hole (e.g., Kormendy and Ho, 2013). Hydrodynamical cosmological simulations require strong AGN feedback already at $z \sim 6$ to reproduce the observed distribution of galaxy masses at $z = 0$ (e.g., Kaviraj et al., 2017). Observationally, however, evidence of AGN feedback has yet to be confirmed in sources at $z \gtrsim 6$ where both host galaxy and black hole are experiencing the first extreme and efficient growth (see also Bischetti et al., 2019; Novak et al., 2020). The launch of jets is thought to be an episode in the life of all AGN, it is thus possible to test this AGN feedback directly on the quasars currently going through this stage.

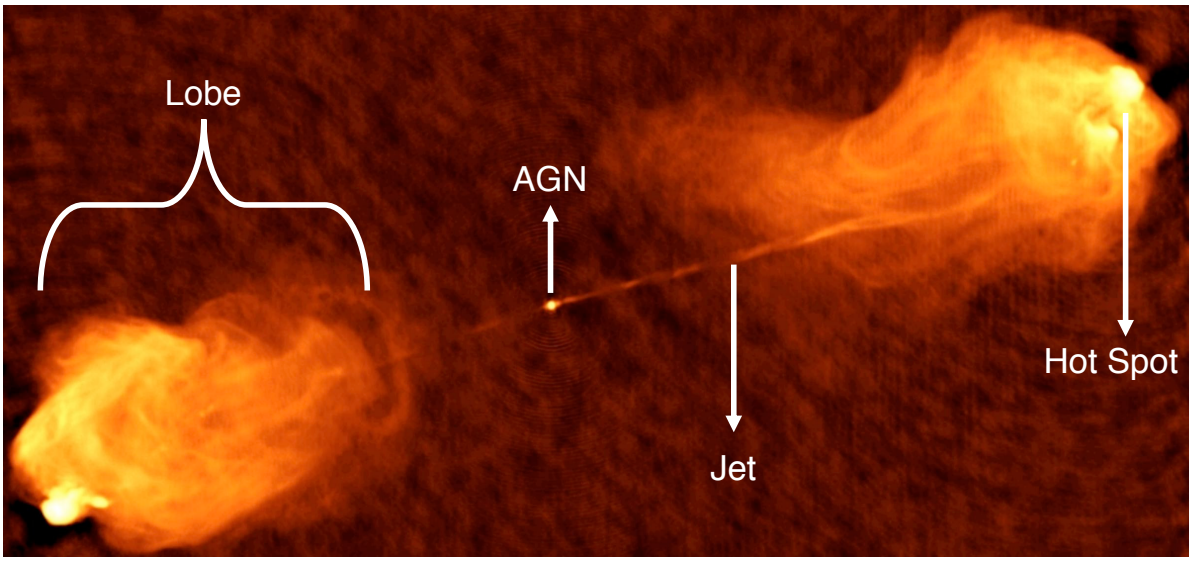

Figure 1.9: Example of the radio galaxy Cygnus A ($z = 0.06$) to show the different components of an active black hole (AGN). The radio jet is shown as a collimated structure coming out of the AGN and, given the viewing angle, we can see a counter jet in this case. The jets are often brighter in X-ray emission, but the Lobes surrounding the path are bright in radio. Finally, the hot spots are regions where the jet is shocking with the ISM and are bright in radio wavelengths as well. For quasars at $z > 5.5$ is possible to see radio hot spots, indirectly evidencing the presence of an active jet. Image credit: NRAO/AUI (adapted).

A jet is the conversion of accreted material into a well-collimated structure where the electrons getting wrapped in the magnetic field emit synchrotron radiation. Thus, *radio-loud* quasars would present strong radio synchrotron emission. The radio-loudness 'R' of a quasar can be determined when comparing the brightness of the source in rest-frame radio frequency at 5 GHz, dominated by the synchrotron emission from the jet, and the optical emission at rest-frame 4400Å, or 2500Å following the definitions in Sramek and Weedman (1980) and Kellermann et al. (1989):

$R_{4400} = f_{\nu,5\,\mathrm{GHz}} / f_{\nu,4400\,\text{Å}} > 10$, or

$R_{2500} = f_{\nu,5\,\mathrm{GHz}} / f_{\nu,2500\,\text{Å}} > 10$

The current scenario points at only ~ 10% of the known quasar population as strong radio emitters at $z > 5.5$ (e.g., Bañados et al., 2015b; Bañados et al., 2021; Belladitta et al., 2020; Liu et al., 2021; Gloudemans et al., 2022). This percentage is similar to what is observed for the AGN population at lower redshifts ($z \lesssim 2.5$; Sandage, 1965; Retana-Montenegro and Röttgering, 2017). Studying the effects that radio jets have on the stellar properties of a galaxy is challenging because the central AGN outshines the stars (e.g., Zibetti, Charlot, and Rix, 2009; Taylor et al., 2011). This is particularly difficult at high redshift and stellar emission from host galaxies of $z \sim 6$ quasars has yet to be detected (e.g., Decarli et al., 2012; Mechtley et al., 2012; Marshall et al., 2020). Additionally, the jet cannot be directly observed for quasars at these faraway distances, but only its interaction with the ISM in the form of hot spots (see Figure 1.9).

How can we try to test AGN feedback in the first Gyr of the universe? Fortunately, and as discussed previously in §1.4, at these redshifts key tracers of atomic and molecular gas from the host galaxy, such as [C II]-158 μm and CO, are redshifted from the rest-frame FIR to the sub-millimeter wavelengths and thus can be observed with facilities like ALMA or NOEMA. Due to the observations of these tracers is possible to infer kinematics, star-formation properties, and masses of the host galaxy (e.g., Wang et al., 2013). Thus, the study of these tracers in radio-loud quasars can reveal whether the jets are affecting the gas that fuels star formation in the host galaxy.

It has been only in the last two years of the time of writing this thesis that the host galaxies of radio-loud quasars at $z \gtrsim 5.5$ have first been studied in millimeter observations at these redshifts. Chapter 3 discusses the first study of the host galaxy of radio-loud quasar P352–15 presenting evidence of a ~ 1.6 kpc-scale jet. Further studies on radio-loud quasars are presented in Rojas-Ruiz et al. (2021) and Khusanova et al. (2022) (see also Figure 1.10). In these studies it can be seen that for some radio-loud quasars where the synchrotron emission, which normally is described with a power-law of the form $S_\nu \propto \nu^\alpha$, has a break towards higher frequencies. This break has been typically observed at lower redshifts (including for the case of Cygnus A from Figure 1.9) when jets are thought to go through ISM shocks, and the break frequency at which this event occurs has been extensively studied (e.g., Kardashev, 1962; Pacholczyk, 1970; Jaffe and Perola, 1973; Carilli et al., 1991; Mahatma et al., 2020). See more on this power-law break effect for quasar P352–15 in Chapter 4. The role of radio jets in the interstellar medium of the host galaxy is recently being ex-

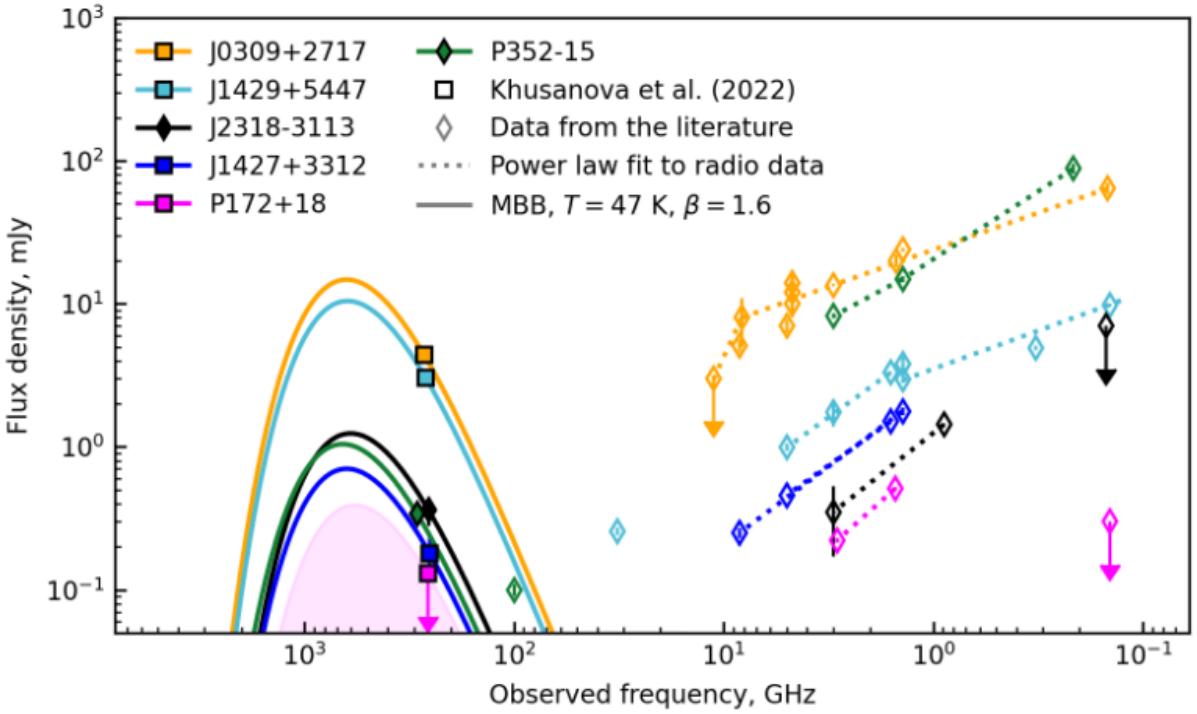

Figure 1.10: The SED of all known radio-loud quasars at $z > 5.5$, taken from Khusanova et al. (2022). The solid lines describe the cold dust emission, which is similar to a blackbody model. The dotted lines are the synchrotron power-law emission that describes the power of the jet. Note that for a few quasars, J0309+2717, J1429+5447 and P352–15, there is a broken power law, showing potential evidence of shocks between of jet with the ISM.

plored at these high redshifts.

1.8 QUASAR LIFETIME FROM PROXIMITY ZONE

The presence of quasars as early in the universe as $z \sim 7.5$ indicate that quasars need to form and grow efficiently during the first 700 Myrs of the universe. The question arises of how old are the quasars we observe at this time. This can be challenging to answer observationally given that the black hole accretion can have different episodes of activity from the time that it first forms. Various simulations and studies of quasars in the local universe show that the intermittent accretion timescales vary between days at $\sim 10^4$ yrs (e.g., Ostriker et al., 2010; Novak, Ostriker, and Ciotti, 2011; Choi et al., 2012) However, it is certain that the light we observe today from a distant quasar is being produced from the most recent accretion episode. Thus, we can measure for how long the quasar has been living its latest accretion episode, the *quasar lifetime*, t_Q. A recent method developed by Eilers et al. (2017) and Eilers, Hennawi, and Davies (2018) to measure t_Q involves the analysis of proximity zones in quasars, and is the one we use in this thesis.

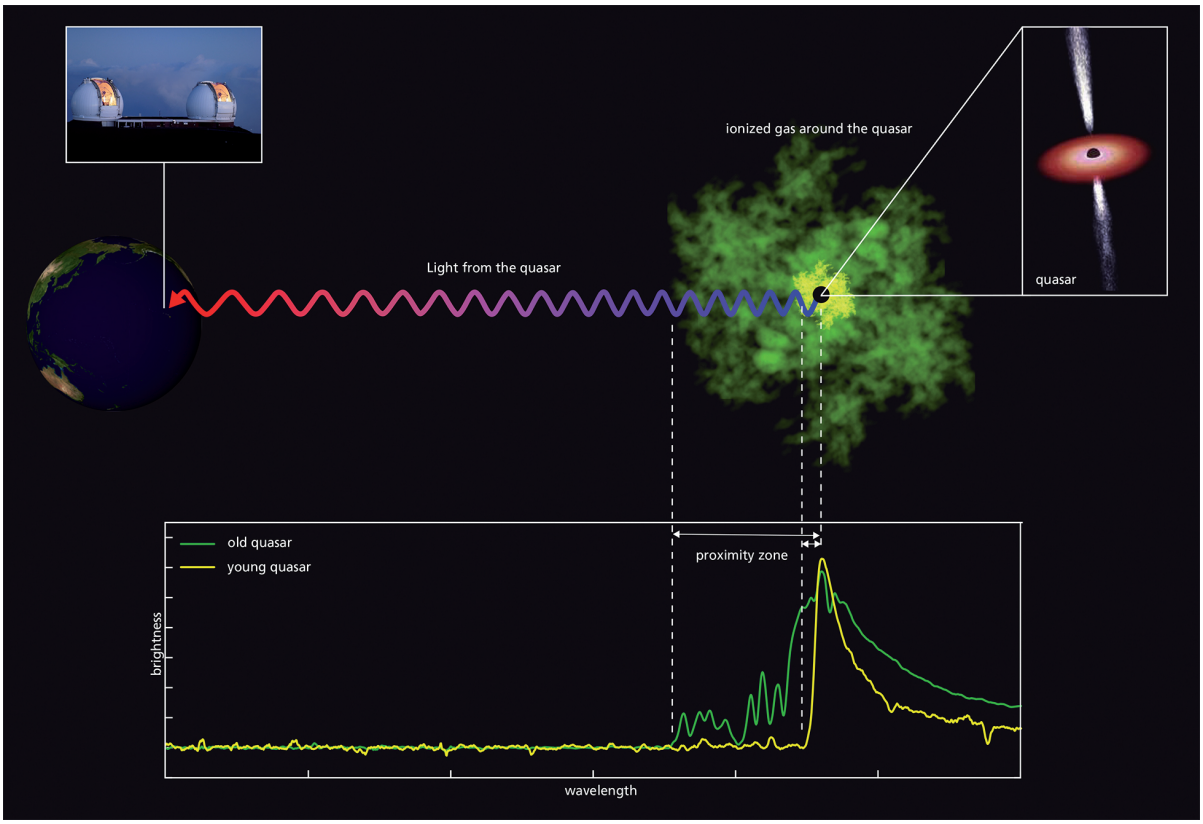

Figure 1.11: Illustration of the quasar lifetime estimate by measuring the proximity zone. Absorption is much less in the quasar's proximity zone for an older quasar (green), than for a younger quasar (yellow). The extent of the proximity zone can be read off the spectrum (bottom). Figure Credit: A. C. Eilers & J. Neidel, MPIA

As previously seen in §1.3, the spectra of high redshift quasars show almost complete absorption bluewards of the Lyα emission line due to patches of neutral hydrogen in the IGM along the line-of-sight to the quasar. However, we can observe enhanced transmitted flux in the immediate environment of the quasar because its UV-radiation radially ionizes the gas in its surrounding in the form of an ionizing bubble (e.g., Madau and Rees, 2000; Cen and Haiman, 2000; Haiman and Cen, 2001; Wyithe, Loeb, and Carilli, 2005; Keating et al., 2015; Eilers et al., 2017). This bubble is bigger for an older quasar as the surrounding medium has been ionized for longer time (see Figure 1.11). The IGM has a limited reaction time to achieve a new ionization equilibrium state as a result of the photoionization of a typical luminous quasar with $M_{1450} \sim -27$, with a timeframe $t_{eq} \approx \Gamma^{-1}{}_{HI} \approx 3 \times 10^4$yrs, where $\Gamma^{-1}{}_{HI}$ is the photoionization rate (Eilers et al., 2017). It is possible to measure the size of this ionized HII bubble following the approach in Haiman and Cen (2001) on *Strömgren spheres*. The following equation measures the ionizing radius R_{ion} for the sphere to expand into a neutral uniform ambient IGM:

$$R_{ion} \approx \left(\frac{3\dot{N}_\gamma t_Q}{4\pi n_H x_{HI}} \right)^{1/3} \tag{1.17}$$

The ionized region around the quasar thus depends on the rate at which ionizing photons are emitted $\dot{N}_\gamma$, the quasar lifetime t_Q, the neutral hydrogen fraction x_{HI}, and the number density of hydrogen n_H. This expression, however, does not predict the distribution of residual neutral hydrogen within the ionized bubble. In contrast, the observed size of the proximity zone (R_p) depends sensitively on the fraction and distribution of the residual neutral hydrogen, because this can cause saturated absorption well before the ionization front is reached (e.g., Eilers et al., 2017). The proximity zone is defined as the extent of the transmitted flux until it drops below the 10% level (e.g., Fan et al., 2006). In order to measure this R_p with higher precision, it is necessary to know accurately the distance to the source, its systemic redshift z_{sys}. Details on the precise measurement of this proximity zone in the quasar spectra are presented in Chapter 4.

Interpreting the quasar lifetime t_Q from the proximity zone R_p requires an understanding of the photoionization on the IGM along the line-of-sight. For this, it is necessary to run radiative transfer simulations that compute the time-dependent ionization and recombination of different species of hydrogen and helium. For this is necessary to consider the associated photoionization heating and cooling by various processes including adiabatic cooling due to the expansion of the universe and inverse Compton cooling off CMB photons (e.g., Bolton and Haehnelt, 2007; Davies, Furlanetto, and McQuinn, 2016). Different studies have observed that average sizes of proximity zones in quasars are $0.8 \lesssim R_p \lesssim 7.1$ pMpc for UV- bright quasars and $0.5 \lesssim R_p \lesssim 4$ pMpc for faint quasars, corresponding to $t_Q \gtrsim 10^6$ (Eilers et al., 2017; Eilers, Hennawi, and Davies, 2018). However, some quasars reveal the unexpected population of very young lifetimes of only $\sim 10^4 - 10^5$ yr, ($0.3 \lesssim R_p \lesssim 1.5$ pMpc) which further challenges current black hole formation models (e.g., Eilers et al., 2021a).

It is important to note that although this method of finding t_Q with proximity zone measurements has proven to be adequate, complications remain. Since this method depends heavily on the observed spectra of quasars, if there are additional absorbers in the line-of-sight, their signature also becomes imprinted in the spectra and prevent measuring the point at which the proximity zone ends. These absorbers can be of the form of aLyman limit System (LLS) or Damped Lyα (DLA). These systems could be intervening in the line-of-sight at lower redshifts, or be physically associated with the quasar pc- or kpc-environment (e.g., Eilers et al., 2017; Bañados et al., 2018b; Andika et al., 2022). It is often relatively easy to identify these absorbers given that they are present in the quasar spectra as strong metal-line absorbers. Some examples of strong absorption are when there is the presence of low-ionization species such as Mg II, C II, Si II, Fe II, Al II, and especially [C II] (e.g., Simcoe et al., 2020). In this thesis we further explore a type of DLA in the quasar spectra of P352–15, and approaches to calculate t_Q in Chapter 4.

This introduction section has contextualized the science we explore in the following Chapters. We describe the work of studying Mpc-scale environments around quasars by investigating ULAS J1342+0928, an exemplary luminous quasar at $z = 7.54$ (Chapter 2). We also focus on studying the kiloparsec to sub-parsec environ-

ment of the radio-loud quasar P3352–15 at $z = 5.832$ in Chapters 3 and 4. Finally a summary of this science is presented in Chapter 5.

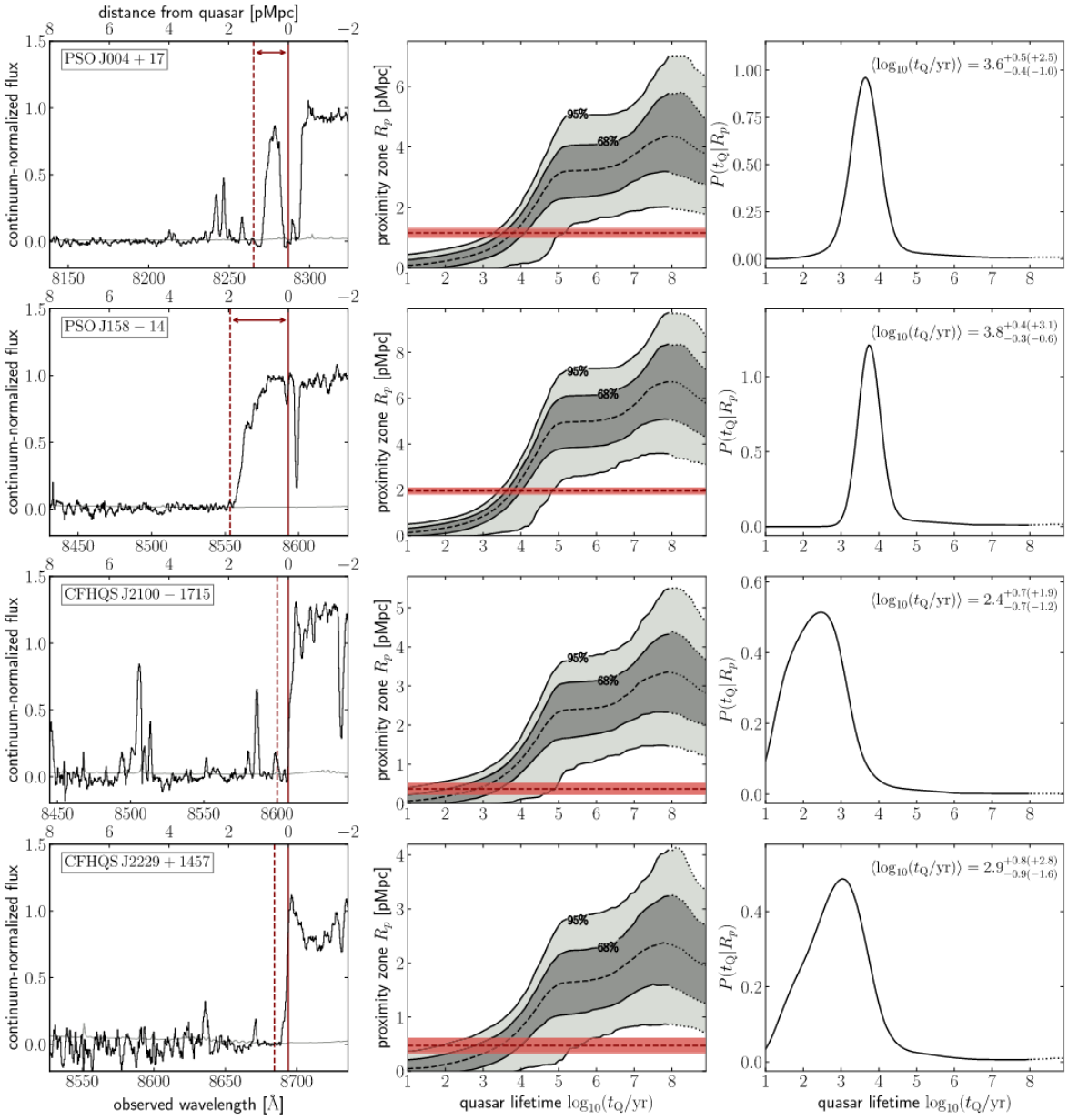

Figure 1.12: Quasar lifetime estimates of very young quasars. Left panels: the proximity zone extension is indicated with the red vertical lines on the quasar spectra. Middle panels: evolution of proximity zone sizes with quasar lifetime from radiative transfer simulations, and the size of the proximity zone shown in red. Right panels: probability distribution of the quasar's lifetime marginalized over the proximity zone measurement uncertainty. Figure taken from Eilers et al. (2021a).

2

THE MPC-SCALE ENVIRONMENT OF THE $z = 7.54$ QUASAR ULAS J1342+0928

In this Chapter, we study the large-scale environment around one of the earliest found quasars in the universe ULAS J1342+0928, which sits at $z = 7.54$ or when the universe was 679 Myr old. First, we introduce the discovery of this quasar and briefly describe its properties in §2.1. To investigate the Mpc-scale environment of this quasar we use *HST* data as described in §2.2. The *HST* photometry, noise calculation, and aperture corrections to make the initial catalog to look for LBG candidates are described in §2.3, including available *Spitzer*/IRAC photometry (§2.3.3). The selection criterion and photometric-redshift analysis to create the final catalog of galaxy candidates are described in §2.4. Details on the properties of the resulting galaxy candidates are discussed in §2.5. As a quality check of the selected galaxy candidates, §2.6.1 discusses the catalog completeness assessment given the data at hand compared to blank field findings. A discussion of the results, the interpretation of the findings in relation to galaxy overdensity and *JWST* follow-up observations are presented in §2.6. Finally, we summarize this work in §2.7.

This work has been submitted to the *AAS Journals* at the time of writing this thesis. I led the analysis and interpretation of this work. Co-author Chiara Mazzucchelli, Peter Zeidler, and I worked on the reduction of the *HST* images. I extracted the photometry measurements from *HST* images and collaborator Gabriel Brammer provided the reduction and photometry from *Spitzer*/IRAC observations. I performed the search for LBG candidates, analysis, and results. Steven Finkelstein shared the CANDELS/GOODS catalog to estimate the completeness of LBG finding in our work and helped calculate the number density in the quasar field. The QSO-LBG clustering analysis was developed and interpreted by Emanuele P. Farina and me. Eduardo Bñados helped in the interpretation of different steps in this work. Finally, I wrote the text presented here and obtained constructive comments from the other collaborators.

2.1 BACKGROUND OF ULAS J1342+0928

Early quasars challenge the different theories of black hole formation previously presented in 1.1. Thus, multiple efforts have been carried out to find the first quasars hosting supermassive black holes of $\sim 10^9$ $M_\odot$. Quasar ULAS J1342+0928was selected

as a candidate quasar from its photometry in the the DECam Legacy Survey (DECaLS), the United Kingdom Infrared Telescope Infrared Deep Sky Survey (UKIDSS), and the Wide-field Infrared Survey Explorer (ALLWISE) surveys. Later, it was followed up with near-IR spectral observations from Magellan/FIRE and Gemini/GNIRS in Bañados et al. (2018b), revealing its quasar nature. From the quasar's luminosity and the observed Mg II emission line, it was possible to measure one of the earliest and most massive SMBHs with a mass $\sim 0.9 \times 10^9$ $M_\odot$. This quasar is also actively accreting at near Eddington rates with $L_{bol}/L_{Edd} \sim 1.1$ (Onoue et al., 2020). The host galaxy is already evolved, with a metallicity comparable to the solar neighborhood (Novak et al., 2019). Additionally, spectral studies in Simcoe et al. (2020) identified a strong absorber at $z = 6.84$ in the line-of-sight of ULAS J1342+0928. This massive and active quasar in the early universe is an ideal candidate to now look for a galaxy overdensity and trace its large-scale structure. In this work, we search for LBG candidates at $z \sim 7.5$ in the immediate ~ 1 physical Mpc^2 environment of the $z = 7.54$ quasar ULAS J1342+0928, using deep imaging data collected with the *Hubble Space Telescope* (*HST*), and *Spitzer*/Infrared Array Camera (IRAC).

2.2 OBSERVATIONS

In order to probe a galaxy overdensity, observations around ULAS J1342+0928 need to cover a large area and reach the required sensitivity to find LBGs in the near vicinity of the quasar (at $z \sim 7.5$). *HST* was the only instrument that could accomplish this with the ACS/WFC camera, which comprises the most extended field of view (FOV) of ~ 11 arcmin^2[1]. For the $z = 7.54$ quasar where 1" corresponds to 4.99 pkpc, ACS/WFC provides a suitable area coverage of 1.1 $pMpc^2$.

Usually, at least three filters are occupied to identify galaxies in the epoch of reionization using the Lyman-break technique. The bluest filter serves as the non-detection to confirm the spectral break produced by the intergalactic medium (IGM) absorption of the galaxy's emission. A contiguous filter is centered on the expected wavelength of the Lyman-break serving as the drop-out and detection band, and redder filters are used to observe the detected continuum emission. In this section, we describe the *HST* data obtained to select LBG candidates in the environment of ULAS J1342+0928 and the reduction process.

2.2.1 *HST data and reduction*

We use observations obtained with the Advanced Camera for Survey (ACS) and Wide Field Camera 3 (WFC3) on board *HST* between June 2018 and June 2019 (PI: Bañados, Prog ID:1165). We obtained data in the F814W (ACS, 13 orbits) serving as the non-detection filter, and for detection the F105W and F125W filters (WFC3, 8 and 4 orbits each, respectively). To maximize the ACS surveyed area, WFC3 near-infrared imaging were observed in a 2×2 mosaic strategy. The final effective area covered

1 https://esahubble.org/about/general/instruments/acs/

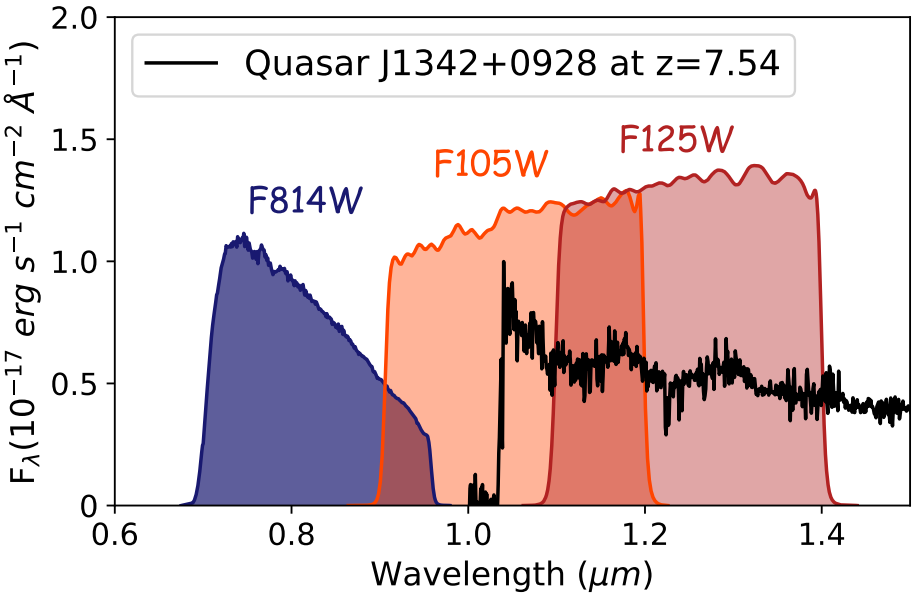

Figure 2.1: *HST* filter coverage used to look for galaxy candidates in the field of ULAS J1342+0928. Overplotted is the spectrum of the quasar from Bañados et al. (2018b). We expect the galaxy candidates laying in close proximity to the quasar at $z \sim 7.5$ to be undetected in the WFC/F814W and begin to drop completely halfway through the WFC3/IR F105W filter while being fully detected in the WFC3/F125W filter. The resulting observations are thus biased towards sources with very red F105W-F125W colors, leading to high uncertainties in the redshift calculation and an incomplete fraction of selected galaxy candidates, which is addressed in §2.6.1.

to search for LBGs is 12.28 arcmin^2. All filter transmission curves are presented in Figure 2.1, with the rest-frame UV spectrum of the $z = 7.54$ quasar overlaid (Bañados et al., 2018b). The presented observations achieve a 5σ limiting AB magnitudes of 28.20, 27.83, and 27.46 in the F814W, F105W, and F125W bands, respectively.

We use the data-reduced images provided by Space Telescope Science Institute (STScI), and implement an ad-hoc method to ensure a good astrometric match between the different filters. We use DrizzlePac[2] to create the final combined images for each filter and ensure a good astrometric match between them. Indeed, a proper alignment between the filters is nontrivial, due to the small number of stars found in the field, which complicates standard reduction routines. We start by considering the *HST* WFC/F814W pipeline-reduced *flc.fits* files, downloaded from the MAST archive[3]. In order to create reference catalogs with enough sources, we run `Source Extractor` (Bertin and Arnouts, 1996) on each image, after cleaning them from cosmic rays contamination using the *astrodrizzle* routine with `cosmic_ray_cr_clean`=True. We use *tweakreg* to align the uncleaned, original *flc.fits* images, utilizing these `Source`

2 https://www.stsci.edu/drizzlepac.html
3 https://archive.stsci.edu/

`Extractor`-created reference catalogs, each containing ~1000 sources. The final combined image in F814W is obtained using *astrodrizzle*, with `skymethod='match'` and `combine_type='median'`. We run again `Source Extractor` on the final, drizzled F814W image, and use this new catalog (4544 sources) as a reference to match the WFC3/F105W and F125W images to the F814W. In detail, we use *tweakreg* on the F105W and F125W *HST* pipeline-reduced *flt.fits* files, with the F814W catalog as reference, `searchrad=3.` and `minobj=6`. We drizzled the matched files to obtain the final F125W and F105W images, with the same *astrodrizzle* parameters used for the F814W filter, and `final_scale=0.''05`, in order to match the pixel scale of the WFC3 images to that of ACS.

In order to check the goodness of our match, we compared the coordinates of sources recovered in all three *HST* final images, considering only the 30 brightest objects. The final mean deviation within the astrometric solutions of the filters is ~0.''03. If we compare instead their astrometry with the GAIA DR2 catalog (Gaia Collaboration et al., 2018), the mean difference in the coordinates of the recovered sources (10 in F814W, 13 in both F105W and F125W) is ~0.''05. We note that the final F105W image is affected by an artifact, due to the presence of a satellite trail in one of the *flt* exposure. We decided to not discard this exposure to obtain the deepest image, but caution is needed when examining sources close to the trail. The final reduced images F814W, F105W and F125W (hereafter i_{814}, Y_{105}, and J_{125}) are presented in Figure 2.2 as an RGB color image created with JS9-4L (v2.2; Mandel and Vikhlinin 2018).

2.2.1.1 *Point-Spread Function (PSF) Matching*

Finding high-redshift galaxies requires very accurate colors from photometric measurements in different bands. We calculate the photometry in fixed aperture diameters of 0.''4, as later discussed in Section 2.4, and therefore imaging in all bands need to be matched to the same PSF. The reference matching image is the one with the largest PSF full width at half maximum (FWHM), which in this case is the J_{125} band. For every band, we first attempted to select appropriate stars contributing to the building of the PSF by making a half-light radius versus magnitude diagram to identify the stellar locus. However, since there are not many stars in the field, and several were saturated, we did not manage to obtain a reliable PSF model from the images. To perform the PSF matching we therefore relied on the standard *HST* PSFs produced with a high level of precision by STScI[4] from the `_flt / _flc` frame (see Figure 2.3. The matching kernel for image convolution is produced with `pyPHER` (Boucaud et al., 2016) to make the final PSF-matched images.

From these stars, we use the Python photutils function `EPSFBuilder` with an oversample factor of 10 and number of iterations defined by the user to ensure an accurate centroid for the stacked stars. The ePSFs are rescaled back to the original pixel size to then make the kernel for the corresponding bands using `Pypher`. The kernels are used to finally convolve the F814W and F105W images to match the F125W image.

4 https://www.stsci.edu/hst/instrumentation/wfc3/data-analysis/psf

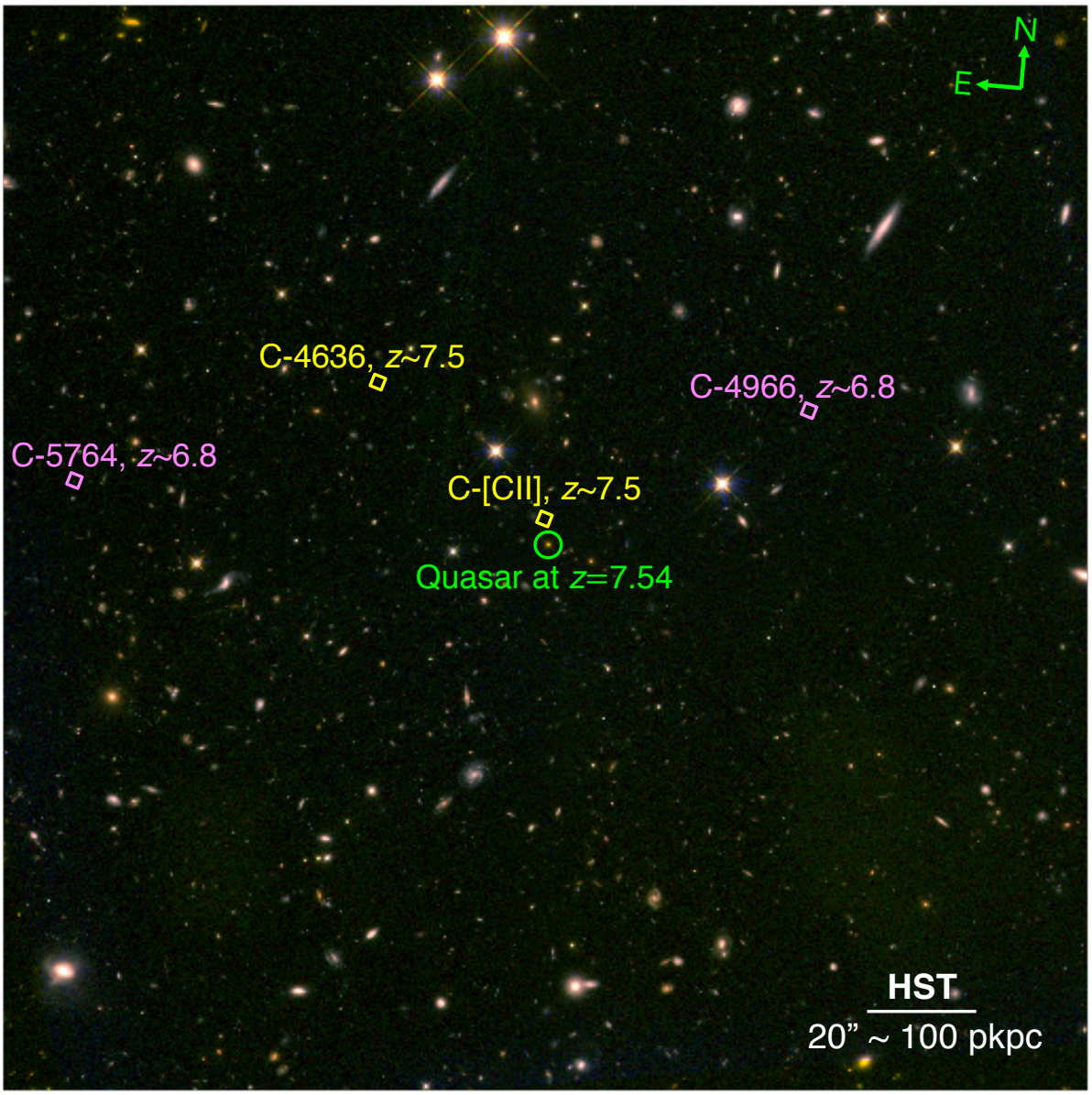

Figure 2.2: *HST iYJ* RGB color-image of the field around the quasar ULAS J1342+0928. The quasar is in the center as presented in the circled region. The high-redshift galaxy candidates selected in this work are overlaid here and described in §2.5. The source C-4636 is an LBG candidate identified in this analysis to be at $z_{\rm phot} = 7.69$. Candidate C-[C II] is a [C II] emitter previously identified in Venemans et al. (2020) to be at $z_{\rm [C\,II]} = 7.5341 \pm 0.0009$ and does not have *HST* or *Spitzer* counterpart emission, making it a dust-obscured candidate in the environment of the quasar. These two galaxy candidates are within 223 pkpc of the quasar, possibly indicating strong clustering around the quasar. Additional LBG candidates in the observed field, C-4966 and C-5764 are at $z_{\rm phot} = 6.91$ and 6.89, respectively. These candidates could be associated with a strong absorber at $z = 6.84$ identified in the spectrum of ULAS J1342+0928 by Simcoe et al. (2020).

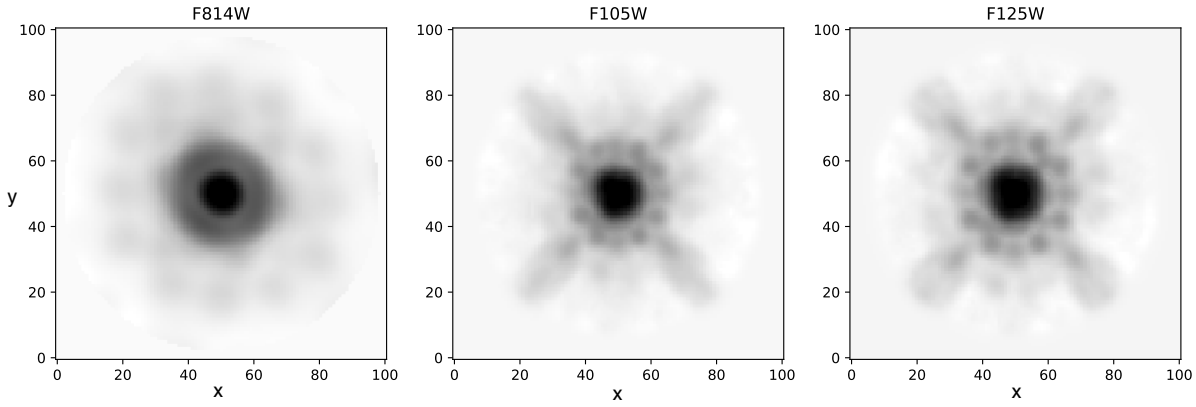

Figure 2.3: The standard PSFs produced at a high level of precision by STScI for the *HST* filters. Given the lack of stars in the FOV explored around ULAS J1342+0928, we cannot model a PSF from star stacking and thus rely on these measured PSFs for the remaining of this work.

2.3 MAKING THE CATALOGS

This analysis follows closely the procedure for Lyman-break detection in Rojas-Ruiz et al. (2020). We utilize the Software `Source Extractor` v2.25.0 to measure the photometry of the sources in all three *HST* filters in dual-mode with a coadded $Y_{105} + J_{125}$ as the detection image, which serves to maximize the signal-to-noise (S/N) and minimize the number of spurious sources resulting in the catalogs. The errors provided by `Source Extractor` depend on the RMS map, which for each band were created from the sky flux measurements in the science image (SCI) found with a 2.5-σ clipping, and the reduced weight image (WHT) as follows:

$$\mathrm{RMS} = \frac{\sigma_{\mathrm{SCI}}}{\mathrm{Median}\{1/\sqrt{\mathrm{WHT}}\}} \times \frac{1}{\sqrt{\mathrm{WHT}}} \tag{2.1}$$

The flux of the objects is measured in a small Kron elliptical aperture (PHOT_AUTOPARAMS 1.2, 1.7) that is later corrected up to total magnitudes using the flux measured in a larger Kron aperture (PHOT_AUTOPARAMS 2.5, 3.5), as previously done in high-redshift galaxy studies (e.g., Bouwens et al., 2010; Bouwens et al., 2021; Finkelstein et al., 2010; Finkelstein et al., 2022). To identify point-like sources in our catalog, rather than rely on the CLASS_STAR parameter from `Source Extractor` that can be misleading when investigating high-redshift sources (see Finkelstein et al., 2015; Morishita et al., 2018), we also perform photometry in a $0''.4$ circular aperture in diameter. Comparing the ratio between the Kron elliptical aperture and the $0''.4$ circular aperture sizes help identify point-like sources such as stars or bad pixels. This circular aperture also serves as a high S/N measurement of the source at the targeted wavelengths and is thus relevant for the S/N cuts in our criteria for selecting candidates at $z \sim 7.5$ as described in §2.4.

Doing a visual inspection of the segmentation map produced from the `Source Extractor` run, the combination of parameters DETECT_THRESH = 1.5 and DE-

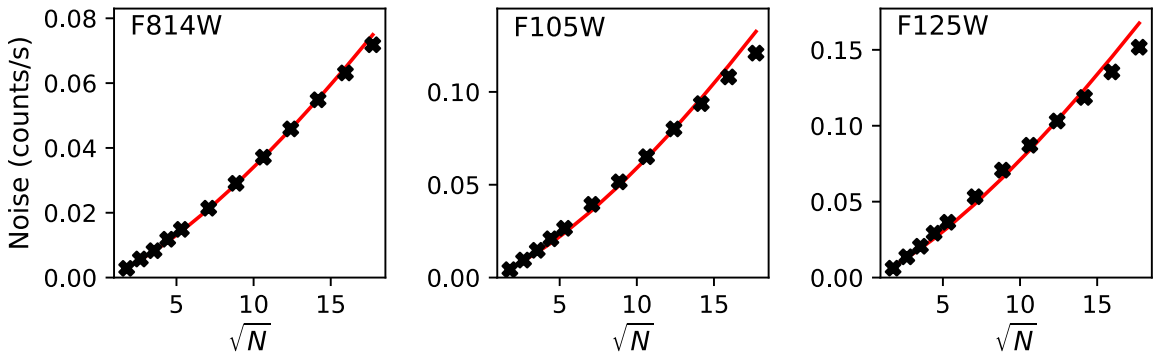

Figure 2.4: Noise calculation for the field in the three-*HST* bands following Equation 2.2. N is the number of pixels in the area of the aperture with diameters 2.0, 3.0, 4.0, 5.0, 6.0, 8.0, 10, 12, 14, 16, 18, 20 (pixel scale is 0.″05). Note how the noise grows with a bigger aperture, as expected from the equation. The red line shows the best fit correlating the noise and aperture size N, which is used to find the α and β free parameters that contribute to the noise estimate (see Equation 2.2). This empirical noise calculation improves the photometric flux error estimations, and therefore the S/N of the sources in the catalogs.

TECT_MINAREA = 7 maximize the number of sources detected while lowering the spurious fraction that would later complicate the background noise calculation.

2.3.1 *Noise Calculation*

We perform an empirical noise calculation of the images rather than rely on the `Source Extractor`-derived photometric errors. We follow closely the procedure described in Papovich et al. (2016) to account for correlated and uncorrelated noise as briefly described here.

For images with exclusively uncorrelated pixels, the noise is measured in a circular aperture of N pixels which scale following $\sigma_n = \sigma_1 \times \sqrt{N}$, where σ_1 is the pixel-to-pixel standard deviation of the background. Conversely, the noise from completely correlated pixels is measured as $\sigma_n = \sigma_1 \times N$. In our *HST* images, the noise truly varies among both correlations as N^β where $0.5 < \beta < 1$, and this can be estimated for the whole image with the parameterized equation:

$$\sigma_n = \sigma_1(\alpha N^\beta) \tag{2.2}$$

where α has to be a positive value. Note that we do not include the Poisson correction of the equation from Papovich et al. (2016) as it did not contribute to the calculation of the noise in the *HST* images. We measure the noise in each of the three *HST* images by first placing random apertures in the sky background with growing sizes from 0.″1 to 1.″0 in diameter. Then, we use the `curvefit` Python function with the Levenberg-Marquardt least-squares method to fit for the noise found in random apertures with increasing size (see Figure 2.4). The calculated noise values in each

image are applied to the Kron and 0.″4 apertures to calculate the flux error in such aperture sizes.

2.3.2 *Corrections to the Photometry Catalogs*

The resulting `Source Extractor` catalogs with the calculated flux errors are then corrected for Galactic dust attenuation following the Cardelli, Clayton, and Mathis (1989) extinction curve with an $R_v = 3.1$, as motivated in similar studies of high-redshift galaxies (e.g., Rojas-Ruiz et al., 2020; Finkelstein et al., 2022; Tacchella et al., 2022). We use Schlafly and Finkbeiner (2011) to calculate the color excess due to galactic extinction, $E(B-V) = 0.025$. The zero points for the final catalog are calculated according to the newest 2020 *HST* photometric calibrations for ACS and WFC3, which apply to the observed dates of the images. The zero points in AB magnitude are 25.9360, 26.2646, and 26.2321 for i_{814}, Y_{105}, and J_{125}, respectively. We also apply in all filters an aperture correction from the large (2.5, 3.5) to small (1.2, 1.7) Kron aperture photometry measured in the J_{125}, to account for the missing PSF flux in the smaller aperture. The catalogs are cleaned from spurious sources identified by a negative aperture correction, from near bright objects with negative fluxes, and lastly from objects near the edges of the images using the `Source Extractor`-generated segmentation map.

2.3.3 Spitzer/*IRAC Photometry*

Additional *Spitzer*/IRAC 3.6μm and 4.5μm images covering the same area of the quasar environment explored with *HST* are available from cycle 16 archival database (PI: Decarli), and each has an exposure time of 3.4 hrs. These additional photometric bands provide crucial information to distinguish true high-redshift galaxies from lower-redshift contaminants. Especially since we only use three *HST* filters, these redder wavelengths populate more the SED of the candidate allowing to differentiate among a dusty Balmer-break galaxy at $z \sim 2$ from the high-redshift candidates of interest at $z \sim 7.5$. The IRAC PSF is about two orders of magnitude larger than in *HST*. Therefore, in order to match the sources from both data the IRAC PSFs need to be modeled in order to correct for deblending of sources and calculate accurate flux and flux errors. The mosaics and modeling are performed following Kokorev et al., 2022, and are briefly described here.

To obtain photometry from the IRAC imaging, a PSF model method is produced using the tools from the Great Observatories Legacy Fields IR Analysis Tools (`GOLFIR`) (Brammer, 2022). This modeling method uses a high-resolution prior, which is built from combining the *HST*/ACS and WFC3 images. This resulting image is combined with the IRAC PSF using a matching kernel to finally obtain the low-resolution templates. The original IRAC images are divided into homogeneous 4×4 patches of 120.″0, which are allowed to overlap to improve the modeling. The brightest stars and sources with high signal-to-noise ratios in the IRAC and *HST* images are man-

ually masked to avoid large residuals from the fit. IRAC model imaging are first generated for the brightest objects in the J_{125} catalog doing a least-squares fit of the low-resolution IRAC patches to the original IRAC data to obtain the modeled fluxes. The flux errors are simply the diagonal of the covariance matrix of the model. Similarly, for the fainter sources in the catalog but the least-squares fit normalizations are then adopted as the IRAC flux densities. The resulting photometry from this PSF modeling method is used for the rest of the analysis.

2.4 SELECTION OF GALAXY CANDIDATES

Galaxy candidates neighboring the quasar ULAS J1342+0928 are found in a similar setup as previous work in the literature (Rojas-Ruiz et al., 2020; Bagley et al., 2022; Finkelstein et al., 2022). We rely on the photometric redshift technique by fitting the best spectral energy distribution (SED) model to the *HST* and *Spitzer* photometry. We constrain the catalog of candidates by applying S/N cuts, quality checks between the low and high-redshift fitting, and color-color comparisons to low-redshift interlopers and MLT brown dwarfs. The different steps to obtain the catalog of galaxy candidates are described in this section.

2.4.1 *Photometric Redshifts with EAZY*

We use the "Easy and Accurate Z_{phot} from Yale" (`EAZY`; Brammer, Dokkum, and Coppi 2008) version 2015-05-08 to calculate the photometric redshifts of all sources in our catalogs. `EAZY` calculates the probability distribution function of photometric redshifts $P(z)$ based on a minimized χ^2 fit of the observed photometry in all given filters to different SED models of known galaxy types. `EAZY` includes the 12 `tweak_fsps_QSF_12_v3` Flexible Stellar Population Synthesis (FSPS) models (Conroy, Gunn, and White, 2009; Conroy and Gunn, 2010), the template from Erb et al. (2010) of the young, low-mass and blue galaxy BX418 at $z = 2.3$ exhibiting high equivalent-width (EW) of nebular lines and Lyα, and a version of this galaxy without the Lyα emission to mimic attenuation from the intergalactic medium (IGM) while preserving strong optical emission lines. All these 14 templates are fed equally into `EAZY` so that it constructs the best-fitting models from a linear combination of the templates to the flux and flux errors of the source measured in the Kron 1.2, 1.7 elliptical aperture (see Section 2.3). For each source, `EAZY` applies IGM absorption following Inoue et al., 2014 for redshift steps of $\Delta z = 0.01$. Initially, we consider the redshift probability distribution when giving the templates freedom from $z = 0.01 - 12$ and assume a flat luminosity prior, as galaxy colors at $z \gtrsim 6$ are not yet well understood (Salmon et al., 2018). This wide redshift range is chosen so that we can evaluate the probability for galaxies truly neighboring ULAS J1342+0928 at $z \sim 7.5$ and their corresponding probability of being a contaminant source at lower redshift ($z < 5$).

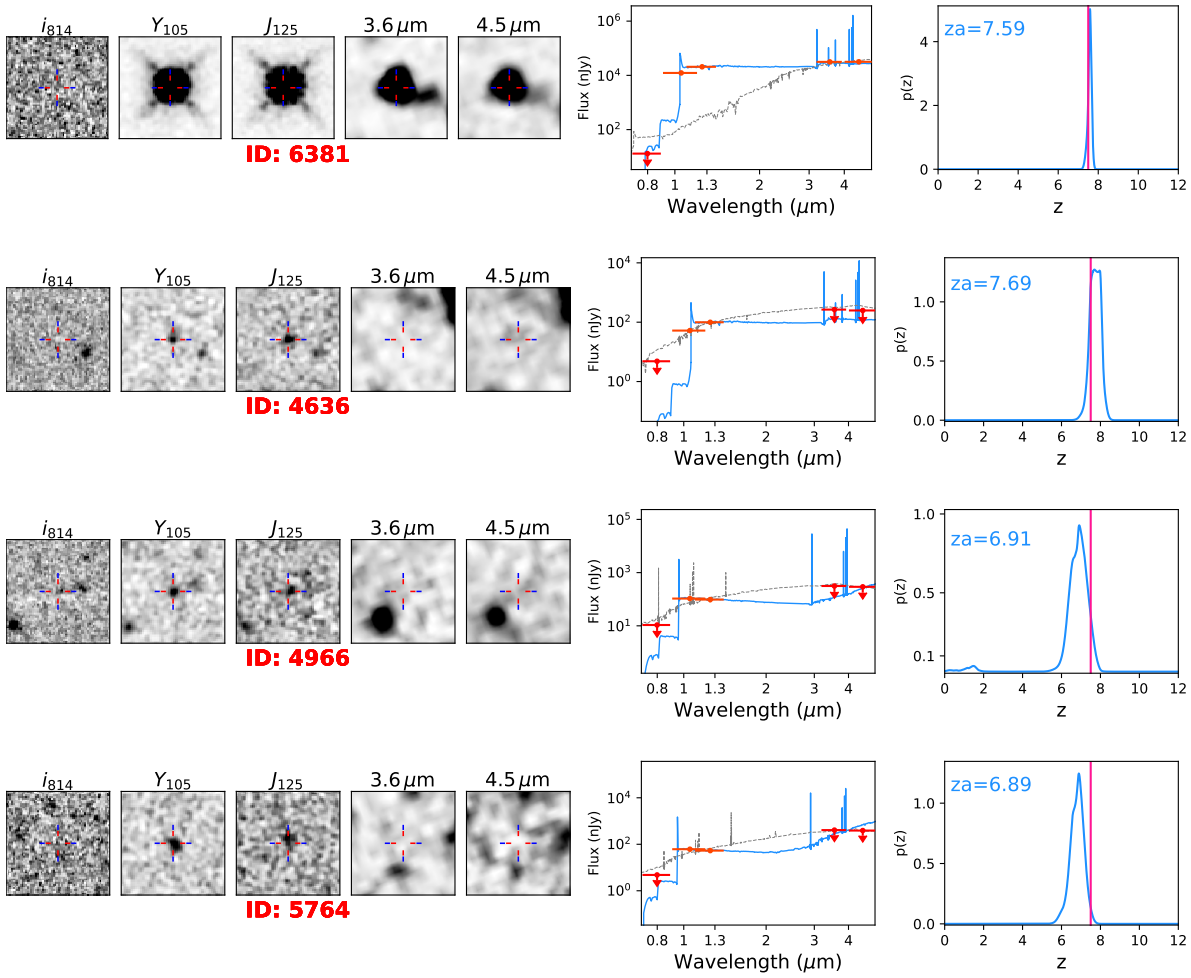

Figure 2.5: Galaxy candidates resulting from our search including the quasar ULAS J1342+0928 at $z = 7.54$, and a new LBG candidate in its environment. *Left:* Postage stamps of each candidate in the iYJ *HST* filters ($3\farcs0 \times 3\farcs0$), and the two *Spitzer*/IRAC bands of this survey ($12\farcs0 \times 12\farcs0$). *Middle:* The best-fit SED of the high-redshift solution of the candidate is presented in blue, with non-detections in red as 1σ upper limits. We present the best-fit SED to a low-redshift solution in a dotted grey line. *Right:* The $P(z)$ versus z from EAZY with the best-fitting redshift denoted as 'za' is presented in blue, and a vertical pink line at $z = 7.5$ for reference to the redshift of quasar ULAS J1342+0928. Note that the redshift probability distributions are highly favored at $z = 7 - 8$ for the top two panels where the quasar is ID: 6381, and an LBG candidate C-4636 associated with the environment of the quasar. This candidate has a slightly higher redshift solution at $z_{\rm phot} = 7.69$ because of the flat $P(z)$ across $z = 7.5 - 8$. The bottom two candidates favor a slightly lower redshift solution at $z \sim 7$.

2.4.2 *Selection Criteria for Catalog*

We build the final catalog of galaxy candidates from the results of the photometric redshift fits from EAZY and applying the following selection criteria.

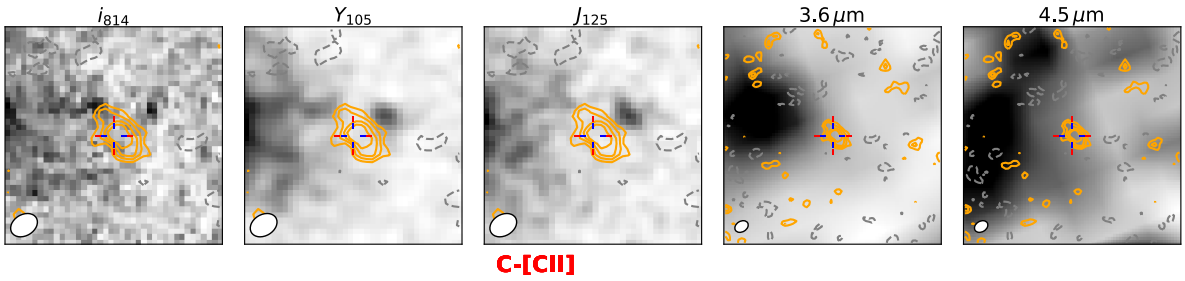

Figure 2.6: Postage stamps in the *HST* (2.″0 × 2.″0) and *Spitzer* (4.″0 × 4.″0) filters used in this work at the position of the dusty star-forming galaxy (DSFG) previously identified with ALMA at $z = 7.5341 \pm 0.0009$ (Venemans et al., 2020). The rest-frame [C II]-158μm emission is presented with the contours at levels $(-2, 2, 3, 4, 5)\sigma$ where the rms value $\sigma = 0.04$ mJy beam^{-1}. The ALMA 222.7 GHz beam with size 0.″26 × 0.″19 is shown in white at the bottom-left corner. This [C II]-emitter is not detected in any of the near-IR filters we use, making this source a candidate DSFG associated with the environment of ULAS J1342+0928.

- $S/N_{i_{814}} < 2.0$ measured in the 0.″4 circular aperture, implying a non-detection in i_{814}.
- $S/N_{Y_{105}}$ or $S/N_{J_{125}} > 5.0$ also in the 0.″4 circular aperture, to ensure the source is detected at high redshift while also potentially selecting strong Lyman-α emitters where the flux would only be detected in the Y_{105}, or galaxies with strongly absorbed Lyman-α producing continuum emission only in the J_{125}.
- The integrated redshift probability $P(z)$ calculated from EAZY at $P(6 < z < 12) > 60\%$, securing that a high-redshift solution dominates over the total probability distribution.
- The integral of the primary peak of the total integrated distribution $P(z_{peak}) > 50\%$.
- The redshift probability distribution at $z = 7.5$ is higher than the neighboring distributions, in $\Delta z = 1$ bins:

  $P(6 < z < 7) < P(7 < z < 8) < P(8 < z < 9)$.

We do not place a cut in the half-light radius of the source in order to include in the catalog possible active galactic nuclei (AGN) sources, which would have a more point-like morphology. However, this parameter is reported in Table 2.2 and is taken into account during the visual inspection step. Note that the half-light radius $r_{0.5}$ of a star in our survey in the J_{125} band is 2.65 pixels, or 0.″13.

Using the above criteria we find 5 LBG candidates where one is the quasar ULAS J1342+0928, and two are identified as diffraction spikes from visual inspection. The succeeding catalog is thus composed of the recovered quasar and two galaxy candidates. We note that decreasing the S/N threshold so that $S/N_{Y_{105}}$ or $S/N_{J_{125}} > 3.0$ results in contamination from marginal detection sources in just one band (25), diffraction spikes (13), and bad pixels or other detector artifacts (25).

Table 2.1: EAZY fit of Galaxy Candidates in the Quasar Field

ID	α (deg)	δ (deg)	$P(z > 6)$ %	$P(6.5 < z < 7.5)$ %	$P(7 < z < 8)$ %	z_{phot}	$\Delta\chi^2_{l-h}$	z_{spec}	d (arcsec)
QSO–6381	205.5337428	9.4773167	100	17	100	$7.59^{+0.08}_{-0.11}$	483.16	7.5413 ± 0.0007^a	
C–4636	205.5435057	9.4851103	100	20	80	$7.69^{+0.33}_{-0.23}$	16.51	...	44.6
C–[C II]	205.5343208	9.4787250	...	...	...	...	...	7.5341 ± 0.0009^b	5.44
C–4966	205.5207121	9.4853401	95	71	39	$6.91^{+0.41}_{-0.51}$	6.48	...	90.4
C–5764	205.5591434	9.4785146	98	79	29	$6.89^{+0.26}_{-0.43}$	14.05	...	55

This table presents the catalog of galaxy candidates in the quasar field, selected here with EAZY using *HST* and *Spitzer* photometry. The reported values at the top correspond to the recovered quasar ULAS J1342+0928 with confirmed systemic redshift $z = 7.54^{\dagger}$, candidate C–4636 at $z \sim 7.5$, and dust-obscured candidate C-[C II] identified with a systemic redshift $z_{[C\,II]}{}^{*}$. The bottom two candidates prefer a lower redshift solution, possibly corresponding to a different environment of an absorber at $z = 6.84$ in the line of sight of the quasar, recovered by Simcoe et al. (2020). Column 1 is the candidate ID. Columns 2-3 are the RA and DEC calculated in degrees. Columns 4-6 present the integral of the redshift probability distribution at $P(z > 6)$ that we require to be higher than 60% in our selection criteria, and the highest probability distribution among the favored $z \sim 7$ and $z \sim 7.5$ candidates at $P(6.5 < z < 7.5)$, and $P(7 < z < 8)$, respectively. Column 7 presents the photometric redshift with the highest probability and its 68% confidence interval as calculated with EAZY. Column 8 shows the difference in the best-fit χ^2 low-redshift ($z < 5$), and the high-redshift ($z < 12$) solutions that are used to assess low-redshift contamination in the catalog. Column 9 is the spectroscopic redshift of the sources when available. Column 10 is the projected distance in arcseconds of the candidate to the quasar.

a Systemic redshift measured using IRAM/NOEMA observations of the [C II]−158μm emission line from the quasar's host galaxy in Venemans et al. (2017a)

b Systemic redshift calculated from [C II]−158μm observations with ALMA in Venemans et al. (2020)

An additional test fitting only a lower-redshift solution was performed to better discriminate among possible low-redshift contaminants. For this, we set EAZY to freely fit the 14 SED templates over a redshift span $z = 0.01 - 5$. We then compared the χ^2 of the best-fit template from this lower-redshift χ^2_{lowz} solution to that at higher-redshift χ^2_{highz}. If $\Delta\chi^2_{l-h} = \chi^2_{lowz} - \chi^2_{highz} < 4$ the goodness of the fit is lower than the threshold of 95% confidence interval, which means the source can be similarly fit with a high and a lower redshift solution (see e.g. Finkelstein et al., 2022; Bagley et al., 2022). We discarded one candidate not passing this test having a $\Delta\chi^2_{l-h} = 2.4$ with a redshift solution $z_{low} = 2.5$ and $z_{high} = 7.9$. The final catalog thus contains the quasar and one new LBG candidate at $z \sim 7.5$ passing the test with $\Delta\chi^2_{l-h} = 16.51$ (see Table 2.1 for the reported values from all candidates).

2.5 GALAXY CANDIDATES IN THE QUASAR FIELD

In this section we present the results from our search of galaxy candidates associated with the quasar ULAS J1342+0928 environment at $z \sim 7.5$. We further comment on the inspection of our *HST*+*Spitzer*/IRAC data at the position of gas-rich [C II]-emitter at $z \sim 7.5$ previously identified in Venemans et al. (2020). Finally, we explore additional galaxy candidates at a slightly lower redshift than that of the quasar, at $z \sim 7$. Figure 2.5 show the postage stamps of the LBG candidates, their SED, and photometric redshift solution from EAZY with both the high-redshift and lower-redshift fits. Table 2.1 summarizes the catalog of these LBGs.

2.5.1 *A galaxy candidate at $z \sim 7.5$*

We recover the quasar with a photometric redshift of $z_{phot} = 7.59$ (its systemic redshift measured from [C II] emission is $z = 7.5413 \pm 0.0007$ (Venemans et al., 2017a)). We find a new LBG candidate, C-4636, at $z_{phot} = 7.69$ (see Figure 2.5). This photometric redshift is slightly higher than $z = 7.5$ given the very flat redshift probability distribution between $z = 7.5 - 8$, but the solution dominates among the other redshift distributions with $P(7 < z < 8) = 80\%$, constraining its association with the environment of the quasar. Moreover, C-4636 is at a distance of 223 proper-kpc from the quasar which is an indicator of quasar-galaxy clustering as seen in similar previous studies (e.g Morselli et al., 2014; Farina et al., 2017; Mignoli et al., 2020; Meyer et al., 2022).

The candidate's color in $Y_{105} - J_{125} = 0.7$ and its compact morphology with a half-light radius $r_{0/5} = 0''.10$ compared to the average radius of stars in this field of $r_{0/5} = 0''.13 \pm 0''.01$, make it a possible MLT-dwarf contaminant (see Figure 2.7). However, the Source Extractor stellarity parameter does not classify this source as a star, with CLASS_STAR = 0.08.. Additionally, galaxies at this redshift would show a distinct SED from MLT contaminants at $\lambda > 2\mu$m, which can be determined even with shallow IRAC imaging (e.g Finkelstein et al., 2022; Bagley et al., 2022).

The non-detection in our IRAC/3.6μm and 4.5μm imaging support the high-redshift nature of this candidate. Thus, we include this source as an LBG candidate in the physical environment of the $z = 7.54$ quasar ULAS J1342+0928. Indeed photometry in contiguous filters redder of the J_{125} band would provide better color diagnostics.

The compact morphology could suggest that C-4636 is an AGN. This is consistent with theoretical simulations which show that AGNs tend to cluster near quasars with SMBH $10^8 - 10^9 M_\odot$(Costa et al., 2014), and some observational cases already seen at $z > 5$ (e.g. McGreer et al., 2016; Connor et al., 2019; Yue et al., 2021). Existing 45ks *Chandra* observations of this field do not show any X-ray signal at this location, indeed there is only an X-ray detection for the quasar (Bañados et al., 2018c). Future JWST NIRSpec spectrum with nebular line emissions could be used for a Baldwin, Philips, & Terlevich (BPT) diagnostic diagram (Baldwin, Phillips, and Terlevich, 1981) to distinguish whether this source is an AGN.

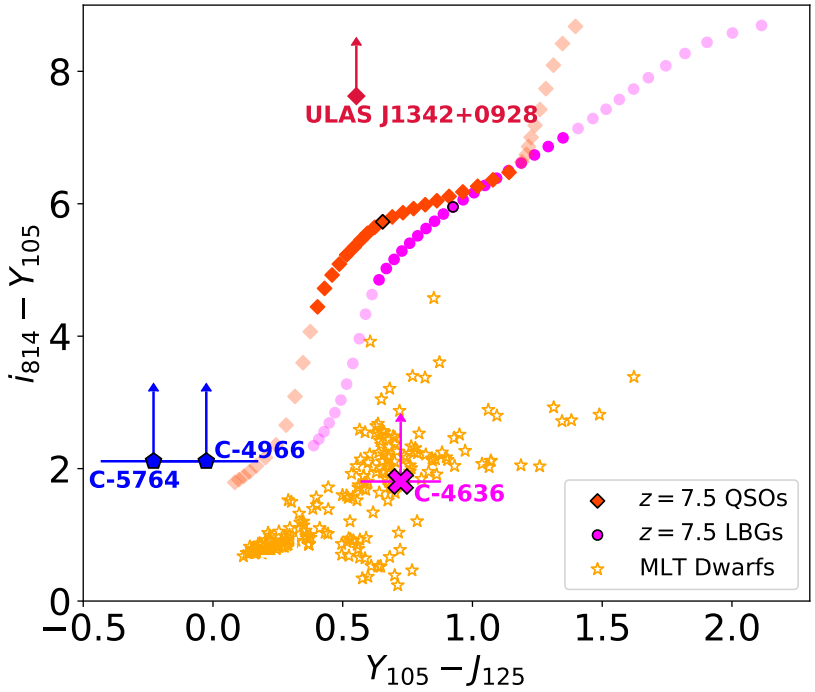

Figure 2.7: Color-Color diagram presenting the colors in *HST* bands of the quasar and LBG candidates. The quasar ULAS J1342+0928 is presented with a crimson diamond showing a strong Lyman Break from the $i_{814} - Y_{105}$ color. The red diamonds and magenta circles indicate the quasars and LBGs with $\Delta z < 2$ from the redshift of the quasar, respectively. The colors of MLT brown dwarf stars in the Milky Way are denoted with yellow stars. LBG candidate C-4636 previously selected with EAZY at $z_{phot} = 7.69$ is shown with the magenta cross. The blue pentagons represent the $z \sim 7$ LBG candidates where, as shown in this diagram, their $Y_{105} - J125$ colors are distinctly bluer from those of $z \sim 7.5$ LBGs.

Table 2.2: Photometry of *HST* and *Spitzer* Selected Galaxy Candidates

ID	S/N_i	S/N_Y	S/N_J	$S/N_{3.6\mu m}$	$S/N_{4.5\mu m}$	i_{814} (AB mag)	Y_{105} (AB mag)	J_{125} (AB mag)	3.6μm (AB mag)	4.5μm (AB mag)	$r_{0.5}$ (arcsec)
QSO–6381	-0.01	3461.1	3772	100.87	118.14	> 28.62	21.18	20.61	20.16	20.15	$0''.14$
C–4636	-1.20	8.63	12.03	-1.0	0.09	> 28.71	27.11	26.41	> 24.14	> 24.22	$0''.10$
C–4966	1.88	9.45	6.62	0.26	0.98	> 28.77	26.34	26.43	> 23.96	> 24.04	$0''.14$
C–5764	0.24	10.64	6.16	0.90	0.19	> 28.80	26.93	27.08	> 23.68	> 23.73	$0''.15$

This table presents the photometry of the catalog of galaxy candidates. Column 1 is the candidate ID. Columns 2-6 are the calculated signal-to-noise values from the $0''.4$-diameter circular aperture in the *HST* bands, and from the *Spitzer* photometry. Columns 7-11 are the calculated AB magnitudes, where the limiting magnitudes correspond to 3σ estimates. Column 12 is the half-light radius of the object in arcseconds.

2.5.2 *Dusty Star-Forming Galaxy*

A galaxy candidate at 27 projected pkpc from the quasar ULAS J1342+0928 had been previously identified in Venemans et al., 2020. This candidate was recovered from ALMA observations targeting the [C II]-158μm (rest-frame) emission of the quasar and found to be at $z_{[C\,II]} = 7.5341 \pm 0.0009$. In order to reinforce the high-redshift nature of this source, we looked for *HST* and *Spitzer*/IRAC counterpart emission. However, we did not detect this galaxy in any of the five images (see Figure 2.6. Since no flux is recovered up to SNR ~ 2, the possibility of this galaxy being a low-redshift interloper is strongly disfavored. Furthermore, many studies have concluded that there is a significant population of dust-obscured galaxies that have no optical counterpart (e.g. Mazzucchelli et al., 2019; Wang et al., 2019b; Meyer et al., 2022). Therefore, this [C II]-emitter could be one of these dusty star-forming galaxies (DSFG) in the environment of ULAS J1342+0928. Currently, the only detection available of this galaxy is from ALMA 223 GHz observations of its [C II] emission at 0.10 ± 0.03 Jy km s^{-1}, and no dust continuum (upper limit, < 0.06) (Venemans et al., 2020). Thus we cannot model a good SED of this galaxy to predict its emission at other wavelengths. These are also the only ALMA observations covering the *HST*+*Spitzer* field and given the small FOV, these are not covering any of the other recovered candidates in this work. Further ALMA or *JWST* observations are necessary to confirm the nature of this source and study its properties.

2.5.3 *Additional Candidates at $z \sim 7$*

On the line-of-sight of the quasar ULAS J1342+0928, through absorption features in the spectrum, a strong metal absorber has been found at $z = 6.84$ (Simcoe et al., 2020). This galaxy has not been directly observed in emission, but its redshift and metal properties are confirmed from the absorption features in the spectra of the quasar. Hence, we also explore candidates at $z \sim 7$ to search for any counterparts (e.g. Neeleman et al., 2019). For this we select all sources with $P(6 < z < 12) > 60\%$, and a $P(6 < z < 7)$ higher than neighboring distributions in $\Delta z = 1$ bins. After visually inspecting the candidates and evaluating the best-fits to high and lower-redshift solutions, $\Delta\chi^2_{l-h}$, we find two galaxy candidates. C-4966 has a photometric redshift of $z_{phot} = 6.91$ and a probability distribution $P(6 < z < 7) = 55\%$ and $P(6.5 < z < 7.5) = 71\%$. C-5764 is found at $z_{phot} = 6.89$ and has a $P(6 < z < 7) = 68\%$ and $P(6.5 < z < 7.5) = 79\%$ (see Figure 2.5, and Table 2.1). Both candidates favor a redshift solution closer to $z = 6.5 - 7.5$. If these galaxies are spectroscopically confirmed, this could point to galaxy clustering in the field at $z \sim 6.8$, near the absorber.

2.6 DISCUSSION

From our extensive search, only one LBG candidate is present in the immediate environment of quasar ULAS J1342+0928at $z \sim 7.5$. Is this the expected number density of galaxies to find? In the following section, we discuss the completeness of our observations to find LBG candidates at $z = 7 - 8$. We further consider different scenarios for an overdensity, or lack of, in this quasar field as compared to blank field searches of LBG candidates at similar redshifts.

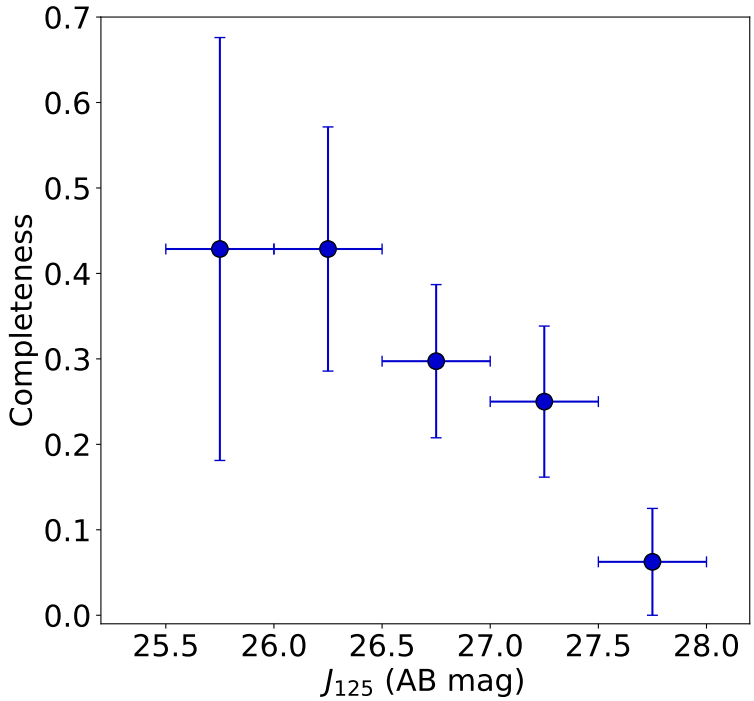

Figure 2.8: Assessment of the completeness of our selection technique of high-redshift galaxy candidates around ULAS J1342+0928presented in magnitude bins of $\Delta_{J_{125}} = 0.5$ and Poisson errors. The comparison of our *HST* observing strategy to what is obtained in the GOODS North and South Deep Fields returns only 43% completeness at the brightest $J_{125} < 26.5$ magnitudes, and drops to $\sim$ 10% between $J_{125} = 27.5 - 28$.

2.6.1 *Completeness*

LBG candidates at $z \sim 7.5$ have the Lyman-break at $\sim 1\,\mu$m, which falls right in the middle of the Y_{105} band used in this work (see Figure 2.1). This means that even if the source is detected in the Y_{105}, their $Y_{105} - J_{125}$ color is red and there is no contiguous filter (e.g. *HST* JH_{140} or H_{160}) to robustly measure the rest-frame UV color redward of the Ly-α break. Although our photometry in the *Sptizer*/IRAC 3.6 μm and 4.5

μm bands enrich the galaxy SED and help determine its dust components to rule out low-redshift contaminants, this is only possible for galaxies already robustly selected at high-redshift with *HST* imaging up to $\lambda \sim 2\mu$m. Our data currently has a wider gap in the wavelength coverage (1.4μm −3.6μm, or J_{125}− IRAC/3.6μm), causing a considerable number of galaxies to never enter the selection catalog. We thus compare the found number density (one new LBG) to what we would recover with a consistent selection of galaxy candidates in the same redshift span of $z \sim 7-8$, using comparable data from blank fields.

The Cosmic Assembly Near-Infrared Deep Extragalactic Legacy Survey (CANDELS) GOODS North and South Deep survey presented in Finkelstein et al. (2015) provides a similar filter coverage (I_{814}, Y_{105}, J_{125}, H_{160}) at comparative depths to our *HST* survey around ULAS J1342+0928. This filter coverage helps to check for the completeness of our data since we can attempt to reproduce the number density of LBGs in a blank field, but using just the I_{814}, Y_{105}, and J_{125} bands and our selection criteria for high-redshift galaxies. We build the photometry catalog for `EAZY` using the fluxes from the GOODS catalog, and the flux errors are set from our limiting magnitudes in the *HST* filters. This way we introduce the noise from our images into the catalog. We run `EAZY` in the same setup and select LBG candidates with the criteria employed for the analysis of the quasar field (see §2.4.2). Using these three *HST* filters alone we recover only 31 sources. This is much lower than the 125 sources with a photometric redshift between $z = 7-8$ in the GOODS catalog when including the additional photometry in H_{160}. Hence, we recover in total only 31/125, i.e. ∼ 25% of the sources.

This test demonstrates the incompleteness at recovering $z \sim 7.5$ galaxies around ULAS J1342+0928 using the current available filter set. Specifically, the recovered fraction of galaxies and their magnitudes in J_{125} is shown in bins of $\Delta 0.5$ mag in Figure 2.8. Note that the faintest galaxy candidate recovered from this catalog has $J_{125} = 27.53$, whereas the GOODS catalog from Finkelstein et al. (2015) has sources as dim as $J_{125} = 28.76$. The highest recovered rate at 43% of galaxy candidates from GOODS are those with $J_{125} < 26.5$, which is in fact within the magnitude of the LBG candidate C-4636 from our results with $J_{125} = 26.41$ (see Table 2.2). However note that our limiting magnitude in this band is deeper reaching up to $J_{125,5\sigma} = 27.46$.

2.6.2 *Exploring an Overdensity at $z \sim 7.5$*

Despite these completeness caveats discussed in §2.6.1, this work presents one LBG at $z \sim 7.5$ in the environment of the quasar ULAS J1342+0928 from the available *HST*+*Spitzer*/IRAC data set. In order to identify whether the number of galaxies found traces an overdensity, we compare this number density to LBGs in blank fields using the rest-frame UV-luminosity function (UV-LF) from Finkelstein et al. (2015), which uses a similar filter coverage to our survey discussed in the previous section. For this purpose, we multiply the completeness function obtained from our *HST* findings (see Figure 2.8) by the integrated UV-LF to find the number of LBGs that should have been found in a blank field. We find that 0.2 galaxies are expected in an average density over our survey area of 12.28 arcmin^2, within $\Delta_z = 0.1$. However, we

find one LBG candidate, which implies a 5-times overdense field at $z \sim 7.5$. Nevertheless, the significance of this candidate overdensity is of just 0.9σ due to our presently poor completeness. Note that in this estimation we do not include C-[C II] the DSFG identified with ALMA in the environment of the quasar, given that these types of galaxies that are not bright in rest-UV emission are not included in UV luminosity function studies.

In the presence of clustering, the expected number of LBG is boosted by a factor $1 + \xi(r)$, where $\xi(r = \left(r/r_0^{QG}\right)^{\gamma}$ is the quasar and LBG (QSO-LBG) cross-correlation function, r_0^{QG} is the cross-correlation length, and γ is the slope. The highest redshift at which the QSO-LBG clustering has been studied is $z \sim 4$ (García-Vergara et al., 2017), who obtained $r_0^{QG} = 8.83h^{-1}$ cMpc with a fixed slope $\gamma = 2.0$. In Figure 2.9 we show the excess of LBG galaxies as a function of the radius surrounding the $z = 7.54$ quasar target of our study assuming no evolution of the QSO-LBG cross correlation between $z = 4$ and $z = 7.5$ (830 Myr) and a comoving line-of-sight distance corresponding to the redshift range $\Delta_z = \pm 0.1$ from the quasar's redshift. We obtain a 28% LBG excess, making this a marginally overdense quasar field. However, we are still limited by low number statistics, and we are not fully able to discard that the field around ULAS J1342+0928 is consistent with the cosmic density, or that it is even underdense. Therefore, a larger area coverage or optimal set of filters to improve the completeness of LBGs, and spectroscopic confirmations of the redshift would be necessary to confirm an overdensity around this quasar.

2.6.3 *Confirming the Potential Overdensity*

Solely using photometry permits to identify galaxies with very large redshift uncertainties ($\Delta z \sim 1$, $\Delta d \sim 130$ comoving Mpc). Therefore, spectral redshift confirmations would ultimately constrain the presence of an overdensity, and whether it would trace a protocluster (Harikane et al., 2019). First one needs to find galaxy candidates with an optimal setup of photometric bands in order to better constrain the $\Delta z \sim 1$ uncertainty. Adding filters filling the gap of photometric information at longer wavelengths than J_{125} would better complete the survey to appropriately select galaxies at $z \sim 7.5$. This could be achieved with *HST* or *JWST* near-infrared filters.

JWST observation from program GTO 1219 (PI: Luetzgendorf) will aim at confirming the LBG candidate C-4636 at $z \sim 7.5$ using NIRSpec MSA spectroscopy. The observations will cover 0.7µm to 3.1µm with the G140H/F070LP and G235H/F170LP grating and filter combination. This setup will allow confirmation of the Lyman-break at $z \sim 7.5$ from the galaxy, while also observing potential UV metal emission lines such as C IV λ1549, C III] λλ1907,1909 and Mg II λ2798 that would characterize the ionization and chemical enrichment of the galaxy (e.g. Hutchison et al., 2019).

Moreover, the close physical distance from the quasar to candidates C-[C II] (27 pkpc), and to C-4636 (223 pkpc) indicates a strong clustering factor, suggesting the presence of more galaxies in a protocluster that can extend up to 10 comoving-Mpc (Overzier, 2016; Chiang, Overzier, and Gebhardt, 2013). It would therefore be neces-

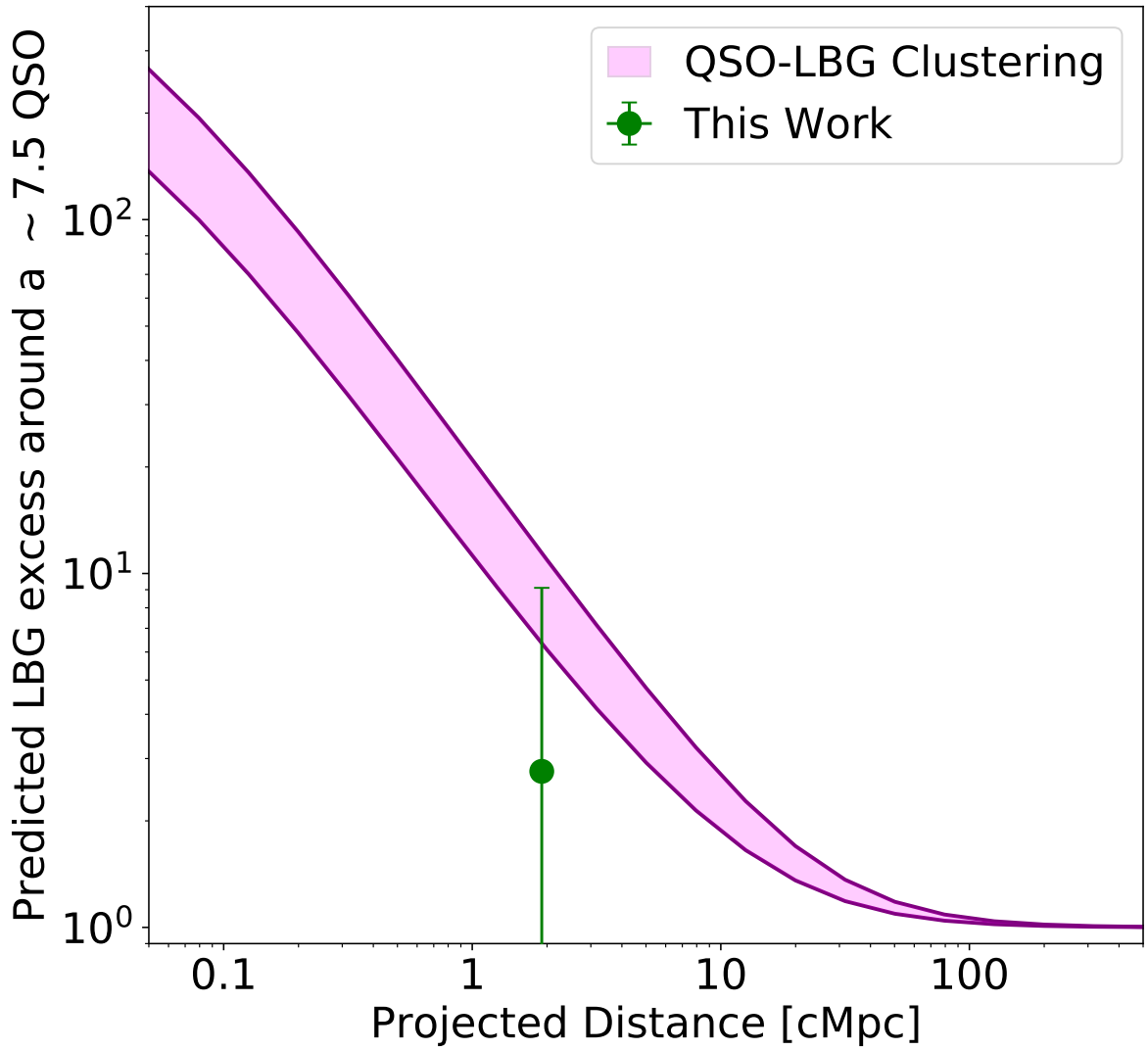

Figure 2.9: Predicted LBG excess as a function of radius around our quasar at $z = 7.54$. The pink curve represents the LBG excess taking into account the uncertainty on the determination of the QSO-LBG clustering cross-correlation r_0^{QG} from García-Vergara et al., 2017 assuming no evolution between $z = 4$ and $z = 7.5$, or cosmic variance. Accounting for our completeness and the LBG we found at $z = 7.69$ with projected distance to the quasar of 223 pkpc (1.9 cMpc), we calculate a 28% LBG excess which is in agreement with a marginally overdense quasar field (green circle with 1σ errors from Gehrels 1986). We note that our result is limited by low Poisson statistics.

sary to survey a wider area to select and confirm galaxies around the quasar to probe protocluster structure.

2.6.4 *Implications Refuting an Overdensity in the Quasar Environment*

Even though simulations show that massive quasars such as ULAS J1342+0928 are good indicators of galaxy overdensities, the opposite has also been observed (e.g. Bañados et al., 2013; Simpson et al., 2014; Mazzucchelli et al., 2017a). There is no evidence for an evolutionary trend of overdensities with redshift as for example Mignoli et al., 2020 found both LBGs and LAEs in the environment of a quasar at $z = 6.31$. On the contrary, Goto et al. 2017 did not find any LAEs around a $z = 6.4$ quasar and points out to the possibility that the quasar formation drains out the available matter within the ~ 1 pMpc. There are indeed many physical processes at play in the formation of a quasar and its environment. Possible methods of oppression are for instance UV radiation from the quasar suppressing the formation of galaxies within 3 pMpc (i.e., within the proximity region) (e.g. Ota et al., 2018).In a different scenario, supernova-driven galactic winds could simply sparse the galaxies further away from the quasar and thus reduce the number density observed (e.g. by a factor of up to 3.7 in the *HST*/ACS area; Costa et al. 2014). Finally, there is also the possibility of the environment being fully dominated by dust-obscured galaxies and no LBGs or LAEs can be found with traditional photometric techniques. In order to probe this for the ULAS J1342+0928 field, further ALMA observations could unveil this population of galaxy candidates and explore more of their chemical properties and/or rest-frame optical observations with JWST e.g Decarli et al., 2017; García-Vergara et al., 2022.

2.6.5 *Galaxy-Absorber Association at $z \sim 6.8$*

The analysis of the $z = 6.84$ absorber detected in the spectrum of ULAS J1342+0928by Simcoe et al. (2020) suggests that this system may be classified as a Damped Lyman Alpha (DLA) system with a fiducial column density of $N_{HI} = 10^{20.6}\,cm^{-3}$ (Simcoe et al., 2020). Galaxies originating such absorbers at $z \sim 4$ are typically located at impact parameters of $\lesssim 50$ pkpc (e.g., Neeleman et al., 2017; Neeleman et al., 2019). However, recent studies based on $z < 2$ MgII ($\lambda\lambda 2796, 2803$Å) absorbers, showed that group environment may give rise to stronger and more widespread absorption systems (e.g., Nielsen et al., 2018; Fossati et al., 2019; Dutta et al., 2020). If this behavior holds at high redshift (see Doughty and Finlator, 2023, for implication on the end of the reionization on absorption systems), this can explain the relatively large impact parameters observed for our two candidates C-4966 and C-5764 (274 pkpc, 452 pkpc, assuming $z = 6.9$, respectively). The two $z \sim 6.9$ galaxy candidates need to be spectroscopically confirmed to establish the physical link with the metal absorption system detected at $z \sim 6.8$ by Simcoe et al. (2020).

2.7 SUMMARY

In the beginning of this Chapter we described the importance of studying the environment of high-redshift quasars hosting SMBHs to understand their large-scale structure. These quasars are often targeted to look for galaxy overdensities. We present the results of a search for Lyman-break galaxy candidates (LBGs) in the environment of the $z = 7.54$ quasar ULAS J1342+0928. We used *HST*+*Spitzer*/IRAC observations designed to look for LBGs in the ~ 1 proper-Mpc^2 environment of the quasar. This area covered is defined from the *HST*ACS/WFC large FOV obtaining observations in the i_{814} band, and a 2×2 mosaic centered around the quasar is constructed with WFC3 Y_{105} and J_{125} bands. This *HST* filter set up is used to find LBGs using the photometric redshift technique while the *Spitzer*/IRAC 3.6 μm and 4.5 μm photometry serve to constrain the high-redshift solution of the galaxies selected.

For this search, we calculate the photometry in elliptical small Kron apertures and $0''.4$ circular apertures using `Source Extractor`. However, we manually measure the noise in our *HST*images and apply it to calculate the flux errors for all sources in our catalog with the selected apertures. In order to avoid losing candidates from strict color-color cuts, we rely on redshift probability calculations with `EAZY` based on the best-fit SED to the available photometry in the small Kron apertures. The final catalog of galaxy candidates results from setting criteria on $0''.4$ circular apertures where $S/N_i < 2$ and $S/N_J > 5$, as well as constraints from the `EAZY` best-fit results. We first constrain the catalog with galaxies whose integrated probability distribution is over 60% at $z > 6$. Specifically to include LBGs at $z \sim 7.5$, the probability distribution $P(7 < z < 8)$ has to dominate over the distributions at neighboring redshifts. Finally, artifacts and low-redshift contaminants in the catalog are discarded after doing a visual inspection and a comparison of the best-fit $\chi^2_{lowz} - \chi^2_{highz}$ solutions. Our results show that:

- The final catalog results in the recovery of the quasar and one LBG with magnitude $J_{125} = 26.4$ just 223 pkpc in projection from the quasar, which is a strong indication for Quasar-Galaxy clustering (e.g. Farina et al., 2017; Meyer et al., 2022). An additional candidate associated with the environment of ULAS J1342+0928 that had been previously identified in Venemans et al. (2020) is not detected in either of the five bands used in this work. Nevertheless, this is still a potential dust-obscured star-forming galaxy at $z = 7.5$ just 27 pkpc in projection from the quasar.

  Galaxy candidates at lower photometric redshifts $z = 6.91$ and $z = 6.89$ are identified in the data set and, interestingly, are at a redshift that is consistent with a $z = 6.84$ absorber in the line of sight previously identified in the quasar spectra in Simcoe et al. (2020).

- The completeness of galaxy candidates found at $z \sim 7.5$ in our survey compared to blank fields from GOODS in Finkelstein et al. (2015) proves to be sub-optimal given the low recovery fraction even at the brightest magnitudes $J_{125} > 26.5$ of

$\sim$ 40%. This low completeness can be explained by the fact that a $z \sim 7.5$ LBG begins to drop-out half-way through the Y_{105}, biasing results to candidates with red $Y - J$ colors. Notwithstanding, the new LBG candidate at $z \sim 7.5$ hint at an overdensity with a 0.9σ significance in this surveyed area, as compared to the expected number density in the blank fields as portrayed in the rest-UV luminosity function. Moreover, there is a [C II]-emitter at $z = 7.5$ that even though is not UV-bright, is a dust-obscured galaxy in the environment of the quasar.

The findings from this work are paving the way for follow-up studies that will confirm one of the earliest overdensities in the universe. Spectroscopic confirmation of the LBG candidate at $z \sim 7.5$ will be secured with upcoming *JWST* NIRSpec observations from program GTO 1219. Moreover, this work demonstrates that it is expected to find more galaxy candidates using further *HST* or *JWST* near-infrared observations. Alternatively, ALMA mosaic observations covering the quasar field would investigate the highly possible population of dust-obscured galaxies. In fact, even finding an average or underdense field would contribute to theories of quasar environment formation at the earliest stages in the universe.

3

THE HOST GALAXY OF A POWERFUL RADIO-LOUD QUASAR AT $z = 5.83$

In this chapter, we present the studies on the host galaxy of the radio-loud quasar PSO J352.4034–15.3373 at $z \sim 6$, or at the edge of the Epoch of Reionization (< 1 Gyr). We first motivate the importance of studying this powerful radio emitter and context on its discovery and properties as known before developing this work in §3.1. The observations of the quasar that we use in this work at millimeter wavelengths from ALMA at 290 GHz and from NOEMA at 100 GHz, and at 215 MHz in radio with Giant Metrewave Radio Telescope (GMRT) are described in §3.2-3.4. The analysis of the continuum and emission lines in the ALMA and NOEMA observations in §3.5. We discuss the radio and Far-infrared Radiation FIR properties in §3.6. We present our results and comparison with previous literature in §3.7. The summary and final conclusions are presented in §3.9.

Part of the work in this Chapter has been previously presented in the article Rojas-Ruiz et al. (2021). I led the analysis, results, and writing of this article. Co-author Eduardo Bañados provided guidance through the different parts of this work. The ALMA observations were provided by collaborator Chiara Mazzucchelli, the reduction was performed by Marcel Neeleman, and I performed the analysis and results. I reduced and analyzed the NOEMA data. Collaborator Chris Carilli reduced the GMRT observations and I performed the analysis. I led the rest of the analysis, modeling, and result interpretation. I also contributed to the search for the radio counterpart of the X-ray source identified in Connor et al. (2021). Finally, the other co-authors provided helpful input and comments for the publication of this article.

3.1 PREVIOUS STUDIES ON P352–15

We studied the quasar PSO J352.4034–15.3373 (hereafter P352–15) which had been selected as a quasar candidate from color analysis from the Panoramic Survey Telescope & Rapid Response System 1 (PAN-STARRS1) survey. Follow-up spectral studies in the rest-frame UV by Bañados et al. (2018a) discovered the quasar to be at $z = 5.8$. It was furthermore confirmed that this object was the brightest $z \gtrsim 6$ radio object known at the time through observations with the VLA, with flux densities reaching up

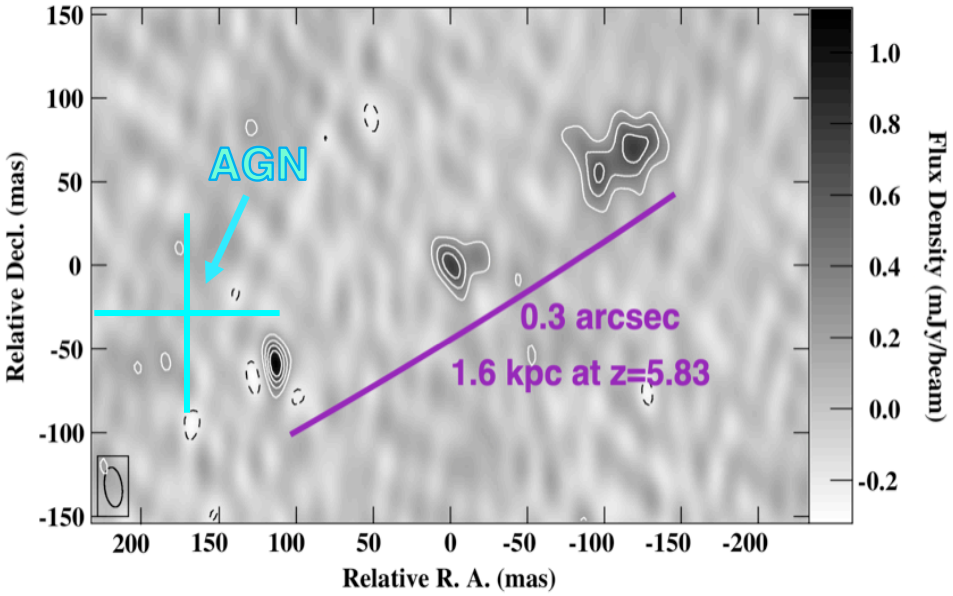

Figure 3.1: VLBA 1.5 GHz of P352–15, revealing three radio hot spots as presented with the contours, supporting evidence for the first time at $z \sim 6$ of an extended radio jet going through shocks with the interstellar medium (adapted from Momjian et al. (2018)). The contour levels are at (-3, 3, 6, 9, 12, 15)σ, where the rms noise level σ is 67 μJy beam^{-1}. The beam resolution on the bottom left is 23.9×1.3 mas resolution (P.A.=8°). The AGN as seen from the optical position of P352–15 is shown with a blue cross, with the error bars as from Momjian et al. (2018). At the redshift of this quasar and using our cosmology defined in §1.1, 1" corresponds to 5.8 proper kpc.

to ~100 mJy at ~200 MHz as measured by the Murchison Widefield Array Murchison Widefield Array (MWA). The only source with comparable radio luminosity at such redshift is a blazar at $z = 6.1$ (Belladitta et al., 2020). Subsequent observations of P352–15 with the Very Long Baseline Array Very Long Baseline Array (VLBA) revealed the first direct evidence of extended (1.62 kpc) radio-jets at $z \sim 6$ (Momjian et al., 2018) (see Figure 3.1). Additionally, Connor et al. (2021) studied this quasar with deep (265 ks) *Chandra* X-ray observations, reporting an X-ray luminosity of $L_{2-10} = 1.26 \times 10^{45}$ erg s^{-1} and a structure aligned with the radio jets but at a distance of 50 kpc away, implying that the jets could affect larger scales than what is currently seen in radio emission (see Connor et al. 2021 for more details).

Next, we wanted to study the host galaxy of this quasar and test whether the jet is affecting the dust or star formation of the host galaxy. We turn to sub–mm observations with ALMA and NOEMA to study the cold dust of the host in rest-frame FIR wavelengths. Moreover, we use additional GMRT observations to constrain order to constrain the synchrotron emission from the jet.

3.2 ALMA OBSERVATIONS

The target source P352–15 was observed with ALMA on 2019 Nov 28 as part of program 2019.1.00840.S (PI: Mazzucchelli) under median weather conditions with a mean precipitable water vapor (PWV) of 1.3 mm. The compact configuration C43-2 with a total of 44 antennas was used, resulting in maximum baselines of 314 m. Blazar J2331–1556 was used as a phase calibrator and blazar J0006–0623 was used to calibrate the flux density scale, which is accurate within 6%. The total time on-source was 756 s. The correlator was set up to observe four spectral windows using 480 channels with a channel width of 3.9 MHz for a total bandwidth of 1.875 GHz per spectral window. Two of the spectral windows were set up to have a slight spectral overlap, and together were centered on the expected frequency of the redshifted [C II] line.

The data were calibrated with the ALMA pipeline, which is part of the common astronomy software application package (CASA; McMullin et al., 2007), using version Pipeline-CASA56-P1-B. A continuum image was made using the task *tclean* within CASA and by applying natural weighting to optimize sensitivity. For this continuum image all channels were used except for the 0.7 GHz spectral region surrounding the [C II] emission. The continuum image has an effective frequency of $\approx$ 290 GHz and a root-mean-square (RMS) noise sensitivity of 0.043 mJy beam^{-1} (see Figure 3.3). We also created a continuum-free line cube by removing the continuum using the task *uvcontsub*, and imaging was done with the *tclean* task. Here, we again adopted natural weighting and a channel spacing of 100 km s^{-1}. The RMS noise sensitivity for this cube is 0.32 mJy beam^{-1} per 100 km s^{-1} channel. The final beam sizes for both the continuum image and line cube are elongated ellipses with FWHM major and minor axis $1\farcs3 \times 1\farcs0$ at a positional angle (PA) of 85.6°.

3.3 NOEMA OBSERVATIONS

P352–15 NOEMA observations were executed to target the CO (6–5) emission line with observed frequency estimated at 101.1 GHz (program: W18EG; PIs: Eilers, Bañados.) All observations were taken on thirteen different visits between 2019 April 10 and 2019 May 31. The observations were taken in the receiver Band 1 (at 3 mm) in the compact configurations of 10D with ten antennae for seven observing days, and the rest were observed in 9D configuration with nine antennae. This set up of observations were taken in compact configuration to maximize the sensitivity. During the different dates, quasars 2243–123/2345–167, and 2145+067/0923+392 were used as phase and amplitude calibrators, respectively. The Radio Frequency (RF) bandpass calibrators included mostly 3C454.3, but also 3C84, 1749+096, and 0923+392. The star MWC 349 was used to set the absolute flux density scale, which is accurate to within 10%. The typical system temperature was (100 – 200) K. The PWV conditions were mostly within PWV $\sim 2-5$ mm, only four visits extending up to PWV $\sim$ 10 mm and one day up to PWV $\sim$ 60mm (where most data was flagged). For each of the days

Table 3.1: Summary of NOEMA Observations of P352–15

Date (2019)	RF Calibrator	Ph/Amp Calibrator	T_{sys} (K)	PWV (mm)
April 10th	3C84	2243–123/2345–167	100–200	5–10
April 18th	3C454.3	2243–123/2345–167	100–160	4
April 20th	3C454.3	2243–123/2345–167	70–100	2
April 21st	1749+096	2243–123/2345–167	100–200	5–10
April 22nd	3C454.3	2243–123/2345–167	100–200	4
April 27th	3C454.3	2243–123/2345–167	100–300	2–4
May 3rd	3C84	2243–123/2345–167	100–200	5–10
May 15th	3C454.3	2243–123/2345–167	70–100	1
May 16th	3C454.3	2243–123/2345–167	100–200	1–10
May 17th	3C84	2145+067/0923+392	100–200	20–60
May 27th	3C454.3	2145+067/0923+392	100–200	4
May 30th	3C454.3	2243–123/2345–167	70–100	1
May 31st	3C454.3	2243–123/2345–167	60–160	4

of observation, we present a summary of calibrators, system temperature (T_{sys}), and PWV in Table 3.1.

The data were reduced at the Institut de radioastronomie millimétrique (IRAM) with the software `CLIC` and `MAPPING` from the GILDAS suite[1]. Using `CLIC` we flag the bad data remaining after the first run of the pipeline done by IRAM, and create the UV-tables. All NOEMA antennas are equipped with 2SB receivers, providing low noise performance and excellent long-term stability. The receivers provide two orthogonal linear polarizations in all three bands. Each of the two polarizations delivers a bandwidth of 7.744 GHz in the lower sideband (LSB) and upper sideband (USB) simultaneously. Therefore, we create UV-tables for LSB and USB, each with 35225 visibilities corresponding to a total ~ 20 hrs of observation. Due to the elevation of our source, there was often shadowing, mainly in Antenna 4 and Antenna 1. The total 9 antennae equivalent time on source is 12.2 hrs. The CO (6–5) emission line is only covered by the USB band and therefore we continue the reduction with this data set. The final UV-plane coverage is presented in Figure 3.2.

The UV-tables are cleaned and further analyzed with `MAPPING`. The UV data is given 386 channels each with an increment velocity of 59 km s^{-1}, or 20 GHz. The primary beam is 49.9 radians, or $7\farcs62 \times 4\farcs01$ at PA = 5.20°. We use the UV-table file to compute a tailored dirty beam and dirty image. We apply natural weighting in order to maximize sensitivity. The RMS noise for this cube is 0.258 mJy beam^{-1} per 59 km s^{-1} channel. We clean the image with the Hogbom algorithm, which makes successive tries of deconvolution to ensure deep enough cleaning. Using the com-

1 https://www.iram.fr/IRAMFR/GILDAS/

mand LMV-CLEAN, we visualize the cumulative flux as a function of the number of found clean components to inspect the cleaning convergence.

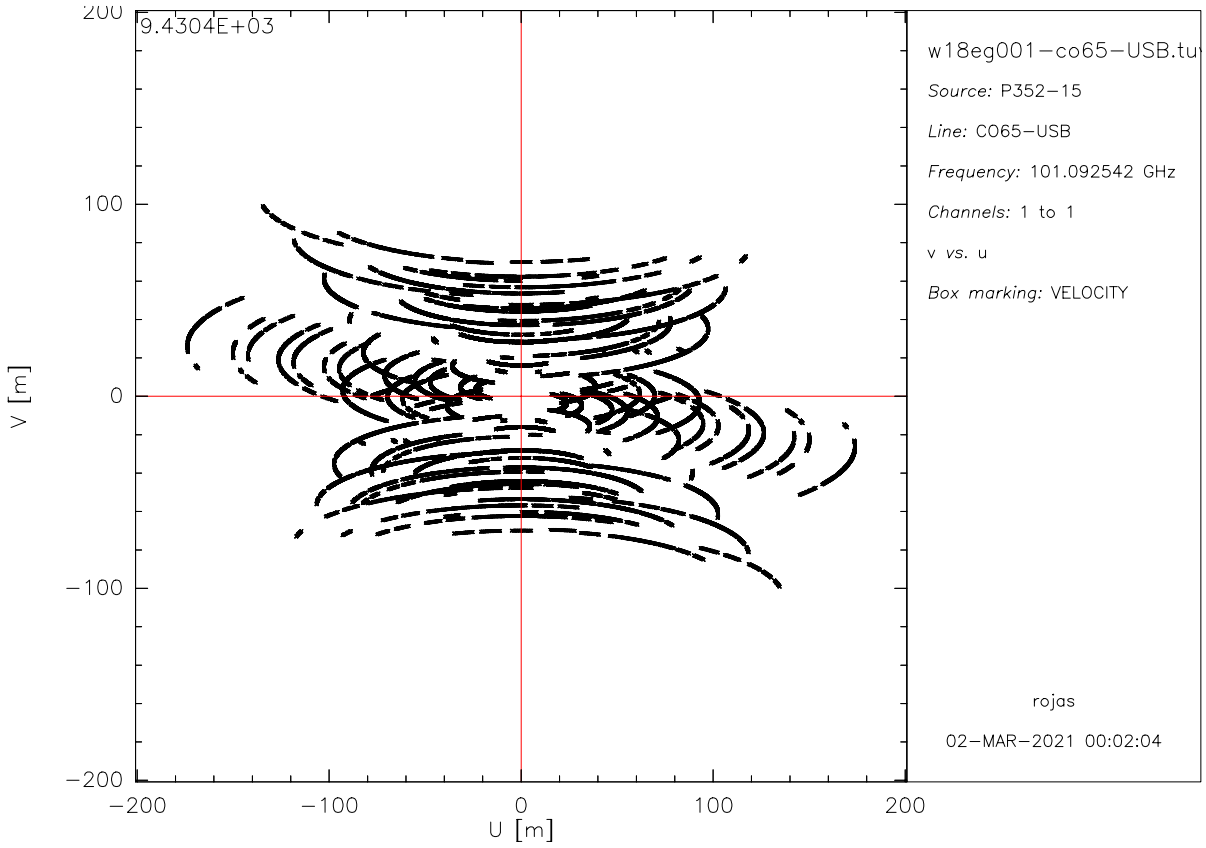

Figure 3.2: This is the UV-plane resulting from the calibrations performed with `CLIC` in the USB band, where we expect to find the CO (6–5) emission from the host galaxy of P352–15. This plane presents the coverage of our observations in U and V as measured in meters (m). The more filled this UV-plane is, the more observations contribute to the Fourier analysis to image and deconvolve the data. Thus, this UV-plane is the basis to create the final multichannel image, or cube, using the `MAPPING` tool for Fourier transform analysis.

The resulting cleaned spectrum does not show clear evidence of CO (6–5) emission line. For this reason, we resample the UV data with 50 channels, with 25 as the new reference pixel and set it at 0 km s^{-1}. Finally, each channel has a velocity increment of 300 km s^{-1} (equivalent to -101.16 GHz.) The new measured RMS for the cube with 300 km s^{-1} channel spacing is 0.10 mJy $beam^{-1}$ per channel, and a synthesized beam size of $7\farcs3 \times 3\farcs8$ and PA of 5.44°. The imaging from the new resolution of 300 km s^{-1} is not optimal to look for the CO (6–5) emission line and therefore we resample the data again. The new resampling of the UV data is with 150 channels, the new reference pixel (75 in this case) setting it at 0 km s^{-1}, and each channel with a velocity increment of 100 km s^{-1} (equivalent to 33.72 GHz.) We apply the same natural weighting and obtain an RMS for the new cube of $\sigma = 0.18$ mJy $beam^{-1}$ per 100 km s^{-1} channel. This cube has a beam size of $7\farcs3 \times 3\farcs7$ and PA of 5.41°. From the imaging, it can be concluded that the CO (6–5) emission line is not detected with

these observations but only the underlying continuum of the quasar at 100 GHz (see Figure 3.3).

3.4 GMRT OBSERVATIONS

P352–15 was detected in the GaLactic and Extra-galactic All-sky MWA (GLEAM) survey and the TIFR GMRT Sky Survey (TGSS) at low frequencies (150 MHz to 200 MHz). However, the cataloged flux densities in this range show a wide scatter, with the GLEAM data consistent with 80 to 120 mJy at 200 MHz (Hurley-Walker et al., 2017). The TGSS image shows significant imaging artifacts (stripes), and our reanalysis of the image finds a peak of 110 mJy beam^{-1}, but a total flux density (significantly affected by the stripes) of 169 mJy (Intema et al. 2017; Gasperin, Intema, and Frail 2018).

To clarify the source flux density at low frequency, we observed the source with the GMRT at 215 MHz on 2018 June 23, for four hours. The observations were centered at 215.5 MHz, with a bandwidth of 25 MHz using 16384 channels, for interference excision. The flux density scale was set assuming 52.3 Jy for 3C48 at 215 MHz (Perley and Butler, 2017). Delay and bandpass calibrations were also performed using 3C48. The array gain and amplitudes were tracked in time using the calibrator J2321–163, which had a boot-strapped flux density (from 3C48) of 14.0 Jy. All calibrations were done using standard procedures in CASA (McMullin et al., 2007). Interference was substantial, in particular on short baselines, and the final calibration and analysis employed only baselines longer than 1.5 km.

The final imaging used CASA task CLEAN with Briggs weighting with a robust factor= 0 (Briggs, Schwab, and Sramek, 1999). The resulting synthesized beam was $= 18\farcs0 \times 11\farcs0$, with PA = -48°. The RMS noise on the final image is 4 mJy beam^{-1}. The source was easily identified as seen in Figure 3.3. Gaussian fitting indicated the source was unresolved, with a flux density of 88 ± 7 mJy, whose uncertainty is dominated by the estimated 8% error from the the absolute flux density bootstrap calibration process.

3.5 EMISSION LINE SEARCH AND MM CONTINUUM MEASUREMENTS

In this section, we present a detailed analysis of the host galaxy of P352–15 with the ALMA and NOEMA data at hand. We discuss specifically the analysis to measuring the [C II] emission from ALMA data, and CO (6–5) lines from NOEMA, and their underlying continuum properties (see Table 3.2).

3.5.1 *[C II] Line and 290 GHz continuum*

We use the ALMA continuum-free line cube generated in Section 3.2 to look for the [C II] line. We find that the line is consistent with the expected redshift $z \sim 5.84$ and

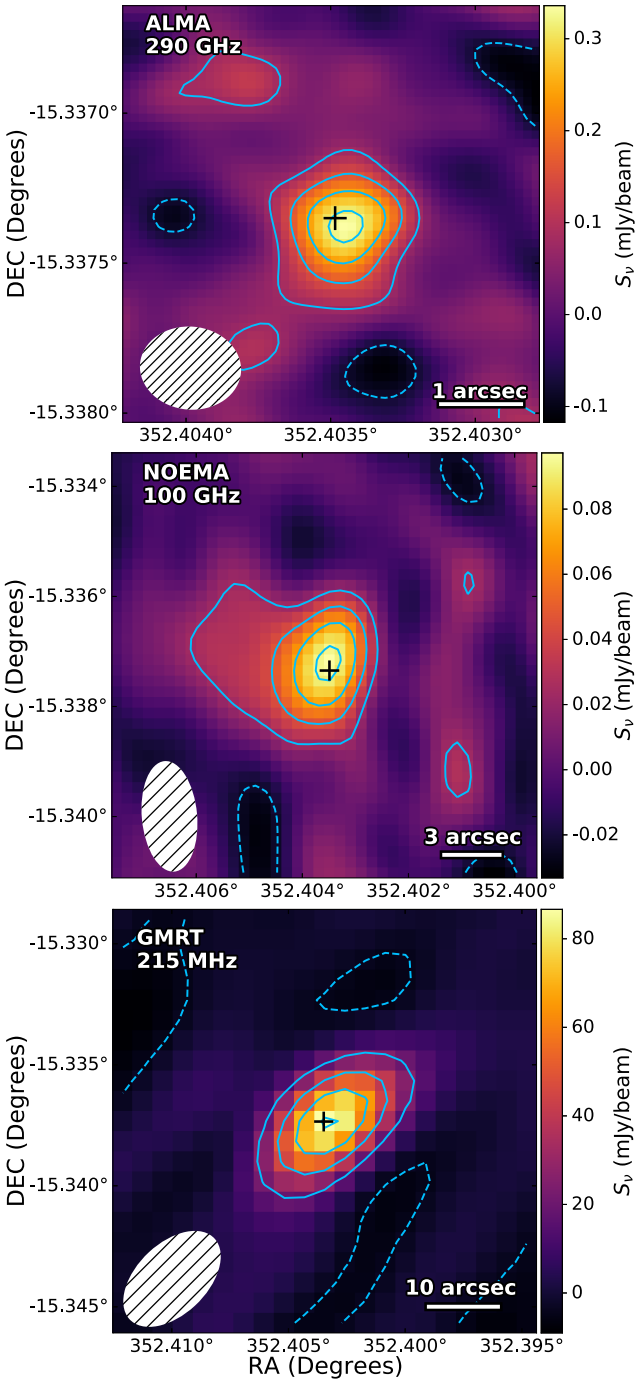

Figure 3.3: *Top:* ALMA 290 GHz continuum emission map of P352–15, with an RMS $\sigma = 0.04$ mJy beam^{-1}. The beam size is $1\farcs3 \times 1\farcs0$ and the quasar is unresolved. *Middle:* NOEMA 100 GHz continuum emission map with $\sigma = 0.01$ mJy beam^{-1}. The beam size is $7\farcs3 \times 3\farcs7$ and the quasar is unresolved. *Bottom:* GMRT 215 MHz emission map with a beam size of $18\farcs0 \times 11\farcs0$ and $\sigma = 4$ mJy beam^{-1}. The quasar appears unresolved. The contour levels for ALMA and NOEMA maps are shown at (−2, 2, 4, 6, 8)σ and both have S/N$>$ 8. The GMRT continuum has contours shown at (−1, 5, 10, 15, 20)σ and has S/N$>$ 20. For all maps, the dashed and solid contours represent the negative and positive σ, respectively. The cross in all panels is centered at the optical position of P352–15 from Momjian et al. (2018).

looks spatially resolved to some extent. Therefore, we perform an aperture photometry test at varying apertures from 1.″0 to 2.″0. We perform a Gaussian fit to the [C II] spectrum and search for the aperture at which the velocity-integrated [C II] emission begins to plateau. This turning point occurs at a radial aperture of 1.″7 (see Figure 3.4).

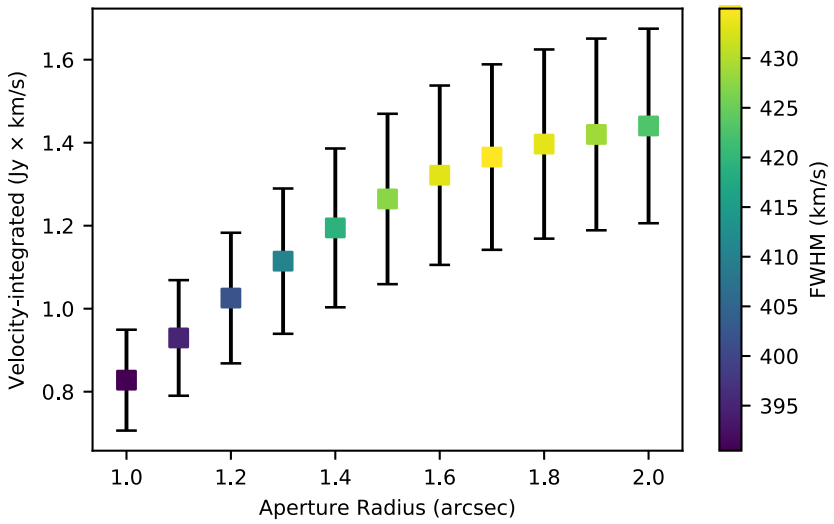

Figure 3.4: Here we present the analysis of the most optimal aperture radius vs. velocity-integrated line to perform the photometry of the [C II] emission from the ALMA observations. The color map represents the FWHM of [C II] at each aperture. This test shows that the velocity-integrated emission begins to plateau with the turning point at 1.″7 of aperture radius, and with the maximum FWHM value of 435 km s^{-1}.

The resulting continuum-subtracted [C II] spectrum is shown in Figure 3.5, which is the [C II] spectrum used in the remaining analysis. From the Gaussian fit, we find that the [C II] emission line has a FWHM of 440 ± 80 km s^{-1} and the line peaks at an observed frequency of 278.20 ± 0.03 GHz (see Figure 3.5, left). Using this value and the rest frame frequency of [C II] (1900.5369 GHz; Schöier et al., 2005), we calculate the systemic redshift of P352–15 to be $z = 5.832 \pm 0.001$. The flux density peak is 2.95 ± 0.48 mJy and the velocity-integrated line is 1.37 ± 0.22 Jy km s^{-1}. To generate a [C II] map, we re-imaged the data cube using channels within 1.2×FWHM of the [C II] emission line which, given our observations, corresponds to the green shaded channels in Figure 3.5. Using this channel spacing maximizes the signal-to-noise on the emission line and recovers 84% of the flux emission, assuming it is Gaussian (see Appendix A in Novak et al., 2020). The [C II] map is shown in the right panel of Figure 3.5 and has an RMS of 0.15 mJy $beam^{-1}$. We note that the beam size is 1.″3 × 1.″0 and therefore does not resolve the radio jet revealed by the VLBA, which extends over 0.″28 (see Momjian et al. 2018).

The [C II] map shows an extended morphology that we fit with a 2D Gaussian profile using CASA. The result is a deconvolved source with major and minor axes of sizes 2.″0 × 0.″8 and position angle 96°, confirming that the [C II] emission of the

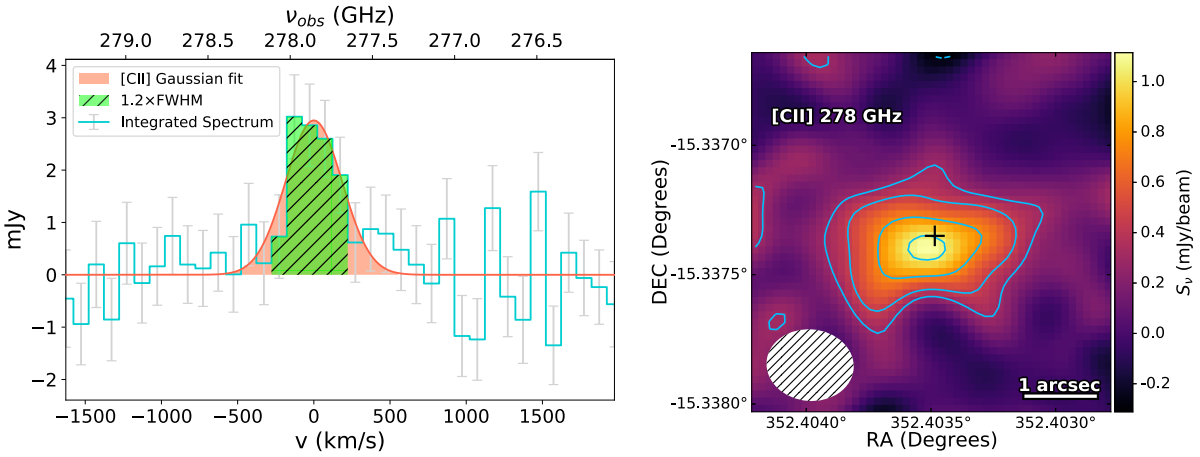

Figure 3.5: *Left:* ALMA continuum-subtracted [C II] emission of P352–15. We use a 1.″7 aperture radius to extract the emission line spectra presented here in blue. The error bars represent the RMS within the aperture at each channel. The spectral range used for the Gaussian fit of [C II] is shaded in orange and corresponds to a velocity-integrated value of 1.37 ± 0.22 Jy km s^{-1}. The [C II] fit at peak has a flux density of 2.95 ± 0.48 mJy. The hatched area in green corresponds to ≈ 1.2 ×FWHM of the Gaussian fit and is used to create the [C II] map shown in the right panel. *Right:* 2D map of [C II] built with the data from the channels shown in the left panel in green. The emission is marginally resolved and the contour levels are shown at $(-2, 2, 3, 5, 7)\sigma$ with $\sigma = 0.15$ mJy beam^{-1} where the Beam is 1.″3 × 1.″0. The [C II] line is detected at S/N> 7.5. The cross is centered at the optical position of P352–15 from Momjian et al. (2018).

quasar host galaxy is marginally resolved. Thus, we decide to investigate its morphology from channel-to-channel. Figure 3.6 shows the ALMA channel maps for P352–15 around the observed frequency of [C II], with the dotted white circles denoting the channels and spatial regions used to extract the [C II] flux emission and create the 2D map shown in Figure 3.5. The central panel shows the [C II] emission closest to the peak velocity from the Gaussian fit (-372.57 ± 34.91 km s^{-1}) at -27 km s^{-1} away. This channel and the 72 km s^{-1} centered channel (middle right panel) have the highest signal-to-noise ratio with S/N> 5.

3.5.1.1 *[C II] Moment Maps*

We decide to calculate the moment maps to get a better physical interpretation of the [C II] emission. We follow the methodology often used for high-redshift galaxies, which involves the Gaussian fitting of the spectral line at each spatial position in the cube (e.g. De Breuck et al., 2014; Shao et al., 2017; Venemans et al., 2019). The following analysis is done with `qubefit`[2] routines (Neeleman and Prochaska, 2021). We use the channels containing the [C II] emission and first calculate the mathematical moment 1 and moment 2 corresponding to the velocity and velocity dispersion fields, respectively. We use these as initial guesses to fit a Gaussian to each spaxel, or

2 https://github.com/mneeleman/qubefit

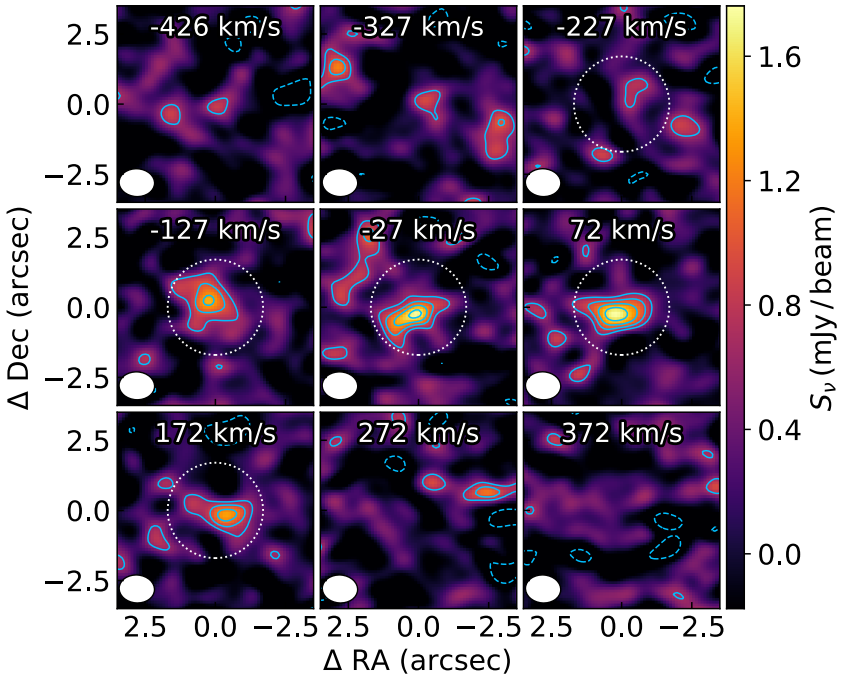

Figure 3.6: ALMA 278 GHz [C II] emission in 100 km s^{-1} channel maps of P352–15. The central map corresponds to the channel closest to the peak velocity at -372.57 ± 34.91 km s^{-1} from the fitted [C II] emission model (orange zone in Figure 3.5). For each panel, the central coordinates correspond to R.A. (J2000) = $23^h29^m36\overset{s}{.}8363$, DEC. (J2000) = $-15°20'14\overset{''}{.}460$, the channel velocities relative to the peak velocity are given at the top, and the synthesized beams are shown at the bottom left. The channels used for flux extraction are presented with a white dotted circle of $1\overset{''}{.}7$ aperture radius. In all maps the contour levels are shown at $(-2, 2, 3, 4, 5)\sigma$ with their respective σ values ~ 0.03 mJy $beam^{-1}$.

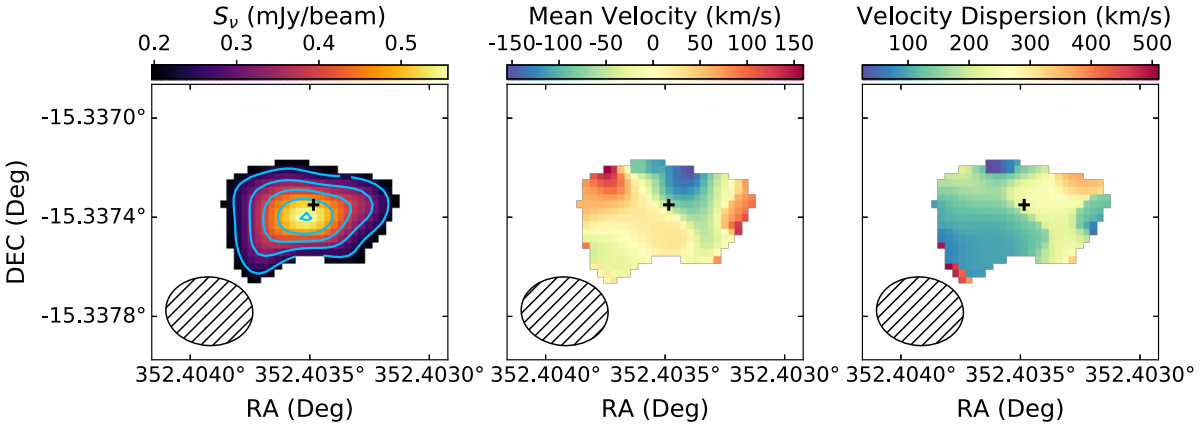

Figure 3.7: The moment maps of the observed ALMA 278 GHz [C II] emission. The zero map presents a high S/N > 7, with the same contours as the emission from Figure 3.5,*Right*. However, since the quasar is only marginally resolved, we cannot fairly analyze the velocity and velocity dispersion fields (moment 1 and moment 2, respectively). In order to obtain fair measurements, more resolved observations at high S/N are needed to determine the velocity gradient of [C II] in the host galaxy of P325–15. The plus sign overlaid is the optical position of the quasar with the uncertainty from Momjian et al. (2018) of ±64 mas in both R.A. and DEC.

spatial element, of the data cube. In this case, the mean of the Gaussian represents the velocity field, and the width of the Gaussian is the dispersion field. Here Neeleman et al. (2021) notes that the result is independent of the chosen initial guess and therefore also from the S/N of the data. These are presented in Figure 3.7.

Despite the [C II] emission being marginally resolved, we do not see any evidence for a velocity gradient or variations in the velocity dispersion across the quasar host galaxy per channel. This is consistent with about a third of all quasar host galaxies at $z \sim 6$, which show no evidence for rotation (Neeleman et al., 2021). However, the current data are insufficient to draw any conclusions on galaxy dynamics. Higher spatial resolution and S/N observations are needed to determine the true velocity structure of the [C II] emission line in this quasar host galaxy.

Finally, we utilize the reduced ALMA continuum cube (refer to Section 3.2), to measure the underlying continuum at 290 GHz. The emission is unresolved with a flux density of 0.34 ± 0.04 mJy (see Figure 3.3, top).

3.5.2 *CO (6–5) Line and 100 GHz continuum*

As previously described in Section 3.3, we do not find a significant detection of the CO (6–5) molecular emission line in either of the NOEMA cubes at 300 km s^{-1} and 100 km s^{-1} sampling. In order to estimate an upper limit on the CO (6–5) luminosity, we use the cube with the 100 km s^{-1} velocity increment and assumed that the line has the same FWHM as the measured [C II] emission line. We find a 3-σ upper limit of 0.35 mJy, which corresponds to $L_{CO(6-5)} < 0.5 \times 10^9$ $L_\odot$. This upper limit is

Table 3.2: Measurements from Line Emission Search

$S_{[C\,II]}$	2.95 ± 0.48 mJy
$S_{[C\,II]}\Delta v$	1.37 ± 0.22 Jy km s^{-1}
$FWHM_{[C\,II]}$	440 ± 80 km s^{-1}
$EW_{[C\,II]}$	2.12 ± 0.42 µm
$z_{[C\,II]}$	5.832 ± 0.001
$S_{CO(6-5)}$	< 0.35 mJy

comparable to the median values for CO (6–5) measured in $z > 6$ radio-quiet quasars (e.g., Venemans et al., 2017b). The 100 GHz continuum emission is clearly detected and unresolved with a flux density of 0.10 ± 0.01 mJy (Figure 3.3).

3.6 THE SPECTRAL ENERGY DISTRIBUTION OF P352–15

In this section we build the spectral energy distribution (SED) for P352–15 by making use of the data presented in this paper and previously reported optical data from Gemini/GMOS r′, Pan-STARRS1 *i*, *z*, *y* bands and Magellan/FourStar J band, and radio observations with the VLA at 3.0 and 1.4 GHz (see Bañados et al., 2018a; Connor et al., 2021). In the following subsections, we will investigate the FIR properties of the quasar and will refine its radio properties. We summarize all existing measurements in Table 3.3 and Figure 3.8.

3.6.1 *Modeling the Radio Emission*

The radio-continuum spectrum is dominated by synchrotron emission at rest-frame frequencies $\lesssim$ 10 GHz, where the thermal bremsstrahlung (free-free) emission is weak (Duric, Bourneuf, and Gregory, 1988). Free-free emission becomes significant at higher frequencies which for this quasar results in a negligible contribution ($\ll$ 1µJy) for the study of the SED (e.g., Venemans et al., 2017a; Yun and Carilli, 2002). As shown in Figure 3.8, the synchrotron radiation of P352–15 is well described as a simple power law of the form $S_\nu \propto \nu^\alpha$, where S_ν is the observed flux density at the frequency ν and α is the radio spectral index. In Bañados et al. (2018a) the synchrotron power-law slope was not well constrained because of the large scatter at the lower-frequency observations. Bañados et al. (2018a) assumed two cases for their analysis with radio slope index $\alpha_{1.4}^{0.150} = -0.89$ and -1.06. With our higher S/N GMRT data (see Section 3.4), we can obtain a more robust measurement of the synchrotron radio slope. We fit a power law to the data from the VLA observed frequencies 3 GHz, 1.4 GHz, and GMRT 215 MHz, resulting in a radio spectral index of $\alpha_3^{0.215} = -0.88 \pm 0.08$ (see Figure 3.8).

The new spectral index presented here allows for an improved calculation of the radio-loudness of P352–15. We adopt the definitions for radio-loudness, for which a source, like a quasar, is considered radio-loud when $R_{4400} = f_{\nu,5\,GHz} / f_{\nu,4400\,Å} > 10$ or $R_{2500} = f_{\nu,5\,GHz} / f_{\nu,2500\,Å} > 10$ (Sramek and Weedman, 1980; Kellermann et al., 1989). From our power-law fit we calculate a flux density of 3.87 ± 0.10 mJy at rest-frame 5 GHz. We use the $L_{4400\,Å}$ reported in Bañados et al. (2018a) and convert it to flux density and find $f_{\nu,4400\,Å} = (3.53 \pm 0.89) \times 10^{-3}$ mJy. We therefore calculate the radio-loudness $R_{4400} = 1100 \pm 280$, which agrees with the $R_{4400} \gtrsim 1000$ reported in Bañados et al. (2018a). Similarly, from the $L_{2500\,Å}$ we calculate $f_{\nu,2500\,Å} = (2.63^{+0.19}_{-0.16}) \times 10^{-3}$ mJy, and measure $R_{2500} = 1470^{+110}_{-100}$.

Although the radio-loudness of P352–15 is extreme and similar to those observed in blazars (e.g., Belladitta et al., 2020; Belladitta et al., 2019; Sbarrato et al., 2012; Romani et al., 2004), its X-ray properties (Connor et al., 2021) confirm its quasar nature. The parameters of the X-ray-to-optical index $\alpha_{ox} = -1.45 \pm 0.11$, and the photon index $\Gamma = 1.99^{+0.29}_{-0.28}$ fall under the quasar classification although near the threshold of high-redshift blazars from Ighina et al. (2019) where a blazar has $\tilde{\alpha}_{ox}$[3] < 1.355 and $\Gamma < 1.8$. Typically, the photon index is $\Gamma \geqslant 1.5$ for high-redshift quasars even up to $z \gtrsim 6$ (e.g., Nanni et al., 2018). Additionally, the radio jet orientation of P352–15 not pointing along our line of sight (Momjian et al., 2018) and the steep radio slope ($\alpha_3^{0.215} = -0.88 \pm 0.08$; see Figure 3.8) are inconsistent with this quasar being a blazar.

3.6.2 *Modeling the mm Emission*

In this work we present two mm-continuum measurements of P352–15 from ALMA 290 GHz and NOEMA 100 GHz observations with S/N$>$ 8 (see Figure 3.3), corresponding to the quasar's rest-frame frequencies of 1981 GHz and 683 GHz, respectively. The flux densities at these frequencies are consistent with being at the Rayleigh–Jeans tail (optical depth $\tau_{Dust} << 1$) of a Modified Black Body (MBB), thought to be a good representation of cold dust from the quasar host galaxy (e.g., Priddey and McMahon, 2001; Beelen et al., 2006; Cunha et al., 2013; Leipski et al., 2014; Venemans et al., 2016; Venemans et al., 2018). The Planck function is:

$$B_{\nu_{rest}}(T_{Dust,z}) = \frac{2h\nu_{rest}^3/c^2}{e^{(h\,\nu_{rest}/k\,T_{Dust,z})} - 1} \tag{3.1}$$

where $T_{Dust,z}$ is the dust temperature at a given redshift. Typical dust parameters of the MBB found for host galaxies of radio-quiet quasars are $T_{Dust} = 47$ K and dust emissivity spectral index $\beta = 1.6$ (e.g., Beelen et al., 2006; Venemans et al., 2016). In the following analysis, we will assume these best-fit parameters and check whether they represent the properties of this quasar known to have a strong radio emission.

3 $\tilde{\alpha}_{ox} = 0.789\alpha_{ox} + 0.212(\Gamma - 1.0)$

Table 3.3: Flux densities and derived properties of P352–15

Telescope/Band[a]	Central λ/ν	Flux Density
Gemini–N/GMOS r	630 nm	0.17 ± 30 μJy
Pan–STARRS1 i_{P1}	752 nm	1.8 ± 0.5 μJy
Pan–STARRS1 z_{P1}	866 nm	11.8 ± 0.7 μJy
Pan–STARRS1 y_{P1}	962 nm	13.6 ± 1.5 μJy
Magellan/FourStar J	1242 nm	14.6 ± 0.4 μJy
ALMA Band–7	290 GHz	0.34 ± 0.04 mJy
NOEMA Band–1	100 GHz	0.10 ± 0.01 mJy
VLA–S	3 GHz	8.20 ± 0.25 mJy
VLA–L	1.4 GHz	14.9 ± 0.7 mJy
GMRT Band–235 MHz	215 MHz	88 ± 7 mJy
Rest Frame Luminosity L ($L_\odot$)		
$L_{5\,\mathrm{GHz}}$		$10^{10.28\pm0.01}$
$L_{4400\,\text{Å}}$		$10^{12.37\pm0.11}$
$L_{2500\,\text{Å}}$		$10^{12.49\pm0.03}$
Radio Loudness		
R_{4400}		1100 ± 280
R_{2500}		1470^{+110}_{-100}

a As mentioned before in §3.1, this quasar was discovered in follow-up of PAN-STARSS1 and therefore we use the bandpass parameters from Tonry et al., 2012. For FourStar camera in the 6.5m Baade telescope at Las Campanas, we get the central value from Persson et al., 2013.

Later on, we will also explore whether different values of T_{Dust} and β can provide a better representation of the existing data of P352–15.

The predicted observed flux density from dust heating can be calculated with the MBB following Novak et al. (2019):

$$S_{obs} = f_{CMB}\ [1+z]\ D_L^{-2}\ \kappa_{\nu_{rest}}(\beta) \times M_{Dust}\ B_{\nu_{rest}}(T_{Dust,z}) \tag{3.2}$$

Here, f_{CMB} is a correction against the Cosmic Microwave Background (CMB) contrast, D_L is the luminosity distance, $\kappa_{\nu,rest}(\beta)$ is the dust mass opacity, which depends on the dust emissivity spectral index β, and M_{Dust} is the dust mass. All values are given in SI units.

The f_{CMB} term corrects for CMB contrast and heating effects, which can be significant at these high redshifts as we are seeing fluxes at frequencies close to the peak of the CMB (see Cunha et al., 2013). However, we do not include a CMB heating correction in Equation 4.1 as this effect is still not significant for $T_{Dust,0} = 30 - 100\,K$ at $z = 5.832$ (including CMB heating changes the temperature in that range by $< 0.3\,K$). Thus, f_{CMB} in Equation 4.1 is only the correcting factor for CMB contrast where the blackbody calculated with the temperature of the CMB at the redshift of the source is divided by the blackbody at the dust temperature:

$$f_{CMB} = 1 - \frac{B_{\nu_{rest}}\ (T_{CMB,z})}{B_{\nu_{rest}}\ (T_{Dust,z})} \tag{3.3}$$

For $z = 5.832$ and $T_{Dust} = 47\,K$, f_{CMB} corresponds to 0.96 and 0.79 for the ALMA 290 GHz and NOEMA 100 GHz continuum points, respectively.

We assume for $\kappa_{\nu,rest}(\beta)$ the relation derived in the submillimeter at 850 µm in Dunne et al. (2000) and James et al. (2002):

$$\kappa_{\nu_{rest}}(\beta) = 0.077\ (\nu_{rest}\ /\ 352\ GHz)^{\beta}\ m^2\ kg^{-1} \tag{3.4}$$

We scale the MBB (Equation 4.1) to match the observed ALMA 290 GHz continuum and obtain a dust mass value of $(0.36 \pm 0.04) \times 10^8\ M_\odot$. We note that if instead of using Equation 3.4 we assume $\kappa_{\nu,rest} = 2.64\ m^2\ kg^{-1}$ at $\nu_{rest} = c/(125\ \mu m)$ as presented in Dunne, Eales, and Edmunds (2003), the value of M_{Dust} would decrease by a factor of 1.6.

Using the calculated dust mass value and Equation 4.1, we can model the MBB at different frequencies. This model predicts a flux density of 0.0139 mJy at 100 GHz, while our NOEMA measurement is 0.10 mJy. Therefore, these values are inconsistent by an order of magnitude and are 7.6σ off from the observed NOEMA flux density. Since neither value set is able to fit the MBB function to both ALMA and NOEMA continuum measurements, we explore the different MBB functions that can be obtained when varying T_{Dust} = 30 K – 100 K, and $\beta = 1.6$ and $\beta = 1.95$ as shown in Figure 3.8. We also try to find a β value that could fit both of our mm-continuum points. This results in $\beta = -0.7$, however, such a negative dust emissivity index has

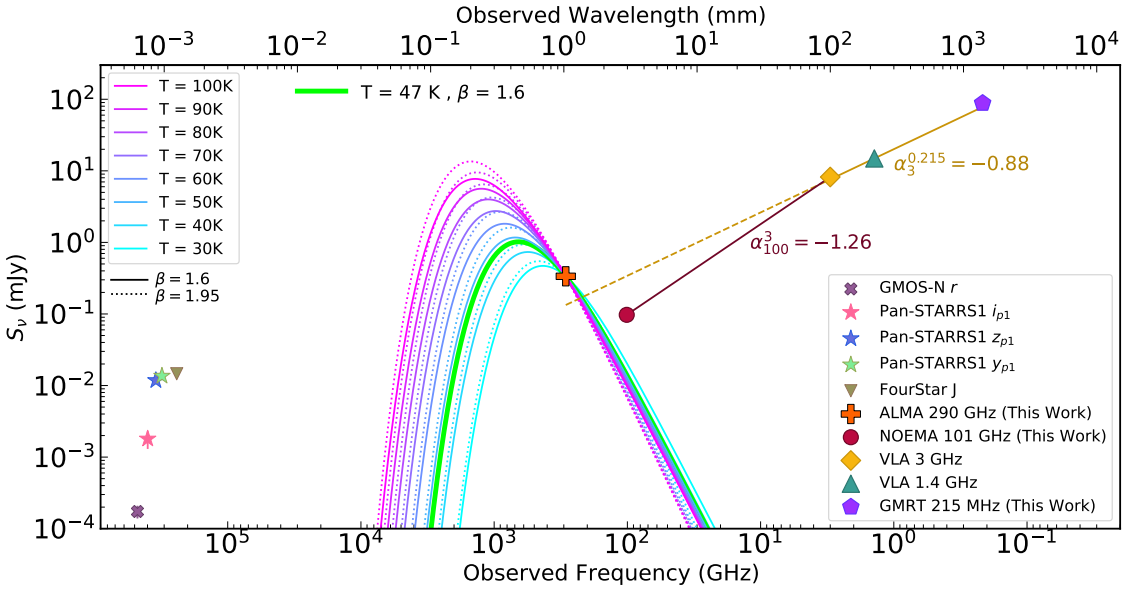

Figure 3.8: Optical, millimeter and radio spectral energy distribution (SED) of P352–15 at $z = 5.832$. The millimeter ALMA and NOEMA measurements are inconsistent with cold dust modeled as a modified black body at different dust temperatures and dust emissivity spectral indexes. The radio data at 215 MHz–3 GHz are well described by synchrotron emission with a power law slope $\alpha = -0.88$. However, extrapolating that power law (dashed line) would be inconsistent with the millimeter data. To explain this SED, the synchrotron emission must steepen or break at high frequencies. We note that the error bars from the measurements are small compared to the scale of the figure and thus are not shown in the image.

never been reported for dust in galaxies (see e.g., Dunne et al., 2000; Beelen et al., 2006).

It is evident that none of these models can reproduce our data, implying that in this system the mm-emission is not only due to cold dust but must be affected by an additional source, the main suspect being the strong synchrotron emission of the quasar, as discussed below.

3.7 DISCUSSION

The work described in this chapter resulted in an intriguing SED of the radio-loud quasar P352–15. In this section, we discuss the implications of our findings. We first describe the possible influence of synchrotron emission up to higher frequencies, which are usually dominated by the dust continuum. Next, we report the derived far infrared (FIR) properties for the quasar based on the mm continuum measured with ALMA at 290 GHz, assuming that this measurement is not contaminated by synchrotron radiation.

3.7.1 *Effects of the synchrotron emission on the mm continuum measurements.*

From the observations described in this work, we see that the radio spectrum is clearly defined by the power-law slope of $\alpha_3^{0.215} = -0.88 \pm 0.08$. However, the continuum emission at millimeter wavelengths is not well-matched to a blackbody fit (Figure 3.8). Given the strong radio emission in this quasar, a possible explanation would be that the millimeter emission is highly affected by synchrotron radiation instead of being only due to cold dust (e.g., Weiß et al., 2008).

In order to assess this possibility, we use the synchrotron power-law fit derived in Section 3.6.1 and extrapolate it to the mm data points. We would expect the extrapolated flux at 100 GHz to be above the measured NOEMA continuum, but the flux density at 290 GHz would be below the measured ALMA continuum (see dashed line in Figure 3.8). When evaluating the slope between the VLA 3 GHz and NOEMA 100 GHz flux density values, the observed spectral index is much steeper ($\alpha_{100}^3 = -1.26 \pm 0.03$) than $\alpha_3^{0.215}$. This means that extrapolating the synchrotron power-law we would have expected a NOEMA detection about three times brighter than what we measure. Therefore, it is very likely that the 100 GHz emission in this quasar is dominated by synchrotron emission. Further measurements between 3–100 GHz are required to pinpoint the location of an expected spectral break.

Extrapolating the synchrotron power-law ($\alpha_3^{0.215} = -0.88$) all the way to 290 GHz results in 0.13 mJy. This implies that the synchrotron contribution in the ALMA measurement could be up to 40% of the measured value. However, this is a strict upper limit given that we know there is a break in the power-law spectrum between 3 and 100 GHz (Figure 3.8). If we extrapolate to 290 GHz using the $\alpha_{100}^3 = -1.26$ power-law, we expect a synchrotron contribution of only 8% in the ALMA continuum measurement.

Due to the significant synchrotron contribution for the NOEMA 100 GHz observations, and a smaller influence on the ALMA 290 GHz, we explore an overall fit of the synchrotron emission and the cold dust, to model both components of the SED simultaneously from the radio to mm regime. For this purpose, we tried to fit the modified black body function (MBB) and a simple power-law function, but this model cannot reproduce our data. We then performed a joint fit using an MBB and a broken power-law and fix the break frequency at 3 GHz, that is the limit of our observations in radio. The resulting model is over-fitted given the few data points and the fitted parameters do not yield trusting values. Since more observations at complementary frequencies are needed to determine the break frequency, we continue to constrain the two components in mm and radio separately. In Chapter 4 we explore different models to fit the SED of P352–15 using more data points from the VLA between the gap of 3 GHz – 10 GHz.

3.7.2 *FIR properties of P352–15*

We use the ALMA continuum measurement to estimate the dust properties of the host galaxy, assuming that the synchrotron emission at this frequency is minimal.

However, we caution the reader that these measurements should be considered as upper limits given that a non-negligible contribution from the synchrotron emission is possible. Additional measurements covering the 3 GHz to 100 GHz gap are required to better disentangle the synchrotron emission at this frequency (see Chapter 4).

From the $M_{\rm Dust}$ derived in Section 3.6.2 along with the dust parameters T = 47 K and $\beta = 1.6$, we integrate over the SED and obtain infrared luminosity constraints. We calculate the FIR luminosity by integrating over rest-frame 42.5–122.5 μm and get $L_{\rm FIR} = (0.89 \pm 0.10) \times 10^{12}$ $L_\odot$. Integrating over the rest-frame wavelengths 8–1000 μm, we obtain the Total Infrared (TIR) luminosity as $L_{\rm TIR} = (1.26 \pm 0.15) \times 10^{12}$ $L_\odot$. We derive a SFR from the $L_{\rm TIR}$ following the relation in Kennicutt and Evans (2012) scaled to the Chabrier (2003) initial mass function (IMF; this results in a SFR 1.7 times smaller than assuming the Salpeter (1955) IMF), obtaining $\rm SFR_{TIR} = (110.0 \pm 13.0)$ $M_\odot$ $\rm yr^{-1}$. This value is ~ 15% smaller than the resulting from calibrations in Kennicutt (1998). The uncertainty in $\rm SFR_{TIR}$ can be larger because we cannot constrain the dust parameters for temperature T, and emissivity index β (see Figure 3.8).

Using the equations for calculating line luminosities from [C II] measurements presented by Carilli and Walter (2013), we find the areal integrated source brightness temperature $L'_{\rm [C\,II]} = (5.6 \pm 0.9) \times 10^9$ K km $\rm s^{-1}$ $\rm pc^2$. The [C II] line luminosity, which is commonly used to compare luminosities to the underlying continuum, is $L_{\rm [C\,II]} = (1.23 \pm 0.20) \times 10^9$ $L_\odot$. We use the relation in De Looze et al. (2014) to calculate the [C II]-derived SFR:

$$\log \rm SFR_{[C\,II]} = -6.09 + 0.90 \times \log \mathit{L}_{[C\,II]} \tag{3.5}$$

Taking into account the systematic uncertainty in this relation of a factor ~2.3, we find $\rm SFR_{[C\,II]} = (54 - 285)$ $M_\odot$ $\rm yr^{-1}$, which is consistent with the SFR inferred from the TIR luminosity, as indicated in Table 3.4.

3.7.3 *Comparison with the Literature*

Here we place the [C II] and dust emission properties for P352–15 in the context of other quasars at $z \gtrsim 6$ in the literature. In Figure 3.9, we compile the properties of $z \gtrsim 6$ quasars with continuum measurements of S/N> 3 as reported by Decarli et al. 2018; Izumi et al. 2018; Eilers et al. 2020; Eilers et al. 2021b; Venemans et al. 2020. We note that all the literature quasars are radio-quiet with the only exception of J2318–3113, whose [C II] properties have been studied by Decarli et al., 2018 and Venemans et al., 2020, but it was only recently identified as radio-loud (with $R_{4400} \sim 70$) by Ighina et al., 2021. Both radio-loud quasars with [C II] information, P352–15 and J2318–3113, are highlighted in Figure 3.9.

P352–15 has a [C II] line width of 440 ± 80 km $\rm s^{-1}$, which is broader but within one standard deviation than the mean of the distribution from $z \gtrsim 6$ quasars in the literature (350 ± 125 km/s; Decarli et al., 2018; Venemans et al., 2020). The [C II]

Table 3.4: Derived FIR properties for P352–15

$M_{\rm Dust}$ [a]	$(0.36 \pm 0.04) \times 10^8$ $M_\odot$
$L_{\rm FIR}$ [a]	$(0.89 \pm 0.10) \times 10^{12}$ $L_\odot$
$L_{\rm TIR}$ [a]	$(1.26 \pm 0.15) \times 10^{12}$ $L_\odot$
$SFR_{\rm TIR}$ [a]	(110.0 ± 13.0) $M_\odot$ yr^{-1}
$L'_{\rm [C\,II]}$	$(5.6 \pm 0.9) \times 10^9$ K km s^{-1} pc^2
$L_{\rm [C\,II]}$	$(1.23 \pm 0.20) \times 10^9$ $L_\odot$
$SFR_{\rm [C\,II]}$ [b]	$(54 - 285)$ $M_\odot$ yr^{-1}
$L_{\rm [C\,II]}/L_{\rm FIR}$	$(1.38 \pm 0.23) \times 10^{-3}$
$L_{\rm CO(6-5)}$	$< 0.5 \times 10^9$ $L_\odot$

a These values are calculated assuming an MBB matched to the ALMA continuum with $T_{\rm Dust} = 47$ K and $\beta = 1.6$. We caution that these measurements might be affected by synchrotron emission.
b Calculation using the SFR to luminosity relation derived in De Looze et al. (2014).

luminosity we calculate for P352–15 is $(1.23 \pm 0.20) \times 10^9$ $L_\odot$, which is smaller than the median of the distribution but it is still within the typical values of $(1-5) \times 10^9$ $L_\odot$ for quasars at $z \gtrsim 6$ (see Figure 3.9 and e.g., Mazzucchelli et al. 2017b; Venemans et al. 2017a; Novak et al. 2019).

As mentioned in Section 3.8, the dust properties for quasar P352–15 cannot be fully constrained given the strong synchrotron contamination at millimeter wavelengths. However, we see that the upper limit estimate for $L_{\rm FIR} \sim 10^{12}$ $L_\odot$ overlaps with those of quasar host galaxies at $z \gtrsim 6$ in the literature, although it is smaller than the median value of the population (Figure 3.9). Similarly, the SFR implied by the total infrared emission is consistent with the one we derive from the [C II] line, and with previous studies of quasars at these redshifts (e.g., Mazzucchelli et al., 2017b; Eilers et al., 2020; Eilers et al., 2021b).

A widely used diagnostic to study properties of the interstellar medium (ISM) is the [C II]-to-FIR luminosity ratio. Local galaxies ($z < 1$) show a decrease in this ratio towards higher FIR luminosities (referred to as the '[C II] deficit'), driven by the presence of mechanisms provoking dust heating in the ISM (e.g., Malhotra et al., 2001; Farrah et al., 2013; Sargsyan et al., 2014; Díaz-Santos et al., 2017). The high-redshift ($z \gtrsim 6$) sample has a large scatter for this ratio but our calculated $\log(L_{\rm [C\,II]} / L_{\rm FIR}) = -2.86$ is comparable to local ultra-luminous infrared galaxies (ULIRGs), and is consistent with previously found measurements of $z > 6$ quasars (see trend in Figure 3.9, left) (e.g., Venemans et al., 2012; Venemans et al., 2017a; Bañados et al., 2015a; Willott, Bergeron, and Omont, 2015; Mazzucchelli et al., 2017b; Decarli et al., 2018).

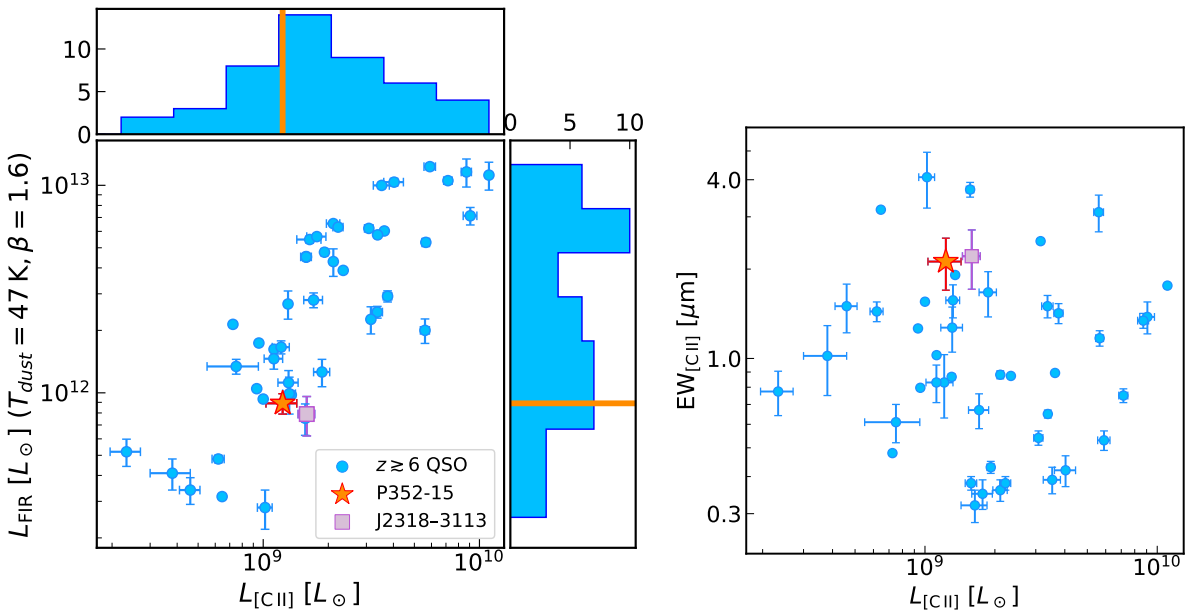

Figure 3.9: *Left:* Relationship between the FIR luminosity (assuming is dominated by cold dust with $T_{Dust} = 47$ K and $\beta = 1.6$), and the [C II] luminosity reported in 45 $z \gtrsim 6$ quasars from Decarli et al. (2018), Izumi et al. (2018), Eilers et al. (2020), Eilers et al. (2021b), and Venemans et al. (2020). The derived properties of P352–15 are within typical values for L_{FIR} and $L_{[CII]}$ in context with the literature. *Right:* Comparison between the [C II] equivalent width and the [C II] luminosity using the same sample of $z \gtrsim 6$ quasars. P352–15's EW$_{[CII]}$ value is at the high end of the distribution found in the literature. The two panels also highlight J2318–3113, the only other radio-loud quasar in the $z \gtrsim 6$ sample with available information for comparison. Both radio-loud quasars have very similar [C II] and FIR properties.

A useful quantity to investigate is the [C II] equivalent width (EW), which has the advantage that it does not depend on the shape of the dust SED:

$$\frac{\mathrm{EW}}{[\mu\mathrm{m}]} = 1000\,\frac{S\Delta v[\mathrm{Jy\ km\ s^{-1}}]}{S_{\nu,0}(\mathrm{cont})[\mathrm{mJy}]}\,\frac{\lambda_0[\mu\mathrm{m}]}{c[\mathrm{km\ s^{-1}}]} \tag{3.6}$$

Here, $S\Delta v$ is the velocity-integrated line, $S_{\nu,0}(\mathrm{cont})$ is the observed continuum flux density at the rest-frame frequency of the line ([C II] in this case), λ_0 is the rest-wavelength which for [C II] is 157.74 µm, and c is the speed of light. Our computed value for P352–15 is EW$_{[CII]} = 2.12 \pm 0.42$ µm, placing P352–15's EW$_{[CII]}$ at the high end of the distribution but with several other hosts of radio-quiet quasars having comparable or larger EW$_{[CII]}$ (see right panel in Figure 3.9). We conclude that the EW$_{[CII]}$ of P352–15 is consistent with what is expected from the properties of radio-quiet quasars, and it is, therefore, likely that the continuum underlying the [C II] emission is indeed not strongly influenced by the radio emission (see §3.7.1).

It is worth noting that the only two $z \gtrsim 6$ radio-loud quasars studied in their rest-frame FIR and [C II] properties lie in a very similar position in the parameter space of Figure 3.9. Nevertheless, a systematic mm study of a larger sample of radio quasars

at high redshifts is necessary to be able to make statistical comparisons between the black hole/host galaxy properties of radio-loud and radio-quiet sources.

3.8 SUPPLEMENTARY OBSERVATIONS OF P352–15

This radio-loud quasar was investigated in X-ray observations by Connor et al. (2021) to look for counterpart evidence of the radio jet observed in Momjian et al. (2018). That work does not find excess of X-ray emission from the source in comparison to other radio-loud quasars. However, they find a tentative detection of X-ray emission along the jet axis of P352–15 at 50 kpc from the central AGN. This could potentially be the signature of a more elongated jet. The 3σ detection is ruled out as a background fluctuation and is measured to have a $L_{2-10} \sim 10^{44}$ erg s^{-1}.

We consider this reported detection of extended X-ray emission and looked for a radio counterpart in our ALMA and NOEMA data described in this Chapter. We cannot identify a source in either of our observations at this position and report 3-sigma limits of < 0.11 mJy (ALMA, 290 GHz) and < 0.04 mJy (NOEMA, 100 GHz). This non-detection could be explained by the source being too faint at these frequencies, or due to being unresolved in these mm observations. Alternatively, the non-detection is indicative of Inverse Compton (IC) interactions of jetted particles with the cosmic microwave background (Connor et al., 2021). If confirmed, this would become the most distant quasar jet observed in X-ray energies.

P352–15 has extreme radio properties and therefore warrants further investigation to connect the black hole activity with the quasar host galaxy. Deeper and higher resolution radio and millimeter follow-up are needed to further investigate this X-ray source.

3.9 SUMMARY AND CONCLUSIONS

In this Chapter we presented the analysis of millimeter and radio observations of the powerful radio bright quasar P352–15. Our major findings are summarized as follows.

- The ALMA observations of the [C II] line emission from this quasar resulted in a systemic redshift calculation of $z = 5.832 \pm 0.001$. We find a [C II] line width of 440 ± 80 km s^{-1}. The [C II] luminosity is 1.23×10^9 L$_\odot$, comparable to values reported in other high-redshift quasars in the literature. The derived star formation rate from the [C II] emission is $SFR_{[C\,II]} = (54 - 285)$ M$_\odot$ yr^{-1}. Finally, the ALMA observations revealed an underlying unresolved continuum source at 290 GHz with a flux density of 0.34 ± 0.04 mJy (see Figures 3.5–3.3).

- We do not detect the CO (6–5) emission line in our NOEMA 100 GHz observation. The derived 3σ upper limit is <0.35 mJy corresponding to a luminosity $L_{CO(6-5)} < 0.5 \times 10^9$ L$_\odot$ (assuming the same FWHM as measured for the [C II]

line). Continuum emission is detected with NOEMA at 100 GHz with a flux density of 0.10 ± 0.01 mJy (see Figure 3.3).

- The high S/N GMRT 215 MHz observations of the quasar allow us to improve the constraints on the radio emission at low frequencies (c.f., Bañados et al. 2018a). The synchrotron radiation can be well modeled by a simple power-law with spectral index $\alpha_3^{0.215} = -0.88 \pm 0.08$. This resulted in updating the calculation of the quasar's radio-loudness parameter $R_{4400} = 1100 \pm 280$ and $R_{2500} = 1470^{+110}_{-100}$, confirming its prominent radio power (see Figure 3.8).

- We study the dust emission of the quasar host galaxy by using the typical approach of modeling a modified black body function (MBB) to our two mm-continuum measurements from ALMA 290 GHz and NOEMA 100 GHz. However, the NOEMA measurement is an order of magnitude brighter than expected from the MBB scaled to the ALMA emission using the typical $T_{dust} = 47$ K and $\beta = 1.6$, and cannot be modeled by any other dust parameters commonly used in the literature. Therefore we hypothesize that the 100 GHz continuum emission is dominated by synchrotron radiation. However, the emission is three times dimmer than the expected emission by extrapolating the trend at lower frequencies. This implies a break in the synchrotron spectrum (see Figure 3.8).

- From the ALMA 290 GHz continuum observations we derive the FIR properties of the quasar, assuming this data point is not significantly contaminated by synchrotron emission (see discussion in Section 3.7.1). Assuming a MBB with typical parameters ($T_{dust} = 47$ K and $\beta = 1.6$), we derive a dust mass and FIR and TIR luminosities. These quantities are reported in Table 3.4. The star formation rate derived from the L_{TIR} is $SFR_{TIR} = (110.0 \pm 13.0)\ M_\odot\ yr^{-1}$, which is consistent with the calculated SFR from the [C II] emission.

- This quasar lies within typical estimates of [C II] FWHM, $EW_{[C\,II]}$, $L_{[C\,II]}$, and L_{FIR} compared to quasars at $z \gtrsim 6$ in the literature. We highlight that the derived properties of P352–15 are very similar to quasar J2318–3113, which was the only other radio-loud quasar with [C II] and rest-frame FIR studies (see Figure 3.9). A more comprehensive study of high-redshift radio quasars in the millimeter is required for statistical comparisons (see Khusanova et al., 2022).

- We investigate the mm counterpart of an X-ray source detected in Connor et al. (2021) at 50 kpc from the black hole's X-ray emission and at the same angle as the 1.6 kpc jet already evidenced in Momjian et al. (2018). We report 3σ upper limits from ALMA at < 0.11 mJy, and from NOEMA at < 0.04 mJy.

This quasar presents an intriguing SED (Figure 3.8) and leaves more open questions that make it an excellent target for follow-up observations. For example, to evaluate the turnover frequency of the synchrotron spectrum. This is further investigated in the following Chapter 4 with VLA observations filling the gap between 3

and 100 GHz. Finally, our current data marginally resolves the [C II] emission (Figure 3.5); higher resolution observations could reveal potential signatures of on-going merger or outflow in this quasar. This could be addressed with future observations from ALMA or NOEMA at higher resolution and S/N.

4

BLACK HOLE ACCRETION AND JET LAUNCH TIMESCALES OF QUASAR P352-15

In the previous Chapter 3 we saw evidence for the extreme radio brightness of the quasar P352–15 and the strong synchrotron emission even in the mm-domain where usually cold dust dominates. In the following Chapter, we investigate in more detail the effects of the powerful radio jets on the ISM producing a spectral steepening in the synchrotron emission. We estimate a timescale corresponding to the jet age from this steepening and compare it to the timescale from the ionizing UV emission of the last black hole accretion event. We provide background on jet physics when it interacts with the ISM in §4.1. Then, we describe the VLA observations designed to locate the frequency of the synchrotron break from P352–15 in §4.2, and their data reduction in §4.3. The Very Large Telescope (VLT)-XShooter spectral observations of P352–15 necessary to measure the quasar lifetime, or its last accretion event, are described in §4.4 along with the reduction method. A combined fit to the mm-observations of the cold dust emission of P352–15 from the previous Chapter 3, and radio VLA observations with synchrotron break are modeled in §4.5. The calculation of the dynamical age of the jet is explained in §4.6. We estimate the proximity zone of P352–15 as described in §4.7 and the corresponding quasar lifetime measurement in §4.8. We compare the jet and quasar lifetime timescales and discuss caveats in our measurement and outlook for future observations repeating this experiment in §4.9.

This work is being prepared to be submitted for publication. I was PI of the VLA telescope proposal which obtained the necessary observations to find a spectral break in the synchrotron spectrum of the jet in P352–15. Collaborator Emmanuel Momjian and I worked on the VLA data reduction. I led the analysis of the spectral aging from the jet. The calculation and interpretation of the jet's dynamical age was done in collaboration with Bhargav Vaidya, Emmanuel Momjian and Eduardo Bañados. Collaborators Zhang-Liang Xie, Christina Eilers and I worked on the data reduction of the VLT-XShooter spectral data of P352–15. Christina Eilers, Frederick Davies, Sarah Bosman and I have worked on the calculation of the proximity zone and *quasar lifetime*, as well as the interpretation of the spectral features in the rest-UV spectrum of this quasar. I have led the write-up of this work and the discussion of the results. Additional colleagues collaborated on the VLA proposal and fruitful discussion throughout the development of this work.

4.1 BACKGROUND ON JETS AND ISM INTERACTIONS

Powerful radio-jets from AGN at low redshifts ($z \sim 0.05$) and their effect on the ISM has been investigated in a variety of scenarios (e.g., Carilli et al., 1991; Laing et al., 2008; Mahatma et al., 2020). When jets collide with the ISM, the created shock wave is subjective to magneto-hydrodynamic instabilities that are reflected on the synchrotron and X-ray emission of the AGN, or quasar (e.g., Borse et al., 2021). These instabilities change the jet dynamics such that after the jet goes through a dense patch of the ISM, the injection of electrons is not organized in a collimated structure anymore but a turbulent flow from small-scales (Kolmogorov characteristics) (e.g., Laing et al., 2008). Consequently, the relativistic electrons in the jet are no longer cooling normally following the power-law relationship $S_\nu \propto \nu^\alpha$, where S_ν is the observed flux density at the frequency ν and α is the radio spectral index. Instead, the electrons in the jet are re-accelerated to high energies (Lorentz factor of $\gtrsim 10^5$; Bell, 1978) after the jet-ISM shock occurs and then cool again following the power-law signature. However, the power law signature past the dense ISM suffers from a reduction of traveling relativistic electrons. This depletion is more evident at the highest frequencies given that the electron loss time-scale is inversely proportional to its energy and hence higher energy electrons radiate away their energy faster (Kellermann et al., 1989). This effect is reflected as a break in the power law of the synchrotron emission at high frequencies. Multiple studies have modeled this effect by varying the injection of electrons and resulting spectral index α after the jet-ISM shock (e.g., Kardashev, 1962; Pacholczyk, 1970; Jaffe and Perola, 1973; Myers and Spangler, 1985; Heavens and Meisenheimer, 1987; Meisenheimer et al., 1989; Tisanić et al., 2019; Tisanić et al., 2020). The frequency break $\nu_{\rm obs}^{\rm break}$ above which the spectrum steepens from the injected power law, relates to the *spectral aging*, or $t_{\rm spec}$. This timescale is defined as the time since the spectrum was a power law out to infinite frequency. Thus, one can relate the spectral aging of the time since the shock process began, to the time since the jet launched, or the *dynamical age* $t_{\rm dyn}$. Observationally, however, this phenomenon is yet to be demonstrated and quantified in sources at $z \gtrsim 6$. P352–15 is the first laboratory at these redshifts where we attempt to do these measurements. In the beginning of this Chapter we investigate the synchrotron break $\nu_{\rm obs}^{\rm break}$ to calculate the $t_{\rm spec}$ and $t_{\rm dyn}$ of the jet based on multi-frequency VLA observations.

4.2 VLA OBSERVATIONS

The VLA observations were performed under program 21A-307 (PI: Rojas-Ruiz). Observations were taken in the L (1.5 GHz), S (3 GHz), C (6 GHz), X (10 GHz), U (15 GHz), K (22 GHz), A (33 GHz), and Q (45 GHz) bands to construct the radio SED of P352–15 and determine the exact location of a break or a turnover in the synchrotron emission. This setup covers the observational gap between 3 GHz and 100 GHz previously observed in Rojas-Ruiz et al. (2021).

We designed our observations by assuming a break near 3 GHz (the most conservative case) and aiming to detect the expected emission with a signal-to-noise S/N$>$ 15.

This S/N also allows to determine an intra-slope for each receiver band, which is important to have an accurate location of the turnover frequency. Since we know that the emission of our source comes from a region smaller than $0\farcs5$ and there are no other strong radio sources in the field, we used the compact C and D configuration. The resolution provided with this configuration improved the existing radio data of this field (e.g., NVSS 1.4 GHz and VLA DDT 3 GHz). We thus repeated observations in these bands for only 5 min on-source each, to avoid any possible misinterpretation due to intrinsic quasar variability. The total allocated time was 5 hours, of which 1 hour and 52 minutes were on source (See Table 4.1. The observations were taken in four parts:

- The first set of observations was performed in the L, S, C, and X bands. L and S-band observations were taken with the 8-bit sampler offering a total ~ 2 GHz bandwidth, per recommendation from the National Radio Astronomy Observatory (NRAO)[1]. The C and X-band observations were taken with the 3-bit sampler totaling a $\sim$ 8 GHz bandwidth per band. The observations were performed by observing the Flux calibrator in all bands first, and then given instrumental setup and maximize the allocated time, two iterations of the cycle L S C X Gain calibrator – Target – Gain Calibrator. Observations were carried out on March 26^{th}, 2021 with 27 antennas in D configuration. For all bands, data was partially or fully lost in three antennas; L-band data was partially or fully gone in one additional antenna. This loss of antennas did not have a large impact on the final product.

- The next set of observations were taken in the U and K bands using the 3-bit sampler. The Flux calibrator was observed first and then two iterations of the cycle U K Gain calibrator – Target – Gain Calibrator. Observations were carried out on June 11^{th}, 2021 with 27 antennas in C configuration. Data was partially or fully lost in only two antennas.

- Observations in the A and Q bands in 3-bit sampler mode were performed. The Flux calibrator was observed in each band first, then the Gain calibrator – Target – Gain Calibrator observations in the A-band were performed in two iterations, while in the Q-band observations were taken in two iterations of five cycles (i.e. 10 cycles of Gain calibrator – Target – Gain Calibrator). These observations will be called Q1. Data was taken on August 17^{th}, 2021 in C-configuration with 27 antennas. Data was fully lost in three antennas, and for the A-band data were additionally lost in another antenna. These antenna losses did not affect the final reduced images.

- To complete the sensitivity in the Q-band while avoiding overheads from time constrictions, more Q-band observations were carried out separately (called Q2 from now). Two iterations were taken, one of six cycles and the other of seven cycles of Gain calibrator – Target – Gain Calibrator. These data were

1 https://science.nrao.edu/facilities/vla/docs/manuals/oss/performance/vla-samplers

Table 4.1: Summary of VLA Observations of P352–15

Band	Flux Cal.	Gain Cal.	Total time on Target
L	3C147	J2348–1631	00:05:36
S	3C147	J2348–1631	00:05:26
C	3C147	J2331–1556	00:05:25
X	3C147	J2331–1556	00:05:25
U	3C147	J2331–1556	00:05:57
K	3C147	J2331–1556	00:06:30
A	3C147	J2331–1556	00:06:27
Q1	3C147	J2331–1556	00:31:00
Q2	3C147	J2331–1556	00:40:18

observed on July 31st, 2021 in C-configuration with 27 antennas, no problems with antennas were reported.

4.3 VLA DATA REDUCTION

All the data was initially processed with the VLA Calibration Pipeline v2020.1.0.36, using the Common Astronomy Software Applications package (CASA, v6.1.2., McMullin et al., 2007). Further calibrations, cleaning, and imaging of the data were performed with the CASA version 6.1.2–27. We excluded the channels that were significantly affected by radio frequency interference (RFI)[2] , which is more characteristic at certain frequency ranges of the L, S, C, and X bands. The flux density scale calibration accuracy is about 3%, from using 3C147 as flux calibrator for all the observations. For all bands, the data was self-calibrated in order to correct visibility amplitude errors from extensive artifacts from background sources, particularly in the lowest-frequency bands L, S, C, X, or phase errors.

The L-band was cleaned using a Hogbom cycle algorithm, and Briggs weighting with a robust factor of 0.4 was used to image the continuum emission. The S-band was cleaned with the deconvolver 'mtmfs' and 2 terms of Taylor coefficients for the spectral model. Imaging was performed with Briggs weighting and a robust of 0.4. Additionally, we divided the S-band data into two chunks of sub-bands (see central frequencies in Table 4.2). The C-band was divided into 4 sub-bands, each imaging was produced using the 'mtmfs' algorithm and Briggs weighting with a 0.8 robust factor. The process of re-calibrating and imaging was the same for the X-band but in this case, the last sub-band was dominated by RFI and thus was discarded. See these reduced images in Figure 4.1.

2 https://science.nrao.edu/facilities/vla/docs/manuals/obsguide/rfi#section-3

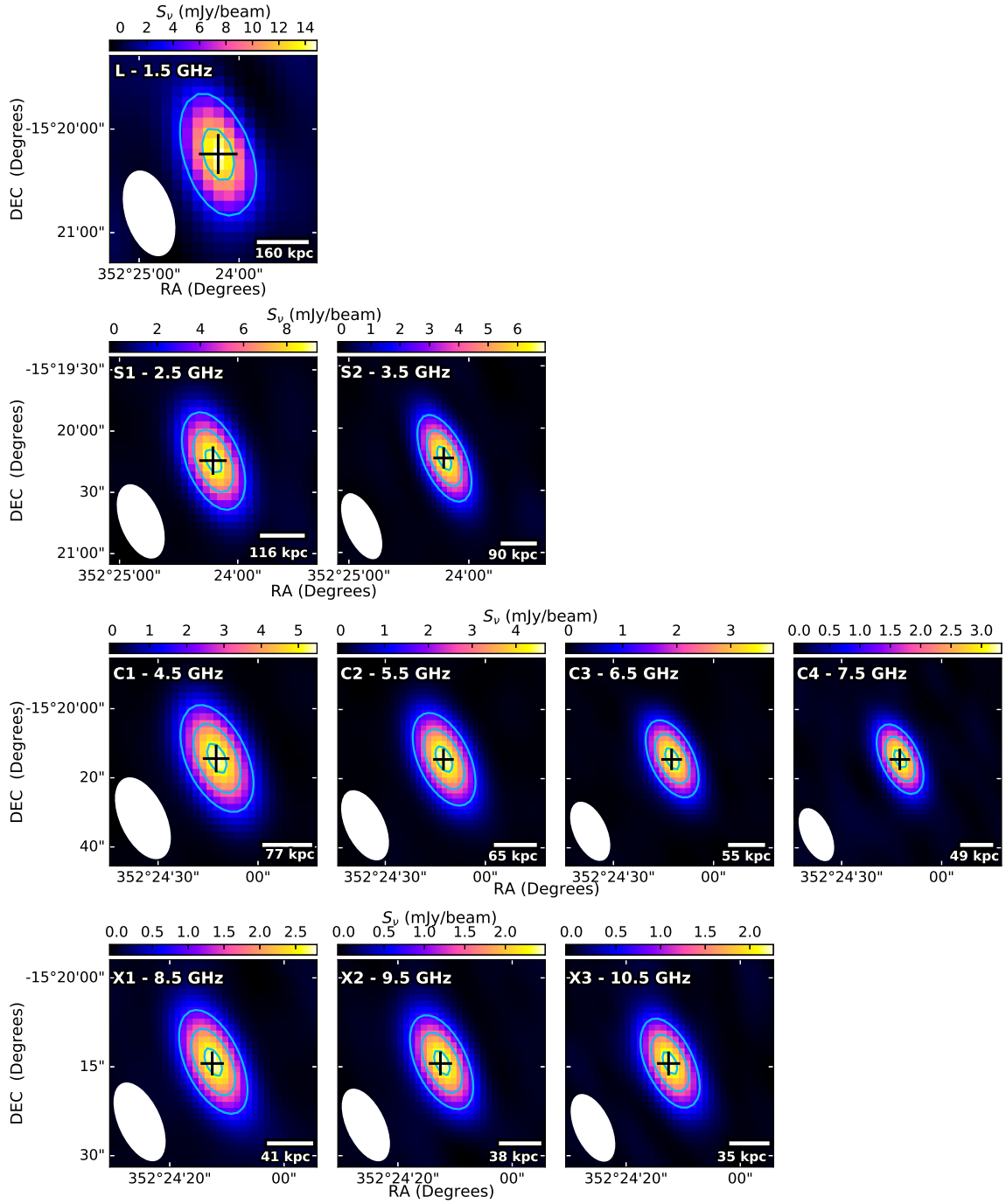

Figure 4.1: Reduced images from the L-band and SCX sub-bands. In all stamps, the color map indicates the flux density S_ν of the synchrotron emission. The central cross represents the optical position of P352–15 as seen in Momjian et al. (2018). At the top of each stamp is the central frequency of the band and sub-bands. The beam size is at the bottom left corner. Note that for visualization purposes, each set of sub-bands has been zoomed in (see the physical scale at the bottom right). The contours are set as follows: L-band ($\pm1\sigma, \pm3\sigma$), SCX sub-bands ($\pm6\sigma, \pm12\sigma, \pm18\sigma$). Refer to Table 4.2 for the corresponding errors σ and S/N of each sub-band.

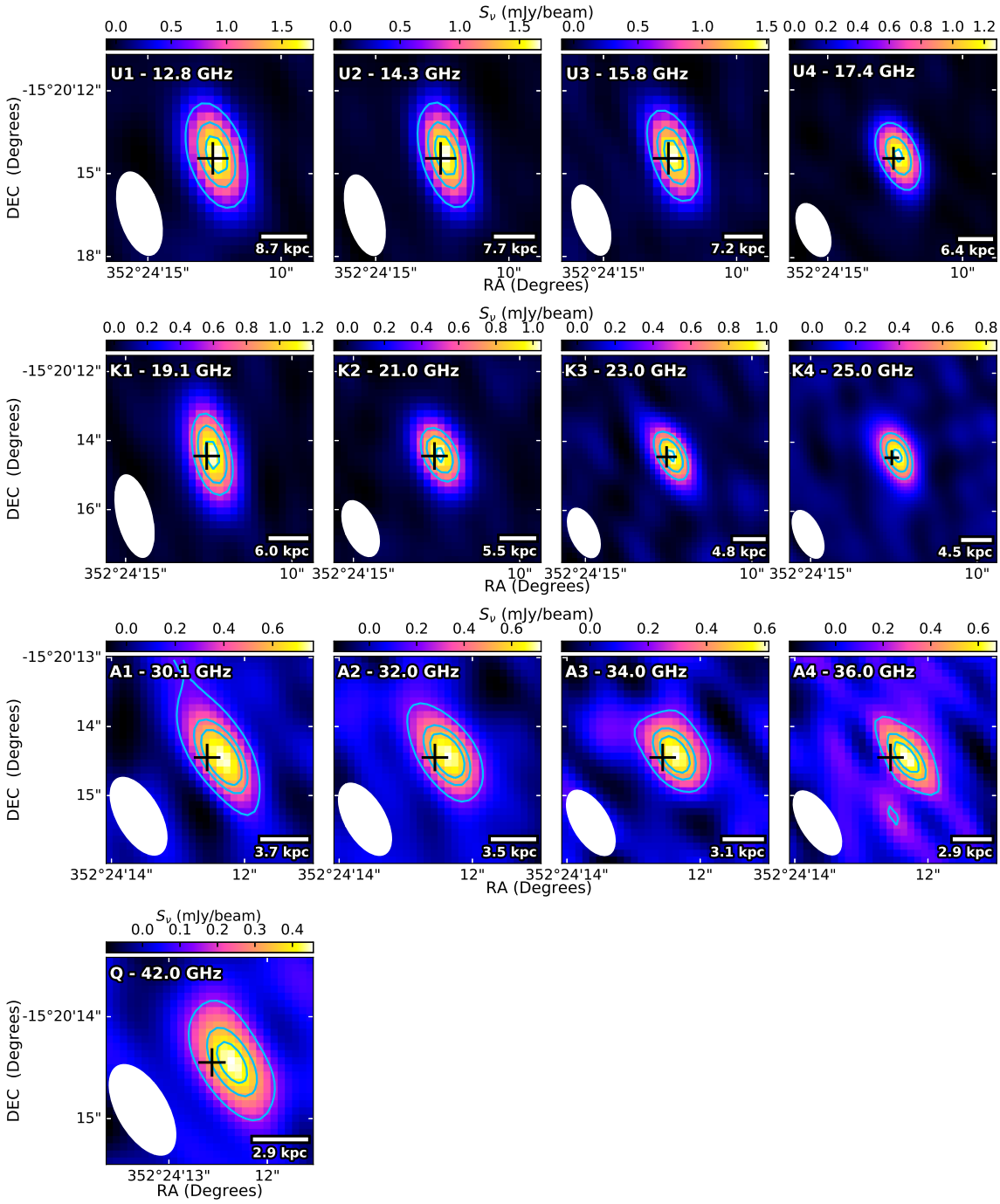

Figure 4.2: Similar to Figure 4.1 but for the U, K, A, and Q images. The contours are set as follows: U-band ($\pm6\sigma, \pm12\sigma, \pm18\sigma$), K-band ($\pm5\sigma, \pm7\sigma, \pm9\sigma$), A-band ($\pm2\sigma, \pm4\sigma, \pm6\sigma$), and Q-band ($\pm2\sigma, \pm4\sigma, \pm5\sigma$).

Table 4.2: VLA Flux Measurements of P352–15

Band	$\nu_{cent.}$ (GHz)	S_ν (mJy beam^{-1})	δS_ν (mJy beam^{-1})	S/N	Beam (″)
L	1.5	14.89	3.80	3.9	51.27×27.63
S1	2.5	9.41	0.48	20	38.45×19.95
S2	3.5	6.93	0.35	20	34.08×15.51
C1	4.5	5.52	0.28	20	25.44×13.25
C2	5.5	4.67	0.23	20	21.84×11.26
C3	6.5	3.78	0.19	20	18.39×9.53
C4	7.5	3.32	0.17	20	16.47×8.38
X1	8.5	2.80	0.14	20	14.27×7.11
X2	9.5	2.51	0.13	20	13.22×6.48
X3	10.5	2.25	0.12	19	12.25×6.11
U1	12.8	1.78	0.10	19	3.16×1.51
U2	14.3	1.67	0.09	19	3.05×1.34
U3	15.8	1.52	0.08	19	2.69×1.24
U4	17.4	1.37	0.06	18	2.05×1.11
K1	19.1	1.19	0.12	9.7	2.49×1.04
K2	21.0	1.05	0.11	9.6	1.76×0.94
K3	23.0	1.02	0.11	9.4	1.56×0.83
K4	25.0	0.84	0.09	9.4	1.53×0.77
A1	30.1	0.76	0.11	6.8	1.27×0.64
A2	32.0	0.72	0.11	6.6	1.18×0.60
A3	34.0	0.61	0.10	6.2	1.08×0.54
A4	36.0	0.65	0.11	5.7	1.07×0.51
Q2	42.0	0.46	0.08	5.8	1.00×0.50

The U, K, and A bands had minimal RFI contamination, and four sub-bands per ban observations were imaged with the 'mtmfs' algorithm and Briggs weighting with a robust factor of 0.8. The Q1-band data observed with the A-band presented an abnormal increase in flux density in the last two sub-bands at higher frequencies, which was not observed in the A-band data. The phase calibrator J2331–1556 was imaged but no anomalies were identified. This phenomenon was not observed in Q2, in which the data indeed followed the characteristic power law of synchrotron emission. Therefore, Q1 data was discarded and the final imaging from the Q-band is from the Q2 observations, which have longer exposure time as well. Given the lower S/N in this band, the data was not divided into sub-bands in order to maintain the highest sensitivity of the synchrotron emission at this frequency bandwidth. The final images from U, K, A, and Q are presented in Figure 4.2

We note that the choice of imaging sub-bands instead of a cube per band, where possible, resulted in an improved S/N and thus more accurate measurements for our fit to the synchrotron emission and its steepening. For all images, the flux density was found by fitting a 2D Gaussian in `casaviewer`, and the rms error was measured from the image rather than the fit of the Gaussian in order to account for all noise variations around the source. Following Shao et al. 2022, we additionally considered a calibration error of 5% for bands L through U, 10% for the K-band, 12.5% for the A-band, and 15% for the Q-band. The flux and beam measurements in all bands are reported in Table 4.2.

4.4 VLT-XSHOOTER SPECTRAL OBSERVATIONS AND DATA REDUCTION

Here we describe the observations necessary to measure the proximity zone R_p for quasar P352–15, to later calculate the *quasar lifetime* t_Q following the methodology in Eilers et al., 2017.

Rest-UV/Optical spectral data of P352–15 was taken with VLT/XShooter as part of program ID = 0102.A-0931 (PI: B. Venemans). XShooter works as a multi-wavelength, medium-resolution spectrograph mounted at the VLT UT2 telescope. It consists of three spectroscopic arms observing in the UVB spectrum (300–559.5) nm, VIS (559.5–1024) nm, and NIR (1024–2480) nm. Given the Gunn-Peterson trough effect, we only obtain spectral information from quasar P352–15 at $z = 5.832$ in the VIS and NIR arms. This data was taken on October 3^{rd} and 11^{th}, 2018. For the NIR observations, nodding along the slit in an ABAB pattern was used for taking offset exposures, which is later used as a double pass sky subtraction.

The data reduction is performed with `PyPeIt`[3](Prochaska et al., 2020), a package developed specifically for the reduction of spectral data and supporting various instruments around the globe, including XShooter. The VIS and NIR data are similarly reduced with standard techniques. The two sets of science frames from both dates of observations are used conjunctively during the reduction process. The first calibra-

3 https://pypeit.readthedocs.io/en/release

tions involve sky subtraction on the 2D images (including the difference imaging of dithered AB pairs of exposures for the NIR arm case) and applying a 2D b-spline fitting procedure. Object traces from the 2D images are identified and extracted to produce the 1D spectra following the optimal spectrum extraction technique from Horne (1986). Next, the 1D spectra for VIS and NIR are flux calibrated using the GD71 star. The resulting fluxed 1D spectra are coadded and corrected for telluric absorption. This last correction is performed using the `PypeIt`-provided telluric file from Paranal Observatory[4], which identifies the wavelength ranges of the tellurics, and applying telluric model grids produced from the Line-By-Line Radiative Transfer Model (LBLRTM[5]; Clough et al., 2005; Gullikson, Dodson-Robinson, and Kraus, 2014). The telluric features are then masked to later join the VIS and NIR final spectrum of P352–15, as presented in Figure 4.4.

4.5 FINDING THE FREQUENCY BREAK OF THE SYNCHROTRON EMISSION

Previous studies in Rojas-Ruiz et al. (2021) on the mm and radio SED of P352–15 showed evidence for a synchrotron break in the power law spectrum. This was concluded given that synchrotron radiation was contaminating the observations of cold dust at 100 GHz, supporting the jet-ISM interaction scenario. In order to correctly model the synchrotron spectral break ν_{obs}^{break} of P352–15, we must combine the models for the cold dust with available observations, and synchrotron emission with the new VLA data.

4.5.1 *Modeling the Cold Dust from mm Observations*

We use the mm observations from Rojas-Ruiz et al. (2021) at 290 GHz and 100 GHz to model the cold dust with a MBB of the form:

$$S_{obs} = f_{CMB}\ [1+z]\ D_L^{-2}\ \kappa_{\nu_{rest}}(\beta) \times M_{Dust}\ B_{\nu_{rest}}(T_{Dust,z}), \tag{4.1}$$

where f_{CMB} is a correction against the CMB contrast, D_L is the luminosity distance, $\kappa_{\nu,rest}(\beta)$ is the dust mass opacity, which depends on the dust emissivity spectral index β, and M_{Dust} is the dust mass. All values are given in SI units. See Rojas-Ruiz et al. (2021) for more details on the different components of this equation.

We use the calculated dust mass of the host galaxy of P352–15 in Rojas-Ruiz et al. (2021) where $M_{Dust} = (0.36 \pm 0.04) \times 10^8\ M_\odot$. Previously, Rojas-Ruiz et al. (2021) presented a range of acceptable values for the dust temperature $T = 30 - 100$ K and emissivity index $\beta = 1.6, 1.95$ given that the lack of information in the mm and radio SED prevented accurate calculations due to overfitting. On this occasion, however, given the rich VLA supplementing data, we leave T and β as free dust parameters to fit a joint MBB and synchrotron break model.

4 https://pypeit.readthedocs.io/en/release/telluric.html
5 http://rtweb.aer.com/lblrtm.html

4.5.2 *Modeling the Synchrotron Spectral Break*

The intrinsic synchrotron emission is well-described by the power law relationship between the flux density and spectral index $S_\nu \propto \nu^\alpha$. A break in the power law at high frequencies has been well characterized in the past using observations and theoretical background on jet physics and particle distribution and energy loss. The models we use to fit the break of the synchrotron spectrum are described as follows:

- The continuous injection model (abbreviated as CI) initially described theoretically in Heavens and Meisenheimer (1987) and then applied to observations of hot spots (where the jet interacts with the ISM) in Meisenheimer et al. (1989). This model involves a constant injection rate of relativistic electrons in the power law distribution. This case simulates an observed unresolved source where different populations of electrons are seen at once. This is the case of our VLA observations of P352–15. Above the frequency break $\nu_{\rm obs}^{\rm break}$, the steepened spectrum has a one-half steeper index $\alpha_{\rm steep}$ from the injected power law spectrum $\alpha_{\rm in}$ such that $\alpha_{\rm steep} = \alpha_{\rm in} - 0.5$.

- The Kardashev-Pacholczyk (KP) model described in Kardashev (1962) and Pacholczyk (1970) assumes a "one-shot" injection of relativistic electrons into the power law distribution. The particles will maintain their initial pitch angle with respect to the magnetic field over time i.e., no scattering. After the frequency break $\nu_{\rm obs}^{\rm break}$, the new power law depends on the injected spectral index in the following relationship $\alpha_{\rm steep} = (\frac{4}{3})\alpha_{\rm in} - 1$.

- The Jaffe-Perola (JP) model (Jaffe and Perola, 1973) also incorporates a "one-shot" injection of electrons but allows for scattering of the pitch angle with time. This timescale is still smaller than the radiative lifetime of the particles and thus results in a sharp exponential cutoff to the power law distribution of particles. In order to observe this effect in P352–15, additional observations closer to the NOEMA 100 GHz dust+synchrotron observation would be necessary to model the exponential cutoff. However, we have a gap between the VLA Q-band at 42 GHz and the NOEMA 100 GHz observations. Therefore, we do not include the JP model in the analysis of this work.

- Finally, one could in principle make a "free model" as in the case of Tisanić et al. (2019) and Tisanić et al. (2020) to fitting a totally free double-power-law, i.e. without constraints on the steepened power law $\alpha_{\rm steep}$. When we applied this free model to our data, the quality of the fit was not optimal, although the resulting spectral aging $t_{\rm spec}$ measurement was consistent within 1σ of the mean spectral aging using the well-studied CI and KP models that account for jet physics (see more on the spectral aging estimates in §4.6).

In Figure 4.3 we show the mm and radio observations of P352–15 fitted with a joint function of a MBB model and a synchrotron steepening assuming the CI modeling (*top*) and KP model (*bottom*). The parameters to fit with this function are the dust

temperature (T) and emissivity index (β), the spectral index of the injected power law (α_{in}), a constant (γ) relating the power law proportionality $S_\nu = \gamma \times \nu^\alpha$, and the frequency break (ν_{obs}^{break}). We find that assuming the CI model $\nu_{obs}^{break} = 18.32 \pm 1.8\,GHz$, and for the KP model $\nu_{obs}^{break} = 39.19 \pm 4.6\,GHz$.

4.6 CALCULATING THE JET TIMESCALE

The evolution of the relativistic particles in jets and hot spots where there is interaction with the ISM has been thoroughly studied. Leahy 1991 relates the radiative aging of electrons to the spectral aging t_{spec} following the equation:

$$t_{spec} = 50.3 \frac{B^{1/2}}{B^2 + B_{CMB}^2} ((1+z)\nu_b)^{-1/2} \ [Myr] \tag{4.2}$$

where B in units of (nT) is the magnetic field of the jet. B_{CMB}(nT) is the magnetic field of the CMB at the redshift z of the object, and ν_b (GHz) is the frequency break we calculated but in the rest-frame. The magnetic field strength B for P352–15 was previously calculated from VLBA observations ($B \sim 3.5\,mG$ Momjian et al., 2018). Adopting the calculated B and the frequency breaks found in the previous section, we find that $t_{spec} = 685 \pm 35$ yrs, and $t_{spec} = 469 \pm 27$ yrs assuming the CI and KP models of the power law break, respectively. Note that the quoted uncertainties are only statistical, and do not reflect the larger systematic uncertainty in the magnetic field strength.

Measuring this radiative aging of electrons does not necessarily represent the timescale of the jet since its launch, which is defined as the dynamical age t_{dyn}. Discrepancies between t_{spec} and t_{dyn} may arise from the changing strength of the magnetic field as the electrons dissipate along the jet, and other environmental effects involving the ISM and jet hot spots (see more with references within Rudnick, Katz-Stone, and Anderson, 1994; Jones, Ryu, and Engel, 1999). In fact, t_{spec} is found to be consistently shorter than t_{dyn} given the methodology used to calculate the spectral aging relies more heavily on the magnetic field variation rather than the instrinsic synchrotron aging (e.g., Kaiser, 2000; Machalski, Jamrozy, and Saikia, 2009). Several approaches have been introduced to compensate for the uncertainty in calculating the dynamical age from the spectral aging. For example, algorithms that account for different properties of the jet including the kinetic energy input into the jet from the AGN, synchrotron emission in different areas of the jet, shocks with the ISM, among others (e.g., Machalski, Jamrozy, and Saikia, 2009, and reference within). However, Blundell and Rawlings (2000) studied the differences among the two timescales and concluded that if the $t_{spec} \ll 10^7$ yrs, then one can use the spectral aging t_{spec} to approximate the measurement of the dynamical age t_{dyn}. This can be achieved by evaluating on the observed frame the cooling time of the electron with Lorentz factor γ_e that is in the fluid frame. To make this conversion one must know the Bulk Lorentz factor of the jet Γ_{jet} that is calculated from the observed relativistic boosting.

Then, the dynamical age can be calculated following the equation:

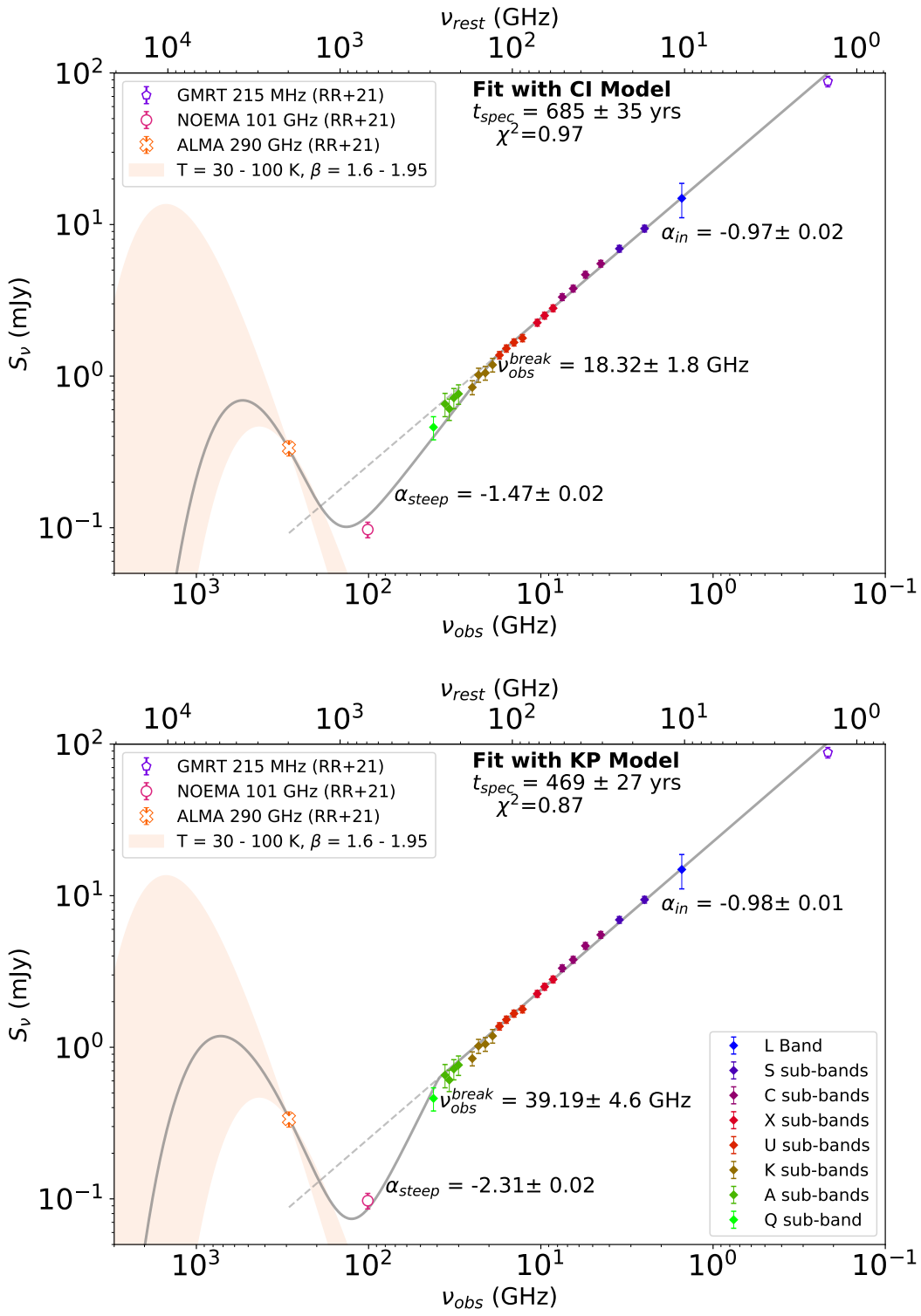

Figure 4.3: The SED of P352–15 in the mm and radio synchrotron emission. The mm-observations presented here are from Rojas-Ruiz et al. (2021), and the radio observations are from this work in all the sub-bands of the VLA from 1.5 GHz - 45 GHz. *Top:* Combined fit the cold dust with a MBB model and synchrotron break model considering a continuous injection (CI) of electrons after the jet shocks with the ISM. *Bottom:* Similar to above but considering a "one-shot" injection of electrons from the KP model. We note that both fits are consistent with our observations, the difference relies on the assumption of relativistic electron distribution. The resulting spectral aging of the jet t_{spec} from both models falls within the same order of magnitude and for the rest of this work we consider both values as upper and lower estimates, correspondingly.

$$t_{dyn}(\nu_{obs}) = \frac{3}{4\sigma_T (U_B + U_{CMB})} \left(\frac{m_e c e B}{2\pi\Gamma_{jet}}\right)^{1/2} \nu_{obs}^{-1/2}(1+z)^{1/2} \text{ [kyr]} \quad (4.3)$$

In this equation, σ_T is the Thompson cross section in cgs units, U_B is the magnetic energy density and U_{CMB} is the CMB energy density at the redshift z of the source (both in cgs units). The electron mass m_e, and the speed of light c are in cgs units. e is the electron charge in elctrostatic units (ESU) units, B is the magnetic field of the jet in Gauss, Γ_{jet} is the Lorentz factor of the jet, ν_{obs} is the observed frequency break in Hz.

For the case of P352–15, $t_{spec} \sim 10^3 \ll 10^7$ yrs so we can use Equation 4.3 to calculate the dynamical age of the jet. In Momjian et al. (2018) observations of the jet hot spots and their direction with respect to the optical position of the AGN suggest we are seeing one of the jets that extends up to $d_{jet} \approx 1.6$ kpc. This suggests that the viewing angle of the jet of P352–15 has a boosting with $\Gamma_{jet} \sim 2$. $\Gamma_{jet} = 1$ would correspond to a classical Fanaroff-Riley Class II (FRII) source where the jets are perpendicular to our line-of-sight. We calculate the jet Lorentz factor Γ_{jet} by approximating the jet timescale to the spectral aging we calculated above and follow the equation:

$$\Gamma_{jet} = [1 - (v/c)^2]^{-1/2}, \qquad \text{where } v \sim d_{jet}/t_{spec} \quad (4.4)$$

We use the average of the spectral aging found from the joint fits with CI and KP models that $t_{spec} \sim 577$ yrs. Thus we find a $\Gamma_{jet} = 2.35$, consistent with the expectation from the jet angle observations in Momjian et al. (2018).

Finally, we apply Equation 4.3 with $\Gamma_{jet} = 2.35$, the magnetic field of the jet $B \sim 3.5$ mG, and the average frequency break from the CI and KP model fits $\nu_{obs} = 28.76$ GHz. The resulting dynamical age of P352–15 is as young as $t_{dyn} \sim 2,000$ yrs. We note that this is the best approximation we can report given the large uncertainty in the magnetic field of the jet. This magnetic field is three orders of magnitude stronger than typically observed magnetic fields in nearby radio-loud galaxies (e.g., $B \sim 45 - 65\mu$G; Carilli et al., 1991) (see more details on the P352–15 magnetic field uncertainties in Momjian et al. 2018). Furthermore, the uncertainties in our calculated synchrotron spectral break ν_{obs} are statistical rather than systematic.

Since jets are thought to be launched soon after the black hole begins accreting, we compare this jet timescale to an accretion disk timescale by constraining the past history of the ionizing UV emission via the proximity zone, or to the quasar lifetime t_Q.

4.7 MEASURING THE PROXIMITY ZONE R_p

The spectrum from P352–15 obtained in §4.4 was initially analyzed with the `linetools`[6] package in order to check the quality of the reduction process. Additionally, we

6 https://linetools.readthedocs.io/en/latest/xspecgui.html

checked for any absorbers in the line-of-sight presented in the spectra, primarily searching for possible LLS or DLA systems that could prematurely truncate the proximity zone and compromise the lifetime measurement (e.g., Eilers et al., 2017; Eilers et al., 2020) Indeed, we found absorption systems at various redshifts in the quasar spectrum, in particular, one system with strong low ionization absorption (N V, O I, Si II, C II, Si IV, C IV, Al II) identified at $z = 5.81924$, which is in the middle of the quasar proximity zone.

Low-ionization absorbers are usually associated with large H I column densities of $N_{HI} \gtrsim 10^{20}\,cm^{-2}$ (e.g., Poudel et al., 2018; Simcoe et al., 2020). Thus the absorber should block the ionizing emission from the quasar, preventing the proximity zone from existing at lower redshifts than the absorber's ($z < z_{abs}$). The high column density should give rise to a broad fully-absorbed trough around $z_{Ly\alpha} \sim z_{abs}$. This characteristic column density from the absorber would be too broad to allow the presence of flux transmission from the quasar ionizing the IGM as visible in the blueward region of the Lyα of P352–15, thus truncating the proximity zone. However, we observe substantial flux at the line position and further blueward of the spectrum (see Figure 4.5). This partial transmission effect suggests only a portion of the quasar's emission is being blocked by the absorber. Thus, this system must be physically associated with the quasar sub-pc environment, such as a small "metal cloud" launched from the quasar and present in the BLR (scale of BLR is $\sim 1/10^{th}$ pc), rather than a typical foreground DLA system at a lower redshift.

These types of absorbers in the sub-pc environment of quasars have been recently discovered in just a handful of low-redshift quasars, which have been christened 'ghost-DLA system' (e.g., Fathivavsari et al., 2017; Fathivavsari, 2020), one example intriguingly happens to be a radio-loud quasar at $z = 2.1$ with evidence of jet-ISM interaction (Gupta et al., 2022). In summary, the partial absorption seen in the spectrum of P352–15 still allows flux transmission from the quasar to be visible. Also, there is no truncation at $z < z_{abs}$ implying that we are still seeing foreground IGM over-ionized by the quasar. Consequently, we continue to measure an upper limit on the proximity zone R_p of P352–15.

4.7.1 *Continuum Emission Prediction using PCA*

The proximity zone R_p is defined as the region of the spectrum with transmission above 10% of the flux normalized by the continuum of the quasar. It is necessary to predict the intrinsic quasar continuum profile of the Lyα emission in order to measure the extent of the transmitted flux up to the 10% level. This continuum prediction is possible thanks to the natural strong correlation of the broad emission lines of a quasar's spectrum in the rest-frame UV (e.g., Francis et al., 1992; Yip et al., 2004; Suzuki, 2006; Greig et al., 2017). Therefore, it is possible to model the emission lines redward of Lyα to predict its intrinsic profile. This has been previously assessed by implementing principal component analysis (PCA) of spectra from a large sample of lower-redshift quasars ($z \lesssim 2$) where the Lyα emission is fully observed (e.g., Suzuki, 2006; Pâris et al., 2011; Davies et al., 2018). We used the recent PCA model from

Bosman et al. (2021) which we briefly explain here. The PCA training set consists of 4579 quasars from the eBOSS–SDSS DR14 catalog (Pâris et al., 2018). This method focuses on recovering the Lyα forest and was repurposed to recover the Lyα line in Chen et al. (2022). The PCA red-side modeling uses the spectrum at wavelengths $\lambda > 1290$Å (compared to the previously applied limit in Davies et al. (2018) where the PCA red-side was defined as $\lambda > 1280$Å). The predicted Lyα profile and bluer continuum is found using a projection matrix relating the red-side PCA coefficients to those in the blue-side of the PCA.

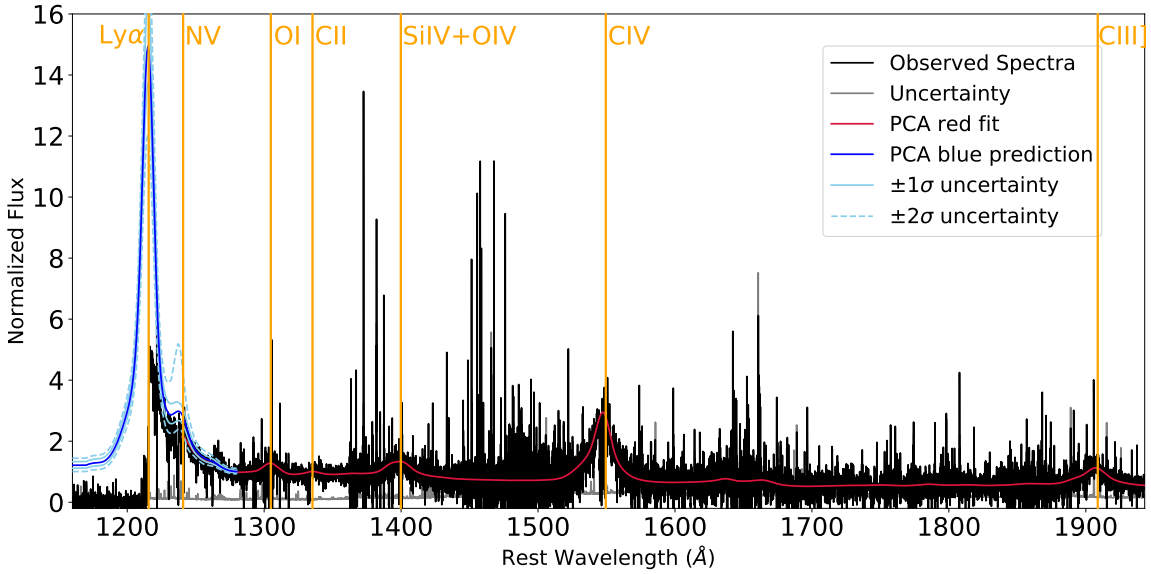

Figure 4.4: The spectrum of P352–15 normalized at rest-frame 1290 ± 2.5Å shows the measured flux (black) and uncertainty (grey). The anticipated emission lines at rest-frame wavelengths are represented by yellow vertical lines. The red-side PCA continuum fit (red) is performed by first removing any absorption features with a cubic-spline procedure. The PCA prediction of the blue-side continuum of the spectrum ($\lambda < 1290$ Å) is the blue line with $\pm 1\sigma, \pm 2\sigma$. The predicted continuum suggests a strong Lyα damping wing with only a third of the emission present close to line center.

To apply this updated PCA continuum modeling to the spectrum of P352–15, we first normalize the reduced spectrum from XShooter observations such that its median flux at $\lambda = 1290 \pm 2.5$ Å is unity. A cubic-spline procedure is applied to automatically and systematically remove absorbers in the spectrum so that the PCA is optimized to model the continuum from the spectrum. Finally, the red-side PCA components are fitted to the spectrum and we obtain the output of the blue-side PCA prediction of the quasar continuum. Figure 4.4 shows the PCA model for P352–15 using this method. The predicted blue-side spectrum lies well above the observed one, in particular, the predicted Lyα line is ~ 3—times weaker than the observed normalized spectrum. This discrepancy at the systemic Lyα and redward of the profile is then suggestive of a Lyα damping wing. Note that in the spectrum we also observe a

very strong broad C IV line from this quasar, which typically strongly correlates with the Lyα emission (e.g., Greig et al., 2017).

To calculate the transmitted flux in the proximity zone R_p, one must know precisely the position of the quasar. For this reason, the systemic redshift of the quasar is necessary to pinpoint the location where the absorption from the IGM begins. Thus, we use the $z_{sys} = 5.832 \pm 0.001$ found in Rojas-Ruiz et al. (2021) (Chapter 3). From this position, one measures the proximity zone up to where flux drops below the 10% level of the smoothed normalized spectrum. The observed spectrum of P352–15 is normalized by the predicted continuum emission (blue line in Figure 4.4), and is then smoothed with a 20 Å Boxcar kernel using the Astropy `convolution`. However, given the caveat of the absorption system presented in the quasar line-of-sight, the normalized spectrum at the position of the quasar is less than half of unity. Following the 10% level definition of the proximity zone would result in a biased measurement of a very short $R_p \sim 0.3$ pMpc (see Appendix A.3). The "shelf" in the smoothed flux in the center of the proximity zone is only a factor of ~ 2 below 10% transmission, thus correcting for the absorber would push the value of R_p out much further.

In lieu of modeling the partially covered absorption in detail, which we leave to future work, we instead roughly estimate the proximity zone size by measuring where the smoothed spectrum approaches the zero level, corresponding to $R_p \sim 2.0$ pMpc (see Figure 4.5).

4.8 ESTIMATING THE QUASAR LIFETIME t_Q

Following the methodology to calculate quasar lifetimes t_Q from proximity zones R_p in Eilers et al. (2017), radiative transfer simulations (RT) for a quasar matching the luminosity and redshift of P352–15 are necessary. The quasar absolute magnitude of the quasar is $M_{1450} = -25.59 \pm 0.13$ Bañados et al. 2018a. We use RT simulations from Davies, Hennawi, and Eilers (2020) evaluated for $M_{1450} = -25.6$ at $z = 6$. The measured R_p of P352–15 is small compared to the average measurements in Eilers et al. (2017) where quasars with $-27.5 \lesssim M_{1450} \lesssim -26.5$ have a corresponding $R_p = 3 - 7$ pMpc. However, a handful of quasars showing small proximity zones and therefore shorter t_Q have been identified in Eilers et al. (2021a) with $R_p = 0.3 - 1.9$ pMpc, which translates to $t_Q \lesssim 10^4$yrs. According to the RT simulations as shown in Figure 4.6, our proximity zone measurement of P352–15 $R_p \sim 2$ pMpc corresponds to a t_Q as young as $\sim 10^4$yrs, with 68% confidence limit that can extend this measurement even to $\sim 10^6$yrs.

4.9 DISCUSSION AND OUTLOOK

In this Chapter, we performed a new experiment to calculate the timescales for quasar activity and jet launch using the radio-loud quasar P352–15. This study is interesting because radio jets are thought to play a key role in the formation and growth mechanisms of SMBHs within the first billion years of the universe. These

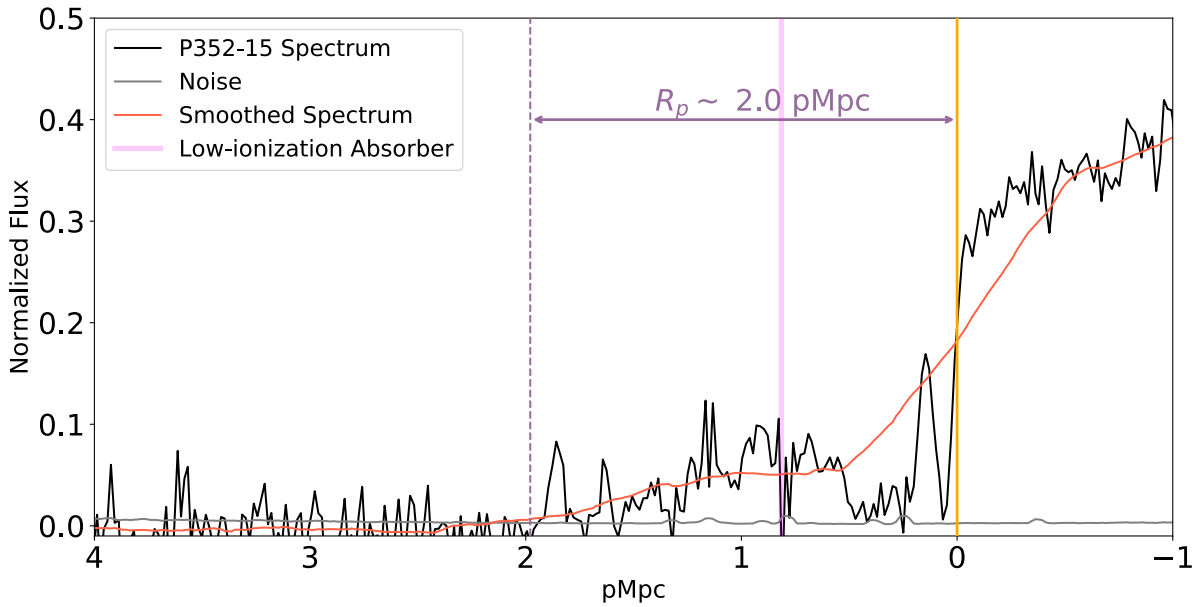

Figure 4.5: Spectrum of P352–15 normalized by the predicted continuum from the PCA analysis (black) and the noise (grey). Given the strong low ionization absorber (centered at the location of the pink vertical line), the normalized flux is less than half at the boundary of the position of the quasar. The flux smoothed with a boxcar kernel of 20 Å is shown in red. Notice that significant transmission extends from the position of the quasar (yellow vertical line) to where the transmission and the smoothed spectrum reach the zero level (purple dashed line), despite the presence of the strong absorber. This is the measured proximity zone; $R_p \sim 2$ pMpc. This R_p measurement is still taken with caution for the calculation of the quasar lifetime t_Q.

black holes with $\sim 10^{8-9}\,M_\odot$ already challenge black hole formation theories and thus jets can be a mechanism aiding this growth (e.g., Volonteri, Silk, and Dubus, 2015; Volonteri, Habouzit, and Colpi, 2023, and references within). However, whether jets emerge soon after black hole activity begins and enhance the accretion rate is challenging to study even at lower redshifts given the complexity of calculating these timescales. Fortunately, quasars at $z \gtrsim 6$ offer the advantage of allowing the calculation of quasar lifetimes from their proximity zone given that this lifetime arises from the quasar ionizing its surrounding environment composed mainly of neutral IGM. Thus, this pioneering experiment cannot be repeated for quasars at lower redshift (i.e., $z \sim 2$) where more radio-loud objects are known.

The VLA radio observations of P352–15 presented in this work depict the most detailed characterization of a radio-loud quasar in the epoch of reionization. Through the analysis of the intrinsic synchrotron break, we calculated the jet timescale since launch $t_{dyn} \sim 10^3$ yrs. The main caveat on this calculation relies on the accuracy of the magnetic field calculation provided in Momjian et al. (2018). It is important to note that solely one observation at high resolution of the jets is challenging to calculate this magnetic field. Additional multifrequency observations would be necessary to

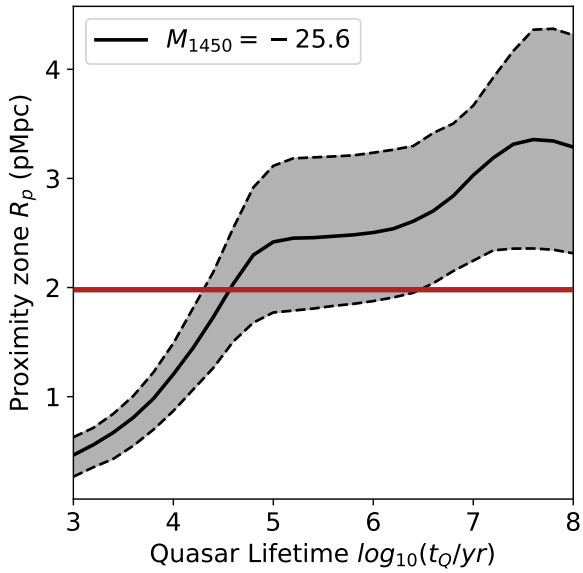

Figure 4.6: Distribution of the evolution of proximity zone sizes with quasar lifetime from radiative transfer simulations for a quasar with $M_{1450} = -25.$. The black line is the median of the distribution and the shaded grey area represents the 68% uncertainty. The horizontal red line is located at the proximity zone we measured of $R_p \sim 2$ pMpc. Based on this analysis, the estimated quasar lifetime of P352–15 is $\log_{10}(t_Q/yr) = 4.6^{+1.9}_{-0.3}$

better constrain this measurement. Finally, we note that there is still a gap between ~ 45 GHz and 100 GHz observations of P352–15. The only telescope on Earth that could help fill in the gap is ALMA but only at ~ 80 GHz, and the sensitivity at this frequency is challenging for the required observations.

The calculated lifetime for quasar activity for P352–15 is achieved by estimating its proximity zone, following the method developed in Eilers et al. (2017). When analyzing the quasar spectrum, we encountered a strong low ionization absorber that could possibly truncate the proximity zone. However, we see substantial flux transmission even at the central position of the absorber. Thus we could estimate a limit on the proximity zone corresponding to a quasar lifetime $t_Q \sim 10^4$ yrs. The rare ghost-DLA system is very interesting, and the fact that another highly radio-loud quasar at $z \sim 2.1$ (Gupta et al., 2022) shows a similar feature is suggestive of a connection between the two. We will examine the detailed nature of this ghost-DLA system in future work.

The calculated timescales for the jet and quasar lifetimes are found to be remarkably consistent despite their significant systematic uncertainties and wildly different physical phenomena. This provides direct evidence that the jet and accretion disk activity are strongly linked. The implied activity timescale of $\lesssim 10^4$ yrs is too small to grow the SMBH (see also Eilers, Hennawi, and Davies, 2018; Eilers et al., 2020; Eilers et al., 2022). This, therefore, suggests that the quasar is flickering (e.g., Davies, Hennawi, and Eilers, 2020; Satyavolu et al., 2023). This hypothesis could be tested by looking for the presence of jet emission at larger kpc-scales that would hint at a pre-

vious black hole-jet activity. In fact, Connor et al. (2021) suggested the presence of a possible X-ray jet at projected ~ 50 kpc from the quasar center. If this jet is confirmed in radio counterpart, then this would correspond to a jet launch accruing before the timescale we calculated in this Chapter where the extension of the jet is just ~ 1.6 kpc.

To sum up, our observing strategy demonstrates that it is possible to determine the age of a radio jet at $z \sim 6$, and compare it to the most recent black hole accretion timescale. Most importantly, this experiment can be repeated for the other handful of radio-loud quasars at similar redshifts (e.g. Bañados et al., 2018a; Gloudemans et al., 2022). Indeed, this work is the pilot program for a more ambitious survey of radio quasars at $z \gtrsim 6$, whose numbers will continue to increase with the next decade of observatories such as the next-generation VLA (ngVLA; McKinnon et al., 2019).

5

SUMMARY

In this thesis, we showed that quasars are fascinating objects from which we can learn the physics of the universe from the cosmic web, formation of galaxy protoclusters and IGM in the universe (Mpc-scale), to host galaxy and jet physics (kpc-scales), and the components close to the accretion disk of the quasar (subpc-scales). Below is a brief summary of all the studies presented here:

In Chapter 2, we pushed the redshift frontier on investigating quasar large-scale environments by surveying the 1.1 pMpc^2 of ULAS J1342+0928 at redshift $z = 7.54$ with Hubble Space Telescope (HST) and *Spitzer*. We reported a $z_{\rm phot} = 7.69$ LBG galaxy candidate at 223 projected pkpc from the quasar. However, we found that our survey of LBG candidates at $z \sim 7.5$ is incomplete when compared to the galaxy number density measured in the CANDELS/GOODS deep blank fields. This deficit is due to the lack of a second band redward of the Lyman-break in the F105W filter, which would produce a more accurate UV color of the candidates. The found number density in the ULAS J1342+0928 field indicates a marginally overdense environment of LBGs with 0.9σ significance. Together with one dust-obscured galaxy previously found with ALMA at 27 projected pkpc and $z_{\rm [C\,II]} = 7.5341 \pm 0.0009$, suggest a galaxy overdensity around ULAS J1342+0928. Two LBG candidates were also identified with a $z_{\rm phot}$ consistent with a known $z = 6.84$ absorber in the line-of-sight of the quasar. All these galaxy candidates are excellent targets for follow-up observations with JWST and/or ALMA to confirm their redshift and physical properties.

In Chapter 3, we investigated the radio-loud quasar PSO J352.4034–15.3373 (P352–15) and calculated its systemic redshift $z_{\rm sys} = 5.832 \pm 0.001$ from ALMA observations of [C II] emission from the host galaxy. This quasar is among the most powerful radio emitters and the first one with direct evidence of extended radio jets (~1.6 kpc) at these high redshifts. Thus we explored whether the presence of the jet influenced the host galaxy's properties. For this, we modeled the SED in the millimeter and radio emission. We used our ALMA and NOEMA observations to model the cold dust from the host galaxy using a modified black body function. The synchrotron emission from the jet of the quasar was constructed using available measurements from known VLAS and NVSS surveys, in addition to our GMRT observations. We found that in contrast to what is typically observed in high-redshift radio-quiet quasars, the cold dust emission alone could not reproduce the millimeter continuum mea-

surements because of a spectral break in the synchrotron spectrum. This is evidence that the strong synchrotron emission from the quasar contributes substantially to the emission from the host galaxy.

In Chapter 4 we continued to explore the jet effects observed in the previous Chapter. We examined closer the break in the synchrotron spectrum of P352–15 to pinpoint the frequency break ν_{obs}^{break} and calculate the spectral again from the jet shocking with the ISM. For this, we performed observations with the VLA in all continuous bands L through Q and their subband observations where available, covering a total range of (1.5 - 44) GHz. We found the frequency spectral break in the synchrotron emission by fitting a MBB model describing the cold dust emission in combination with two models describing spectral breaks from the literature. Using the ν_{obs}^{break} from the two models, and the previously measured strong magnetic field $B = 3.5\,mG$, we calculated the jet's spectral aging $t_{spec} = (4.7 - 6.9) \times 10^2\,yrs$. Considering the jet's relativistic boosting, the dynamical age describing the time since the jet launched is just ~10-times older, resulting in a surprisingly young $t_{dyn} \sim 10^3\,yrs$. We compared this age to that of the latest black hole accretion event, or the *quasar lifetime* t_Q, since the timescales for black hole accretion and jet launch are thought to be comparative.

We use rest-UV XShooter spectral observations of P352–15 to calculate t_Q from the proximity zone R_p. However, we encountered multiple strong metal absorbers in the spectrum that could affect the measurement of the R_p. We explored the hypothesis of dense clouds in the BLR subpc-environment of P352–15 acting as a ghost-DLA system and took caution when estimating the size of R_p. We found an upper limit for $R_p \sim 2\,pMpc$ that, after running radiative transfer simulations, corresponds to a t_Q of $\sim 10^4$ yrs. The timescale since the last black hole accretion event is consistent with the jet launch timeline within an order of magnitude. Therefore, we concluded that P352–15 is a very young system and is an exciting pioneering experiment to study black hole, jet, and host galaxy interactions in radio-loud quasars present during the first Gyr of the universe.

A

APPENDIX

A.1 TESTS TO MAKE THE EPSF FROM HST FILTER SET

This Appendix corresponds to Chapter 2 and presents the attempt at obtaining the effective point-spread functions (ePSFs) of the i_{814}, Y_{105}, and J_{125} *HST* filters to perform PSF-matching in our images. Usually, to get the ePSF from an image one can stack non-saturated stars that are not affected by near bright neighbors or that are located at the edges of the image. However, as mentioned in Chapter 2, the ~ 1 pMpc^2 field around the quasar has just a few stars satisfying these criteria (22 stars). Consequently, the built ePSF and calculated FWHM cannot be used to make a kernel and PSF-match the i_{814}, Y_{105} to the J_{125} image that has the largest PSF (see Figure A.1). Thus, we used the *HST* ePSFs provided by STScI, as mentioned in Chapter 2 §2.2.

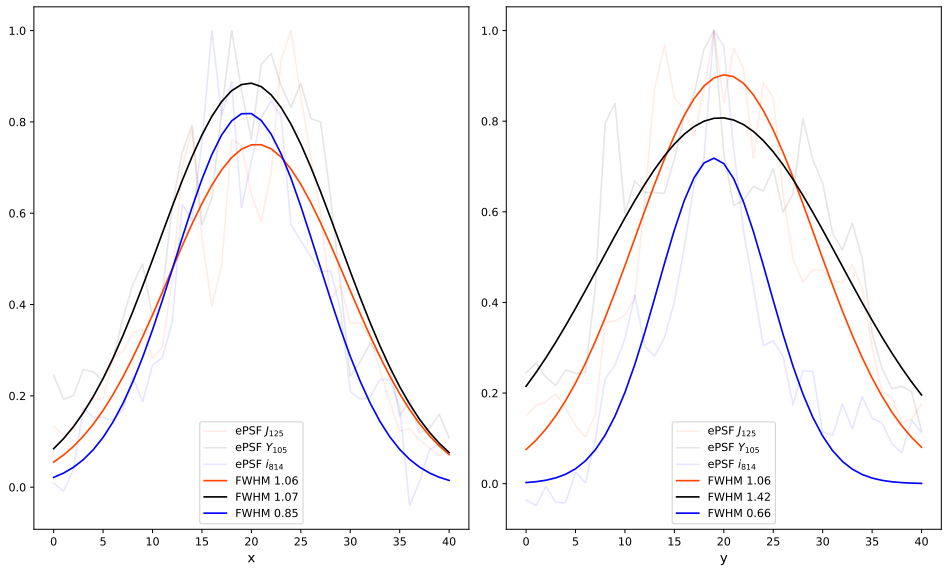

Figure A.1: Graph showing the effective point-spread functions (ePSFs) and calculated FWHM from the three *HST* filters used in this work. The left and right panels show the median-normalized ePSFs from the three filters i_{814}, Y_{105}, and J_{125} in red, green, and blue, correspondingly. Note that the ePSF is collapsed along the x and y direction to calculate the FWHM. Note that the FWHM for all filters changes considerably and is not consistent with the ePSFs created from the few stacked stars.

A.2 DENSITY OF QUASAR ENVIRONMENT AT $z = 7.5$

In Chapter 2 we explored the number density of LBGs around the luminous quasar at $z = 7.54$ ULAS J1342+0928. Below we show how we determined the average number density of LBGs found in the quasar field of $\sim$ 1pMpc^2. We calculated the number of expected LBGs from the UV-luminosity function at $z \sim 7.5$ and correcting by the completeness we found using the GOODS blank field from Finkelstein et al., 2015. This resulted in 0.2 LBGs with magnitude $J_{125} < 26.5$ expected in the area of our search (green line below). Since we found the one LBG associated with the quasar field, the environment is marginally overdense (5×), but dominated by low number statistics (Poisson errors in shaded pink) resulting in a 0.9σ significance. However, this result is from considering $z \sim 7.5$ LBGs in a determined area of the sky, not consider the QSO-LBG clustering which is further explained in the Chapter.

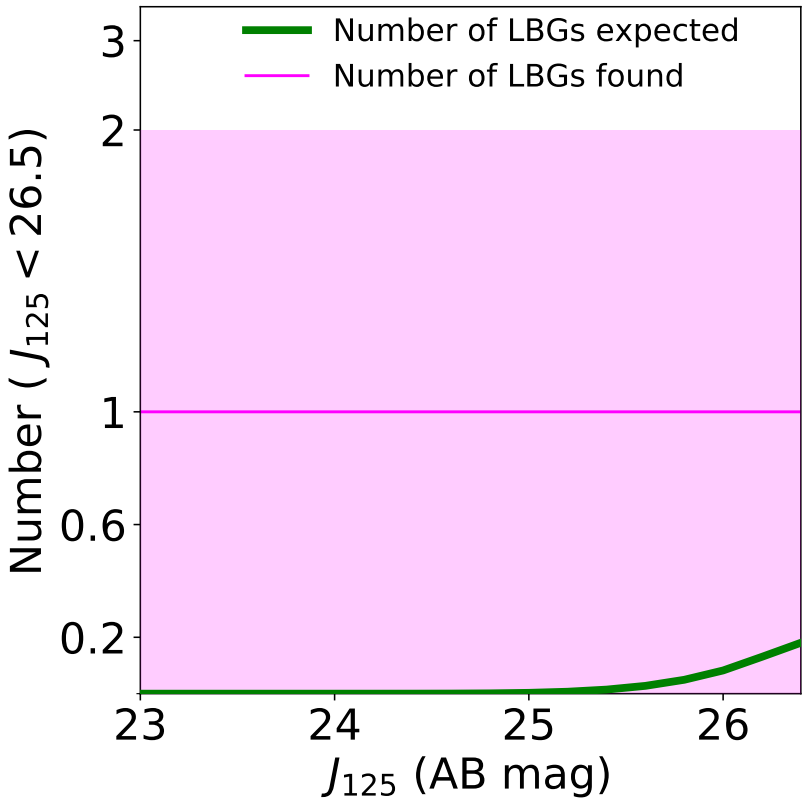

Figure A.2: Exploring an overdensity of LBGs in the $z = 7.54$ quasar field. The green line shows the number of galaxies expected at $z \sim 7.5$ with magnitude $J_{125} < 26.5$ in an average number density from blank fields (GOODS;Finkelstein et al., 2015) corrected by the completeness of our work, which is just 0.2. The magenta line presents the one LBG candidate found in the $\sim$ 1 pMpc^2 quasar field, and the shaded region is the Poisson uncertainty. The findings from this work imply a 5-times overdense environment, however this overdensity is of 0.9σ significance.

A.3 ABSORPTION SYSTEMS IN THE SPECTRUM OF P352−15

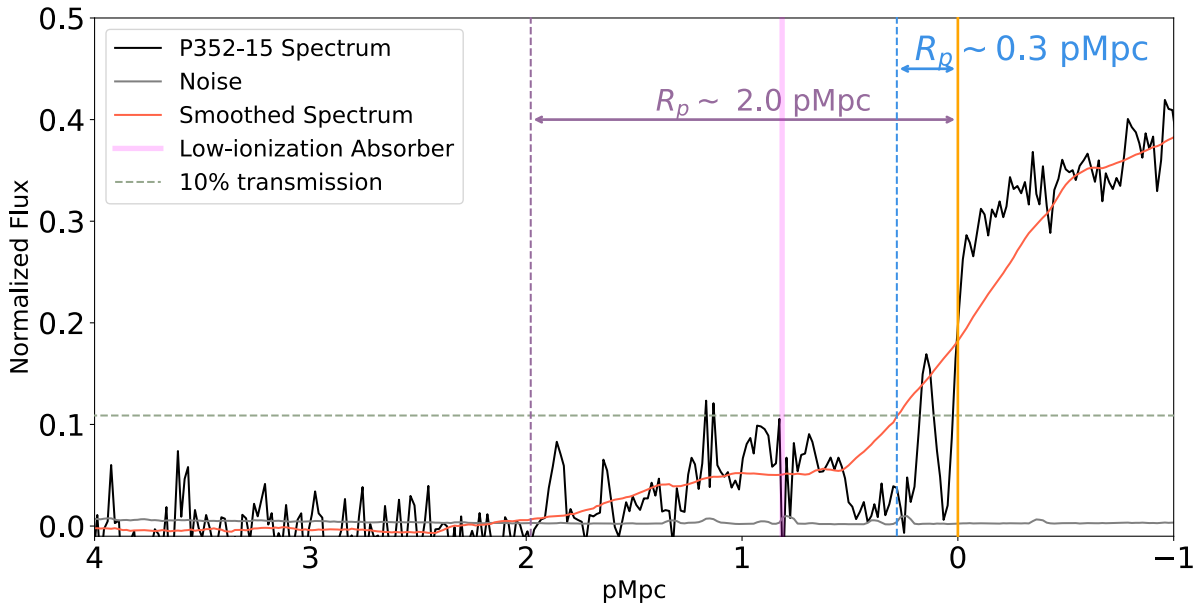

Figure A.3: This figure shows the normalized spectrum of P352–15 (black) and the noise (grey). The flux smoothed with a boxcar kernel of 20 Å is shown in red. The horizontal dashed line indicates 10% of the normalized spectrum. Traditionally, the proximity zone R_p is measured from the position of the quasar (yellow vertical line) to where the smoothed flux drops below the 10% level (indicated by the blue vertical dashed line). However, given the caveat of the absorption system presented in the quasar line-of-sight (centered at the location of the pink vertical line), the resulting proximity zone measurement is biased to a very short $R_p \sim 0.3$ pMpc. Notice that significant transmission extends even further out and hence we chose to measure the R_p up to where the transmission and the smoothed spectrum reach the zero level (purple; $R_p \sim 2$ pMpc). This R_p measurement is still taken with caution for the calculation of the quasar lifetime t_Q (see §4.8.)

BIBLIOGRAPHY

Abel, Tom, Greg L. Bryan, and Michael L. Norman (Sept. 2000). "The Formation and Fragmentation of Primordial Molecular Clouds." In: *ApJ* 540, pp. 39–44. DOI: 10.1086/309295.

Alpher, R. A., H. Bethe, and G. Gamow (Apr. 1948). "The Origin of Chemical Elements." In: *Phys. Rev.* 73.7, pp. 803–804. DOI: 10.1103/PhysRev.73.803.

Amaro-Seoane, Pau et al. (Dec. 2023). "Astrophysics with the Laser Interferometer Space Antenna." In: *LRR* 26, p. 2. DOI: 10.1007/s41114-022-00041-y.

Anand, Gagandeep S. et al. (June 2022). "Comparing Tip of the Red Giant Branch Distance Scales: An Independent Reduction of the Carnegie-Chicago Hubble Program and the Value of the Hubble Constant." In: *ApJ* 932, p. 15. DOI: 10.3847/1538-4357/ac68df.

Andika, Irham Taufik et al. (June 2022). "Staring at the Shadows of Archaic Galaxies: Damped Lya and Metal Absorbers Toward a Young z = 6 Weak-line Quasar." In: *AJ* 163, p. 251. DOI: 10.3847/1538-3881/ac6422.

Antonucci, Robert (1993). "Unified models for active galactic nuclei and quasars." en. In: *ARA&A* 31, pp. 473–521. DOI: 10.1146/annurev.aa.31.090193.002353.

Bagley, Micaela B. et al. (May 2022). "Bright z~9 Galaxies in Parallel: The Bright End of the Rest-UV Luminosity Function from HST Parallel Programs." In: *2022arXiv220512980B*. DOI: 10.48550/arXiv.2205.12980.

Baldwin, J. A., M. M. Phillips, and R. Terlevich (Feb. 1981). "Classification parameters for the emission-line spectra of extragalactic objects." en. In: *PASP* 93.551, p. 5. DOI: 10.1086/130766.

Bañados, E. et al. (May 2015a). "Bright [C II] 158 {\ensuremath{\mu}}m Emission in a Quasar Host Galaxy at z = 6.54." In: *ApJL* 805, p. L8. DOI: 10.1088/2041-8205/805/1/L8.

Bañados, E. et al. (May 2015b). "Constraining the radio-loud fraction of quasars at z > 5.5." en. In: *ApJ* 804.2, p. 118. DOI: 10.1088/0004-637X/804/2/118.

Bañados, E. et al. (Nov. 2016). "THE PAN-STARRS1 DISTANT z > 5.6 QUASAR SURVEY: MORE THAN 100 QUASARS WITHIN THE FIRST GYR OF THE UNIVERSE." en. In: *ApJS* 227.1, p. 11. DOI: 10.3847/0067-0049/227/1/11.

Bañados, Eduardo et al. (Aug. 2013). "The Galaxy Environment of a QSO at $z \sim 5.7$." In: *ApJ* 773, p. 178. DOI: 10.1088/0004-637X/773/2/178.

Bañados, Eduardo et al. (July 2018a). "A Powerful Radio-loud Quasar at the End of Cosmic Reionization." en. In: *ApJ* 861.2, p. L14. DOI: 10.3847/2041-8213/aac511.

Bañados, Eduardo et al. (Jan. 2018b). "An 800-million-solar-mass black hole in a significantly neutral Universe at a redshift of 7.5." en. In: *Nature* 553.7689, pp. 473–476. DOI: 10.1038/nature25180.

Bañados, Eduardo et al. (Apr. 2018c). "Chandra X-Rays from the Redshift 7.54 Quasar ULAS J1342+0928." In: *APJL* 856, p. L25. DOI: 10.3847/2041-8213/aab61e.

Bañados, Eduardo et al. (Mar. 2021). "The Discovery of a Highly Accreting, Radio-loud Quasar at z = 6.82." en. In: *ApJ* 909.1, p. 80. DOI: 10.3847/1538-4357/abe239.

Becker, George D., James S. Bolton, and Adam Lidz (Dec. 2015). "Reionisation and High-Redshift Galaxies: The View from Quasar Absorption Lines." In: *PASA* 32, e045. DOI: 10.1017/pasa.2015.45.

Becker, Robert H. et al. (Dec. 2001). "Evidence for Reionization at $z\sim6$: Detection of a Gunn-Peterson Trough in a z = 6.28 Quasar." en. In: *AJ* 122.6, p. 2850. DOI: 10.1086/324231.

Beelen, Alexandre et al. (May 2006). "350 {\ensuremath{\mu}}m Dust Emission from High-Redshift Quasars." en. In: *ApJ* 642, p. 8. DOI: 10.1086/500636.

Bell, A. R. (Feb. 1978). "The acceleration of cosmic rays in shock fronts." In: *MNRAS* 182.2, pp. 147–156. DOI: 10.1093/mnras/182.2.147.

Belladitta, S. et al. (Sept. 2019). "An extremely X-ray weak blazar at z = 5." In: *A&A* 629, A68. DOI: 10.1051/0004-6361/201935965.

Belladitta, S. et al. (Mar. 2020). "The first blazar observed at $z > 6$." en. In: *A&A* 635, p. L7. DOI: 10.1051/0004-6361/201937395.

Bertin, E. and S. Arnouts (June 1996). "SExtractor: Software for source extraction." en. In: *A&AS* 117, p. 393. DOI: 10.1051/aas:1996164.

Birrer, S. et al. (Apr. 2019). "HoLiCOW - IX. Cosmographic analysis of the doubly imaged quasar SDSS 1206+4332 and a new measurement of the Hubble constant." In: *MNRAS* 484. ADS Bibcode: 2019MNRAS.484.4726B, pp. 4726–4753. DOI: 10.1093/mnras/stz200.

Bischetti, M. et al. (Oct. 2019). "Widespread QSO-driven outflows in the early Universe." In: *A&A* 630, A59. DOI: 10.1051/0004-6361/201833557.

Biscoveanu, Sylvia et al. (Dec. 2020). "Measuring the Primordial Gravitational-Wave Background in the Presence of Astrophysical Foregrounds." en. In: *Phys. Rev. Lett* 125.24, p. 241101. DOI: 10.1103/PhysRevLett.125.241101.

Blundell, Katherine M. and Steve Rawlings (Mar. 2000). "The Spectra and Energies of Classical Double Radio Lobes." In: *AJ* 119, pp. 1111–1122. DOI: 10.1086/301254.

Bolton, James S. and Martin G. Haehnelt (Jan. 2007). "The nature and evolution of the highly ionized near-zones in the absorption spectra of z ~= 6 quasars." In: *MNRAS* 374, pp. 493–514. DOI: 10.1111/j.1365-2966.2006.11176.x.

Borse, Nikhil et al. (May 2021). "Numerical study of the Kelvin-Helmholtz instability and its effect on synthetic emission from magnetized jets." en. In: *Astronomy & Astrophysics, Volume 649, id.A150, <NUMPAGES>17</NUMPAGES> pp.* 649, A150. DOI: 10.1051/0004-6361/202140440.

Bosman, Sarah E. I. et al. (June 2020). "Three Lya Emitting Galaxies within a Quasar Proximity Zone at $z \sim 5.8$." In: *ApJ* 896, p. 49. DOI: 10.3847/1538-4357/ab85cd.

Bosman, Sarah E. I. et al. (May 2021). "A comparison of quasar emission reconstruction techniques for z > 5.0 Lyman-alpha and Lyman-beta transmission." In: *MNRAS* 503, pp. 2077–2096. DOI: 10.1093/mnras/stab572.

Bosman, Sarah E. I. et al. (July 2022). "Hydrogen reionization ends by z = 5.3: Lyman-{\ensuremath{\alpha}} optical depth measured by the XQR-30 sample." In: *MNRAS* 514. ADS Bibcode: 2022MNRAS.514...55B, pp. 55–76. DOI: 10.1093/mnras/stac1046.

Boucaud, A. et al. (Dec. 2016). "Convolution kernels for multi-wavelength imaging." en. In: *A&A* 596, A63. DOI: 10.1051/0004-6361/201629080.

Bouwens, R. J. et al. (Feb. 2010). "Discovery of z ~ 8 Galaxies in the Hubble Ultra Deep Field from Ultra-Deep WFC3/IR Observations." In: *ApJL* 709. ADS Bibcode: 2010ApJ...709L.133B, pp. L133–L137. DOI: 10.1088/2041-8205/709/2/L133.

Bouwens, R. J. et al. (Apr. 2015). "UV LUMINOSITY FUNCTIONS AT REDSHIFTS $z \sim 4$ TO $z \sim 10$: 10,000 GALAXIES FROM HST LEGACY FIELDS." en. In: *ApJ* 803.1, p. 34. DOI: 10.1088/0004-637X/803/1/34.

Bouwens, R. J. et al. (Oct. 2016). "The Bright End of the $z \sim 9$ and $z \sim 10$ UV Luminosity Functions Using All Five CANDELS Fields." In: *ApJ* 830, p. 67. DOI: 10.3847/0004-637X/830/2/67.

Bouwens, R. J. et al. (July 2019). "Newly Discovered Bright $z \sim9-10$ Galaxies and Improved Constraints on Their Prevalence Using the Full CANDELS Area." In: *ApJ* 880, p. 25. DOI: 10.3847/1538-4357/ab24c5.

Bouwens, R. J. et al. (Aug. 2021). "New Determinations of the UV Luminosity Functions from z 9 to 2 Show a Remarkable Consistency with Halo Growth and a Constant Star Formation Efficiency." In: *AJ* 162, p. 47. DOI: 10.3847/1538-3881/abf83e.

Bower, R. G., A. J. Benson, and Robert A. Crain (June 2012). "What shapes the galaxy mass function? Exploring the roles of supernova-driven winds and active galactic nuclei." In: *MNRAS* 422, pp. 2816–2840. DOI: 10.1111/j.1365-2966.2012.20516.x.

Bradley, L. D. et al. (Dec. 2012). "The Brightest of Reionizing Galaxies Survey: Constraints on the Bright End of the z ~ 8 Luminosity Function." In: *ApJ* 760, p. 108. DOI: 10.1088/0004-637X/760/2/108.

Brammer, Gabriel B., Pieter G. van Dokkum, and Paolo Coppi (Oct. 2008). "EAZY: A Fast, Public Photometric Redshift Code." In: *ApJ* 686, pp. 1503–1513. DOI: 10.1086/591786.

Brammer, Gabriel (Oct. 2022). "gbrammer/golfir: Software pipeline for model photometry on images with different point spread functions." In: *Zenodo*. DOI: 10.5281/zenodo.7149516.

Briggs, Daniel S., Frederic R Schwab, and Richard A. Sramek (Jan. 1999). "Imaging." In: *ASPC*. Astronomical Society of the Pacific Conference Series 180, p. 127.

Bromm, Volker, Paolo S. Coppi, and Richard B. Larson (Dec. 1999). "Forming the First Stars in the Universe: The Fragmentation of Primordial Gas." In: *ApJ* 527, pp. L5–L8. DOI: 10.1086/312385.

Calvi, V. et al. (Feb. 2016). "Bright Galaxies at Hubble's Redshift Detection Frontier: Preliminary Results and Design from the Redshift z ~ 9-10 BoRG Pure-Parallel HST Survey." In: *ApJ* 817, p. 120. DOI: 10.3847/0004-637X/817/2/120.

Cardelli, Jason A., Geoffrey C. Clayton, and John S. Mathis (Oct. 1989). "The Relationship between Infrared, Optical, and Ultraviolet Extinction." In: *ApJ* 345, p. 245. DOI: 10.1086/167900.

Carilli, C. L. et al. (Dec. 1991). "Multifrequency radio observations of Cygnus A - Spectral aging in powerful radio galaxies." In: *ApJ* 383, pp. 554–573. DOI: 10.1086/170813.

Carilli, C.L. and F. Walter (Aug. 2013). "Cool Gas in High-Redshift Galaxies." en. In: *ARA&A* 51.1, pp. 105–161. DOI: 10.1146/annurev-astro-082812-140953.

Cen, Renyue and Zoltan Haiman (Oct. 2000). "Quasar Strömgren Spheres Before Cosmological Reionization." In: *ApJ* 542, pp. L75–L78. DOI: 10.1086/312937.

Chabrier, Gilles (July 2003). "Galactic Stellar and Substellar Initial Mass Function." en. In: *PASP* 115.809, pp. 763–795. DOI: 10.1086/376392.

Champagne, Jaclyn B. et al. (Nov. 2018). "No Evidence for Millimeter Continuum Source Overdensities in the Environments of $z \gtrsim 6$ Quasars." In: *ApJ* 867, p. 153. DOI: 10.3847/1538-4357/aae39610.48550/arXiv.1809.10178.

Chen, Huanqing et al. (May 2022). "Measuring the Density Fields around Bright Quasars at z 6 with XQR-30 Spectra." In: *The Astrophysical Journal* 931. ADS Bibcode: 2022ApJ...931...29C, p. 29. DOI: 10.3847/1538-4357/ac658d.

Chiang, Yi-Kuan, Roderik Overzier, and Karl Gebhardt (Dec. 2013). "Ancient Light from Young Cosmic Cities: Physical and Observational Signatures of Galaxy Proto-clusters." In: *ApJ* 779, p. 127. DOI: 10.1088/0004-637X/779/2/127.

Choi, Ena et al. (Aug. 2012). "Radiative and Momentum-based Mechanical Active Galactic Nucleus Feedback in a Three-dimensional Galaxy Evolution Code." In: *ApJ* 754, p. 125. DOI: 10.1088/0004-637X/754/2/125.

Clough, S. A. et al. (Mar. 2005). "Atmospheric radiative transfer modeling: a summary of the AER codes." en. In: *JQSRT* 91.2, pp. 233–244. DOI: 10.1016/j.jqsrt.2004.05.058.

Coe, Dan et al. (Jan. 2013). "CLASH: Three Strongly Lensed Images of a Candidate $z \approx 11$ Galaxy." In: *ApJ* 762, p. 32. DOI: 10.1088/0004-637X/762/1/32.

Connor, Thomas et al. (Dec. 2019). "X-Ray Observations of a $z \sim 6.2$ Quasar/-Galaxy Merger." In: *ApJ* 887, p. 171. DOI: 10.3847/1538-4357/ab5585.

Connor, Thomas et al. (Apr. 2021). "Enhanced X-Ray Emission from the Most Radio-powerful Quasar in the Universe's First Billion Years." en. In: *ApJ* 911.2, p. 120. DOI: 10.3847/1538-4357/abe710.

Conroy, Charlie and James E. Gunn (Apr. 2010). "The Propagation of Uncertainties in Stellar Population Synthesis Modeling. III. Model Calibration, Comparison, and Evaluation." In: *ApJ* 712, pp. 833–857. DOI: 10.1088/0004-637X/712/2/833.

Conroy, Charlie, James E. Gunn, and Martin White (July 2009). "The Propagation of Uncertainties in Stellar Population Synthesis Modeling. I. The Relevance of Uncertain Aspects of Stellar Evolution and the Initial Mass Function to the Derived Physical Properties of Galaxies." In: *ApJ* 699, pp. 486–506. DOI: 10.1088/0004-637X/699/1/486.

Costa, Tiago et al. (Apr. 2014). "The environment of bright QSOs at $z \sim 6$: star-forming galaxies and X-ray emission." en. In: *MNRAS* 439.2, pp. 2146–2174. DOI: 10.1093/mnras/stu101.

Cunha, Elisabete da et al. (Mar. 2013). "On the Effect of the Cosmic Microwave Background in High-redshift (Sub-)millimeter Observations." en. In: *ApJ* 766.1, p. 13. DOI: 10.1088/0004-637X/766/1/13.

Curtis-Lake, Emma et al. (Dec. 2022). "Spectroscopic confirmation of four metal-poor galaxies at z=10.3-13.2." In: *2022arXiv221204568C*. DOI: 10.48550/arXiv.2212.04568.

Davies, Frederick B., Steven R. Furlanetto, and Matthew McQuinn (Apr. 2016). "Quasar ionization front Lya emission in an inhomogeneous intergalactic medium." In: *MNRAS* 457, pp. 3006–3023. DOI: 10.1093/mnras/stw055.

Davies, Frederick B., Joseph F. Hennawi, and Anna-Christina Eilers (Mar. 2020). "Time-dependent behaviour of quasar proximity zones at z = 6." In: *MNRAS* 493, pp. 1330–1343. DOI: 10.1093/mnras/stz3303.

Davies, Frederick B. et al. (Sept. 2018). "Predicting Quasar Continua near Lya with Principal Component Analysis." In: *ApJ* 864, p. 143. DOI: 10.3847/1538-4357/aad7f8.

De Breuck, Carlos et al. (May 2014). "ALMA resolves turbulent, rotating [CII] emission in a young starburst galaxy at z = 4.8." en. In: *A&A* 565, A59. DOI: 10.1051/0004-6361/201323331.

De Looze, Ilse et al. (Aug. 2014). "The applicability of far-infrared fine-structure lines as star formation rate tracers over wide ranges of metallicities and galaxy types." en. In: *A&A* 568, A62. DOI: 10.1051/0004-6361/201322489.

Decarli, R. et al. (May 2017). "Rapidly star-forming galaxies adjacent to quasars at redshifts exceeding 6." In: *Nature* 545, pp. 457–461. DOI: 10.1038/nature22358.

Decarli, Roberto et al. (Sept. 2012). "Hubble Space Telescope Narrowband Search for Extended Lya Emission around Two $z > 6$ Quasars." In: *ApJ* 756, p. 150. DOI: 10.1088/0004-637X/756/2/150.

Decarli, Roberto et al. (Feb. 2018). "An ALMA [C ii] Survey of 27 Quasars at $z > 5.94$." en. In: *ApJ* 854.2, p. 97. DOI: 10.3847/1538-4357/aaa5aa.

Dijkstra, Mark and Abraham Loeb (Nov. 2008). "Lya-driven outflows around star-forming galaxies." In: *MNRAS* 391.1, pp. 457–466. DOI: 10.1111/j.1365-2966.2008.13920.x.

Doughty, Caitlin C. and Kristian M. Finlator (Jan. 2023). "The environments and hosts of metal absorption at z > 5." In: *MNRAS* 518, pp. 4159–4171. DOI: 10.1093/mnras/stac3342.

Dunne, L. et al. (June 2000). "The SCUBA Local Universe Galaxy Survey – I. First measurements of the submillimetre luminosity and dust mass functions." en. In: *MNRAS* 315.1, pp. 115–139. DOI: 10.1046/j.1365-8711.2000.03386.x.

Dunne, Loretta, Stephen A Eales, and M G Edmunds (2003). "A census of metals at high and low redshift and the connection between submillimetre sources and spheroid formation." en. In: *MNRAS*, p. 10. DOI: 10.1046/j.1365-8711.2003.06440.x.

Duric, Nebojsa, Eric Bourneuf, and P. C. Gregory (July 1988). "The separation of synchrotron and bremsstrahlung radio emission in spiral galaxies." en. In: *AJ* 96, p. 81. DOI: 10.1086/114791.

Dutta, Rajeshwari et al. (Dec. 2020). "MUSE Analysis of Gas around Galaxies (MAGG) - II: metal-enriched halo gas around $z \sim 1$ galaxies." en. In: *MNRAS* 499.4, p. 5022. DOI: 10.1093/mnras/staa3147.

Díaz-Santos, T. et al. (Aug. 2017). "AHerschel/PACS Far-infrared Line Emission Survey of Local Luminous Infrared Galaxies." en. In: *ApJ* 846.1, p. 32. DOI: 10.3847/1538-4357/aa81d7.

Eilers, Anna-Christina, Joseph F. Hennawi, and Frederick B. Davies (Nov. 2018). "First Spectroscopic Study of a Young Quasar." In: *ApJ* 867. ADS Bibcode: 2018ApJ...867...30E, p. 30. DOI: 10.3847/1538-4357/aae081.

Eilers, Anna-Christina et al. (May 2017). "Implications of $z \sim 6$ Quasar Proximity Zones for the Epoch of Reionization and Quasar Lifetimes." In: *ApJ* 840, p. 24. DOI: 10.3847/1538-4357/aa6c60.

Eilers, Anna-Christina et al. (Sept. 2020). "Detecting and Characterizing Young Quasars. I. Systemic Redshifts and Proximity Zone Measurements." In: *ApJ* 900, p. 37. DOI: 10.3847/1538-4357/aba52e.

Eilers, Anna-Christina et al. (Aug. 2021a). "Detecting and Characterizing Young Quasars. II. Four Quasars at z 6 with Lifetimes < 104 Yr." In: *ApJ* 917, p. 38. DOI: 10.3847/1538-4357/ac0a76.

Eilers, Anna-Christina et al. (June 2021b). "Erratum: "Detecting and Characterizing Young Quasars. I. Systemic Redshifts and Proximity Zones Measurements" (2020, ApJ, 900, 37)." In: *ApJ* 914, p. 74. DOI: 10.3847/1538-4357/ac05c3.

Eilers, Anna-Christina et al. (Oct. 2022). "A Generative Model for Quasar Spectra." In: *ApJ* 938, p. 17. DOI: 10.3847/1538-4357/ac8ead.

Erb, Dawn K. et al. (Aug. 2010). "Physical Conditions in a Young, Unreddened, Low-metallicity Galaxy at High Redshift." In: *ApJ* 719, pp. 1168–1190. DOI: 10.1088/0004-637X/719/2/1168.

Fan, Xiaohui, Eduardo Banados, and Robert A. Simcoe (Dec. 2022). "Quasars and the Intergalactic Medium at Cosmic Dawn." In: *ARA&A* 2022arXiv221206907F.

Fan, Xiaohui et al. (July 2006). "Constraining the Evolution of the Ionizing Background and the Epoch of Reionization with z~6 Quasars. II. A Sample of 19 Quasars." In: *AJ* 132, pp. 117–136. DOI: 10.1086/504836.

Farina, Emanuele P. et al. (Oct. 2017). "Mapping the Lya Emission around a $z \sim 6.6$ QSO with MUSE: Extended Emission and a Companion at a Close Separation." In: *ApJ* 848, p. 78. DOI: 10.3847/1538-4357/aa8df4.

Farina, Emanuele Paolo et al. (Dec. 2022). "The X-shooter/ALMA Sample of Quasars in the Epoch of Reionization. II. Black Hole Masses, Eddington Ratios, and the Formation of the First Quasars." In: *ApJ* 941, p. 106. DOI: 10.3847/1538-4357/ac962610.48550/arXiv.2207.05113.

Farrah, D. et al. (Sept. 2013). "FAR-INFRARED FINE-STRUCTURE LINE DIAGNOSTICS OF ULTRALUMINOUS INFRARED GALAXIES." en. In: *ApJ* 776.1, p. 38. DOI: 10.1088/0004-637X/776/1/38.

Fathivavsari, H. et al. (Mar. 2017). "A ghostly damped Lya system revealed by metal absorption lines." In: *MNRAS* 466, pp. L58–L62. DOI: 10.1093/mnrasl/slw233.

Fathivavsari, Hassan (Jan. 2020). "Ghostly Strong Lya Absorbers: Tracers of Gas Flows in the Close Vicinity of Quasars?" In: *ApJ* 888, p. 85. DOI: 10.3847/1538-4357/ab59da.

Finkelstein, Steven L. (2016). "Observational Searches for Star-Forming Galaxies at z > 6." en. In: *PASA* 33, e037. DOI: 10.1017/pasa.2016.26.

Finkelstein, Steven L. et al. (Aug. 2010). "On the Stellar Populations and Evolution of Star-forming Galaxies at 6.3 < z <= 8.6." In: *ApJ* 719, pp. 1250–1273. DOI: 10.1088/0004-637X/719/2/1250.

Finkelstein, Steven L. et al. (Sept. 2012). "Candels: The Evolution of Galaxy Rest-frame Ultraviolet Colors from z = 8 to 4." In: *ApJ* 756, p. 164. DOI: 10.1088/0004-637X/756/2/164.

Finkelstein, Steven L. et al. (Sept. 2015). "The evolution of the galaxy rest-frame ultraviolet luminosity function over the first two billion years." en. In: *ApJ* 810.1, p. 71. DOI: 10.1088/0004-637X/810/1/71.

Finkelstein, Steven L. et al. (Mar. 2022). "A Census of the Bright z = 8.5-11 Universe with the Hubble and Spitzer Space Telescopes in the CANDELS Fields." In: *ApJ* 928, p. 52. DOI: 10.3847/1538-4357/ac3aed.

Fossati, M. et al. (Nov. 2019). "The MUSE Ultra Deep Field (MUDF). II. Survey design and the gaseous properties of galaxy groups at $0.5 < z < 1.5$." In: *MNRAS* 490. ADS Bibcode: 2019MNRAS.490.1451F, pp. 1451–1469. DOI: 10.1093/mnras/stz2693.

Francis, Paul J. et al. (Oct. 1992). "An Objective Classification Scheme for QSO Spectra." In: *ApJ* 398, p. 476. DOI: 10.1086/171870.

Freedman, Wendy L. et al. (May 2001). "Final Results from the Hubble Space Telescope Key Project to Measure the Hubble Constant." In: *ApJ* 553. ADS Bibcode: 2001ApJ...553...47F, pp. 47–72. DOI: 10.1086/320638.

Gaia Collaboration, Gaia et al. (Aug. 2018). "Gaia Data Release 2. Summary of the contents and survey properties." en. In: *A&A* 616, A1. DOI: 10.1051/0004-6361/201833051.

García-Vergara, Cristina et al. (Oct. 2017). "Strong Clustering of Lyman Break Galaxies around Luminous Quasars at $z\sim4$." In: *ApJ* 848. ADS Bibcode: 2017ApJ...848....7G, p. 7. DOI: 10.3847/1538-4357/aa8b69.

García-Vergara, Cristina et al. (Dec. 2019). "Clustering of Lyα Emitters around Quasars at $z \sim 4$." In: *ApJ* 886, p. 79. DOI: 10.3847/1538-4357/ab4d5210.48550/arXiv.1904.05894.

García-Vergara, Cristina et al. (Mar. 2022). "ALMA Reveals a Large Overdensity and Strong Clustering of Galaxies in Quasar Environments at z 4." en. In: *ApJ* 927.1, p. 65. DOI: 10.3847/1538-4357/ac469d.

Gasperin, F de, H T Intema, and D A Frail (Mar. 2018). "A radio spectral index map and catalogue at 147–1400 MHz covering 80 per cent of the sky." en. In: *MNRAS* 474.4, pp. 5008–5022. DOI: 10.1093/mnras/stx3125.

Gehrels, N. (Apr. 1986). "Confidence Limits for Small Numbers of Events in Astrophysical Data." In: *ApJ* 303, p. 336. DOI: 10.1086/164079.

Ghisellini, G. et al. (Feb. 2010). "General physical properties of bright Fermi blazars: Properties of bright Fermi blazars." en. In: *MNRAS* 402.1, pp. 497–518. DOI: 10.1111/j.1365-2966.2009.15898.x.

Ghisellini, G. et al. (June 2015). "SDSS J013127.34–032100.1: a candidate blazar with an 11 billion solar mass black hole at z = 5.18." en. In: *MNRASL* 450.1, pp. L34–L38. DOI: 10.1093/mnrasl/slv042.

Gloudemans, A. J. et al. (Dec. 2022). "Discovery of 24 radio-bright quasars at $4.9 \lesssim z \lesssim 6.6$ using low-frequency radio observations." en. In: *A&A* 668, A27. DOI: 10.1051/0004-6361/202244763.

Goto, Tomotsugu et al. (Sept. 2017). "No Lya emitters detected around a QSO at z = 6.4: Suppressed by the QSO?" In: *MNRAS* 470, pp. L117–L121. DOI: 10.1093/mnrasl/slx088.

Greig, Bradley et al. (Apr. 2017). "Lya emission-line reconstruction for high-z QSOs." In: *MNRAS* 466, pp. 1814–1838. DOI: 10.1093/mnras/stw3210.

Greiner, J. et al. (Oct. 2021). "Quasar clustering at redshift 6." en. In: *A&A* 654, A79. DOI: 10.1051/0004-6361/202140790.

Gullikson, Kevin, Sarah Dodson-Robinson, and Adam Kraus (Aug. 2014). "CORRECTING FOR TELLURIC ABSORPTION: METHODS, CASE STUDIES, AND RELEASE OF THE TelFit CODE." en. In: *AJ* 148.3, p. 53. DOI: 10.1088/0004-6256/148/3/53.

Gunn, James E. and Bruce A. Peterson (Nov. 1965). "On the Density of Neutral Hydrogen in Intergalactic Space." In: *ApJ* 142, pp. 1633–1636. DOI: 10.1086/148444.

Gupta, N. et al. (Mar. 2022). "H i Gas Playing Hide-and-seek around a Powerful FRI-type Quasar at z = 2.1." en. In: *ApJL* 927.2, p. L24. DOI: 10.3847/2041-8213/ac589f.

Guth, Alan H. (Jan. 1981). "Inflationary universe: A possible solution to the horizon and flatness problems." In: *Phys. Rev. D* 23.2, pp. 347–356. DOI: 10.1103/PhysRevD.23.347.

Habouzit, Mélanie et al. (Feb. 2016a). "Black hole formation and growth with non-Gaussian primordial density perturbations." In: *MNRAS* 456, pp. 1901–1912. DOI: 10.1093/mnras/stv2740.

Habouzit, Mélanie et al. (Nov. 2016b). "On the number density of 'direct collapse' black hole seeds." In: *MNRAS* 463, pp. 529–540. DOI: 10.1093/mnras/stw1924.

Habouzit, Mélanie et al. (Oct. 2019). "The diverse galaxy counts in the environment of high-redshift massive black holes in Horizon-AGN." In: *MNRAS* 489.1, pp. 1206–1229. DOI: 10.1093/mnras/stz2105.

Haiman, Z. and Renyue Cen (Jan. 2001). "Probing the End of the Dark Age: Quasar Strömgren Spheres Before Cosmological Reionization." In: *ASPC* 222, p. 101.

Hansen, Matthew and S. Peng Oh (Apr. 2006). "Lyman alpha radiative transfer in a multiphase medium." In: *MNRAS* 367.3, pp. 979–1002. DOI: 10.1111/j.1365-2966.2005.09870.x.

Harikane, Yuichi et al. (Oct. 2019). "SILVERRUSH. VIII. Spectroscopic Identifications of Early Large-scale Structures with Protoclusters over 200 Mpc at $z \sim 6-7$: Strong Associations of Dusty Star-forming Galaxies." In: *ApJ* 883, p. 142. DOI: 10.3847/1538-4357/ab2cd5.

Hazard, C., M. B. Mackey, and A. J. Shimmins (Mar. 1963). "Investigation of the Radio Source 3C 273 By The Method of Lunar Occultations." In: *Nature* 197, pp. 1037–1039. DOI: 10.1038/1971037a0.

Heavens, A. F. and K. Meisenheimer (Mar. 1987). "Particle acceleration in extragalactic sources : the role of synchrotron losses in determining the spectrum." In: *MNRAS* 225, pp. 335–353. DOI: 10.1093/mnras/225.2.335.

Herrera-Camus, R. et al. (Feb. 2015). "[C II] 158 μm Emission as a Star Formation Tracer." In: *ApJ* 800, p. 1. DOI: 10.1088/0004-637X/800/1/1.

Horne, K. (June 1986). "AN OPTIMAL EXTRACTION ALGORITHM FOR CCD SPECTROSCOPY." en. In: *PASP* 98.604. Publisher: IOP Publishing, p. 609. DOI: 10.1086/131801.

Hurley-Walker, N. et al. (Jan. 2017). "GaLactic and Extragalactic All-sky Murchison Widefield Array (GLEAM) survey – I. A low-frequency extragalactic catalogue." en. In: *MNRAS* 464.1, pp. 1146–1167. DOI: 10.1093/mnras/stw2337.

Hutchison, Taylor A. et al. (July 2019). "Near-infrared Spectroscopy of Galaxies During Reionization: Measuring C III] in a Galaxy at z = 7.5." In: *ApJ* 879, p. 70. DOI: 10.3847/1538-4357/ab22a2.

Ighina, L. et al. (Oct. 2019). "X-ray properties of z > 4 blazars." In: *MNRAS* 489, pp. 2732–2745. DOI: 10.1093/mnras/stz2340.

Ighina, L. et al. (Jan. 2021). "Radio Detection of VIK J2318$-$3113, the Most Distant Radio-Loud Quasar (z=6.44)." In: *A&A* 2101, p. L11.

Inayoshi, Kohei, Eli Visbal, and Zoltán Haiman (Aug. 2020). "The Assembly of the First Massive Black Holes." In: *ARA&A* 58, pp. 27–97. DOI: 10.1146/annurev-astro-120419-014455.

Inoue, Akio K. et al. (Aug. 2014). "An updated analytic model for attenuation by the intergalactic medium." In: *MNRAS* 442, pp. 1805–1820. DOI: 10.1093/mnras/stu936.

Intema, H. T. et al. (Feb. 2017). "The GMRT 150 MHz all-sky radio survey: First alternative data release TGSS ADR1." en. In: *A&A* 598, A78. DOI: 10.1051/0004-6361/201628536.

Izumi, Takuma et al. (June 2018). "Subaru High-z Exploration of Low-Luminosity Quasars (SHELLQs). III. Star formation properties of the host galaxies at $z \gtrsim 6$ studied with ALMA." In: *PASJ* 70, p. 36. DOI: 10.1093/pasj/psy026.

Jaffe, W. J. and G. C. Perola (Aug. 1973). "Dynamical Models of Tailed Radio Sources in Clusters of Galaxies." en. In: *A&A* 26, p. 423.

James, A. et al. (Sept. 2002). "SCUBA observations of galaxies with metallicity measurements: a new method for determining the relation between submillimetre luminosity and dust mass." en. In: *MNRAS* 335.3, pp. 753–761. DOI: 10.1046/j.1365-8711.2002.05660.x.

Jiang, Linhua et al. (Dec. 2020). "Evidence for GN-z11 as a luminous galaxy at redshift 10.957." en. In: *Nat Astron*. DOI: 10.1038/s41550-020-01275-y.

Jolley, E. J. D. and Z. Kuncic (May 2008). "Jet-enhanced accretion growth of supermassive black holes." en. In: *MNRAS* 386.2, pp. 989–994. DOI: 10.1111/j.1365-2966.2008.13082.x.

Jones, T. W., Dongsu Ryu, and Andrew Engel (Feb. 1999). "Simulating Electron Transport and Synchrotron Emission in Radio Galaxies: Shock Acceleration and Synchrotron Aging in Axisymmetric Flows." In: *ApJ* 512, pp. 105–124. DOI: 10.1086/306772.

Kaiser, C. R. (Oct. 2000). "The environments and ages of extragalactic radio sources inferred from multi-frequency radio maps." In: *A&A* 362. ADS Bibcode: 2000A&A...362..447K pp. 447–464. DOI: 10.48550/arXiv.astro-ph/0007261.

Kardashev, N. S. (Dec. 1962). "Nonstationarity of Spectra of Young Sources of Nonthermal Radio Emission." In: *Soviet Astronomy* 6, p. 317.

Kaviraj, S. et al. (Jan. 2017). "The Horizon-AGN simulation: evolution of galaxy properties over cosmic time." en. In: *MNRAS* 467, p. 4739. DOI: 10.1093/mnras/stx126.

Keating, Laura C. et al. (Nov. 2015). "Probing the end of reionization with the near zones of z > 6 QSOs." In: *MNRAS* 454, pp. 681–697. DOI: 10.1093/mnras/stv2020.

Kellermann, K. I. et al. (Oct. 1989). "VLA observations of objects in the Palomar Bright Quasar Survey." en. In: *AJ* 98, p. 1195. DOI: 10.1086/115207.

Kennicutt, Robert C. (Sept. 1998). "STAR FORMATION IN GALAXIES ALONG THE HUBBLE SEQUENCE." en. In: *ARA&A* 36.1, pp. 189–231. DOI: 10.1146/annurev.astro.36.1.189.

Kennicutt, Robert C. and Neal J. Evans (Sept. 2012). "Star Formation in the Milky Way and Nearby Galaxies." en. In: *ARA&A* 50.1, pp. 531–608. DOI: 10.1146/annurev-astro-081811-125610.

Khusanova, Y. et al. (Aug. 2022). "The [CII] and FIR properties of z > 6 radio-loud quasars." en. In: *A&A* 664, A39. DOI: 10.1051/0004-6361/202243660.

Klessen, Ralf S. and Simon C. O. Glover (Mar. 2023). "The first stars: formation, properties, and impact." In: *2023arXiv230312500*. DOI: Publication Title: arXiv e-prints ADS Bibcode: 2023arXiv230312500K Type: article. DOI: 10.48550/arXiv.2303.12500.

Kokorev, V. et al. (Dec. 2022). "ALMA Lensing Cluster Survey: Hubble Space Telescope and Spitzer Photometry of 33 Lensed Fields Built with CHArGE." In: *ApJS* 263, p. 38. DOI: 10.3847/1538-4365/ac9909.

Kormendy, John and Luis C. Ho (Aug. 2013). "Coevolution (Or Not) of Supermassive Black Holes and Host Galaxies." en. In: *ARA&A* 51.1, pp. 511–653. DOI: 10.1146/annurev-astro-082708-101811.

Laing, R. A. et al. (Dec. 2008). "Structures of the magnetoionic media around the Fanaroff-Riley Class I radio galaxies 3C31 and Hydra A." In: *MNRAS* 391, pp. 521–549. DOI: 10.1111/j.1365-2966.2008.13895.x.

Larson, Rebecca L. et al. (Mar. 2023). "A CEERS Discovery of an Accreting Supermassive Black Hole 570 Myr after the Big Bang: Identifying a Progenitor of Massive z > 6 Quasars." In: *2023arXiv230308918L*. DOI: 10.48550/arXiv.2303.08918.

Leahy, J. P. (Jan. 1991). *Interpretation of large scale extragalactic jets*. Vol. 19. Cambridge University Press.

Leipski, C. et al. (Apr. 2014). "SPECTRAL ENERGY DISTRIBUTIONS OF QSOs AT $z > 5$: COMMON ACTIVE GALACTIC NUCLEUS-HEATED DUST AND OCCASIONALLY STRONG STAR-FORMATION." en. In: *ApJ* 785.2, p. 154. DOI: 10.1088/0004-637X/785/2/154.

Ligo Collaboration, The LIGO Scientific et al. (Mar. 2015). "Advanced LIGO." en. In: *Class. Quantum Grav.* 32.7. Publisher: IOP Publishing, p. 074001. DOI: 10.1088/0264-9381/32/7/074001.

Liu, Yuanqi et al. (Feb. 2021). "Constraining the Quasar Radio-loud Fraction at z $\sim$ 6 with Deep Radio Observations." en. In: *ApJ* 908.2, p. 124. DOI: 10.3847/1538-4357/abd3a8.

Loeb, Abraham and Rennan Barkana (2001). "The Reionization of the Universe by the First Stars and Quasars." In: *ARA&A* 39.1, pp. 19–66. DOI: 10.1146/annurev.astro.39.1.19.

Lynds, Roger (Mar. 1971). "The Absorption-Line Spectrum of 4c 05.34." In: *ApJ* 164, p. L73. DOI: 10.1086/180695.

Machalski, J., M. Jamrozy, and D. J. Saikia (May 2009). "A multifrequency study of giant radio sources - III. Dynamical age versus spectral age of the lobes of selected sources." In: *MNRAS* 395, pp. 812–822. DOI: 10.1111/j.1365-2966.2009.14516.x.

Madau, Piero and Mark Dickinson (Aug. 2014). "Cosmic Star-Formation History." en. In: *ARA&A* 52, p. 415. DOI: 10.1146/annurev-astro-081811-125615.

Madau, Piero and Martin J. Rees (Oct. 2000). "The Earliest Luminous Sources and the Damping Wing of the Gunn-Peterson Trough." In: *ApJ* 542. ADS Bibcode: 2000ApJ...542L..69M, pp. L69–L73. DOI: 10.1086/312934.

Mahatma, Vijay H. et al. (Feb. 2020). "Investigating the spectral age problem with powerful radio galaxies." In: *MNRAS* 491, pp. 5015–5034. DOI: 10.1093/mnras/stz3396.

Malhotra, S. et al. (Nov. 2001). "Far-Infrared Spectroscopy of Normal Galaxies: Physical Conditions in the Interstellar Medium." en. In: *ApJ* 561.2, p. 766. DOI: 10.1086/323046.

Mandel, Eric and Alexey Vikhlinin (Oct. 2018). "Ericmandel/Js9: V2.2 Supports Synchronized Images, Separate/Gather Images, Mosaic Images, User-Defined And Mac-Style Menus, Coordinate Grids." In: *Zenodo*. DOI: 10.5281/zenodo.1453307.

Marshall, M. A. et al. (Sept. 2020). "Limits to Rest-frame Ultraviolet Emission from Far-infrared-luminous $z \sim 6$ Quasar Hosts." en. In: *ApJ* 900.1, p. 21. DOI: 10.3847/1538-4357/abaa4c.

Matsuoka, Yoshiki et al. (Oct. 2019). "Subaru High-z Exploration of Low-luminosity Quasars (SHELLQs). X. Discovery of 35 Quasars and Luminous Galaxies at $5.7 \lesssim z \lesssim 7.0$." In: *ApJ* 883, p. 183. DOI: 10.3847/1538-4357/ab3c60.

Mazzucchelli, C. et al. (Jan. 2017a). "No Overdensity of Lyman-Alpha Emitting Galaxies around a Quasar at $z\sim5.7$." In: *ApJ* 834, p. 83. DOI: 10.3847/1538-4357/834/1/83.

Mazzucchelli, C. et al. (Nov. 2017b). "Physical Properties of 15 Quasars at $ z \gtrsim 6.5$." en. In: *ApJ* 849.2, p. 91. DOI: 10.3847/1538-4357/aa9185.

Mazzucchelli, C. et al. (Aug. 2019). "Spectral Energy Distributions of Companion Galaxies to $z sim 6$ Quasars." en. In: *ApJ* 881.2, p. 163. DOI: 10.3847/1538-4357/ab2f75.

McGreer, Ian D. et al. (Mar. 2016). "A Constraint on Quasar Clustering at z = 5 from a Binary Quasar." In: *AJ* 151, p. 61. DOI: 10.3847/0004-6256/151/3/61.

McKinnon, Mark et al. (Sept. 2019). "ngVLA: The Next Generation Very Large Array." In: *BAAS* 51. \, p. 81.

McMullin, J P et al. (Oct. 2007). "CASA Architecture and Applications." en. In: *Astronomical Data Analysis Software and Systems XVI ASP Conference Series, Vol. 376, proceedings of the conference held 15-18 October 2006 in Tucson, Arizona, USA. Edited by Richard A. Shaw, Frank Hill and David J. Bell., p.127*. Astronomical Society of the Pacific Conference Series 376, p. 127.

McQuinn, Matthew (2016). "The Evolution of the Intergalactic Medium." In: *ARA&A* 54.1. _eprint: https://doi.org/10.1146/annurev-astro-082214-122355, pp. 313–362. DOI: 10.1146/annurev-astro-082214-122355.

Mechtley, M. et al. (Sept. 2012). "Near-infrared Imaging of a z = 6.42 Quasar Host Galaxy with the Hubble Space Telescope Wide Field Camera 3." In: *ApJL* 756, p. L38. DOI: 10.1088/2041-8205/756/2/L38.

Meisenheimer, K. et al. (July 1989). "The synchrotron spectra of radio hot spots." In: *A&A* 219, pp. 63–86.

Meyer, Romain A. et al. (Mar. 2022). "Constraining Galaxy Overdensities around Three z 6.5 Quasars with ALMA and MUSE." In: *ApJ* 927, p. 141. DOI: 10.3847/1538-4357/ac4f67.

Mignoli, Marco et al. (Oct. 2020). "Web of the giant: Spectroscopic confirmation of a large-scale structure around the z = 6.31 quasar SDSS J1030+0524." en. In: *A&A* 642, p. L1. DOI: 10.1051/0004-6361/202039045.

Momjian, Emmanuel et al. (July 2018). "Resolving the Powerful Radio-loud Quasar at z{\ensuremath{\sim}} 6." en. In: *ApJ* 861.2, p. 86. DOI: 10.3847/1538-4357/aac76f.

Morishita, T. et al. (Nov. 2018). "The Bright-end Galaxy Candidates at $z \sim 9$ from 79 Independent HST Fields." In: *ApJ* 867, p. 150. DOI: 10.3847/1538-4357/aae68c.

Morselli, L. et al. (Aug. 2014). "Primordial environment of super massive black holes: large-scale galaxy overdensities around $z \sim 6$ quasars with LBT." en. In: *A&A* 568, A1. DOI: 10.1051/0004-6361/201423853.

Myers, S. T. and S. R. Spangler (Apr. 1985). "Synchrotron aging in the lobes of luminous radio galaxies." In: *ApJ* 291, pp. 52–62. DOI: 10.1086/163040.

Namikawa, Toshiya (Mar. 2018). "Constraints on patchy reionization from Planck CMB temperature trispectrum." In: *Phys. Rev. D* 97.6, p. 063505. DOI: 10.1103/PhysRevD.97.063505.

Nanni, R. et al. (July 2018). "The 500 ks Chandra observation of the z = 6.31 QSO SDSS J1030 + 0524." en. In: *A&A* 614, A121. DOI: 10.1051/0004-6361/201832694.

Neeleman, Marcel and J. Xavier Prochaska (Feb. 2021). "qubefit: Small documentation updates." In: DOI: 10.5281/zenodo.4534407.

Neeleman, Marcel et al. (Mar. 2017). "[C II] 158-μm emission from the host galaxies of damped Lyman-alpha systems." In: *Science* 355, pp. 1285–1288. DOI: 10.1126/science.aal1737.

Neeleman, Marcel et al. (Jan. 2019). "[C II] 158 μm Emission from $z \sim 4$ H I Absorption-selected Galaxies." In: *ApJ* 870, p. L19. DOI: 10.3847/2041-8213/aaf871.

Neeleman, Marcel et al. (Apr. 2021). "The Kinematics of z $\gtrsim$ 6 Quasar Host Galaxies." en. In: *ApJ* 911.2, p. 141. DOI: 10.3847/1538-4357/abe70f.

Nielsen, Nikole M. et al. (Dec. 2018). "MAGIICAT VI. The Mg II Intragroup Medium Is Kinematically Complex." In: *ApJ* 869. ADS Bibcode: 2018ApJ...869..153N, p. 153. DOI: 10.3847/1538-4357/aaedbd.

Novak, Gregory S., Jeremiah P. Ostriker, and Luca Ciotti (Aug. 2011). "Feedback from Central Black Holes in Elliptical Galaxies: Two-dimensional Models Compared to One-dimensional Models." In: *ApJ* 737, p. 26. DOI: 10.1088/0004-637X/737/1/26.

Novak, Mladen et al. (Aug. 2019). "An ALMA Multiline Survey of the Interstellar Medium of the Redshift 7.5 Quasar Host Galaxy J1342+0928." en. In: *ApJ* 881.1, p. 63. DOI: 10.3847/1538-4357/ab2beb.

Novak, Mladen et al. (Nov. 2020). "No Evidence for [C ii] Halos or High-velocity Outflows in z {\ensuremath{\gtrsim}} 6 Quasar Host Galaxies." en. In: *ApJ* 904.2, p. 131. DOI: 10.3847/1538-4357/abc33f.

Oesch, P. A. et al. (Aug. 2013). "Probing the Dawn of Galaxies at z ~ 9-12: New Constraints from HUDF12/XDF and CANDELS data." In: *ApJ* 773, p. 75. DOI: 10.1088/0004-637X/773/1/75.

Oesch, P. A. et al. (May 2014). "The Most Luminous $z \sim 9-10$ Galaxy Candidates Yet Found: The Luminosity Function, Cosmic Star-formation Rate, and the First Mass Density Estimate at 500 Myr." In: *ApJ* 786, p. 108. DOI: 10.1088/0004-637X/786/2/108.

Oesch, P. A. et al. (Mar. 2016). "A REMARKABLY LUMINOUS GALAXY AT $Z = 11.1$ MEASURED WITH *HUBBLE SPACE TELESCOPE* GRISM SPECTROSCOPY." en. In: *ApJ* 819.2, p. 129. DOI: 10.3847/0004-637X/819/2/129.

Onoue, Masafusa et al. (Aug. 2020). "No Redshift Evolution in the Broad-line-region Metallicity up to z = 7.54: Deep Near-infrared Spectroscopy of ULAS J1342+0928." In: *ApJ* 898, p. 105. DOI: 10.3847/1538-4357/aba193.

Ostriker, Jeremiah P. et al. (Oct. 2010). "Momentum Driving: Which Physical Processes Dominate Active Galactic Nucleus Feedback?" In: *ApJ* 722. ADS Bibcode: 2010ApJ...722..642O, pp. 642–652. DOI: 10.1088/0004-637X/722/1/642.

Ota, Kazuaki et al. (Apr. 2018). "Large-scale Environment of a z = 6.61 Luminous Quasar Probed by Lya Emitters and Lyman Break Galaxies." In: *ApJ* 856, p. 109. DOI: 10.3847/1538-4357/aab35b.

Overzier, Roderik A. (Nov. 2016). "The realm of the galaxy protoclusters. A review." en. In: *A&AR* 24.1, p. 14. DOI: 10.1007/s00159-016-0100-3.

Overzier, Roderik A. (Feb. 2022). "Conditions for Direct Black Hole Seed Collapse near a Radio-loud Quasar 1 Gyr after the Big Bang." In: *ApJ* 926, p. 114. DOI: 10.3847/1538-4357/ac448c.

Overzier, Roderik A. et al. (Apr. 2009). "LCDM predictions for galaxy protoclusters - I. The relation between galaxies, protoclusters and quasars at z ~ 6." In: *MNRAS* 394, pp. 577–594. DOI: 10.1111/j.1365-2966.2008.14264.x.

Pacholczyk, A. G. (1970). "Radio astrophysics. Nonthermal processes in galactic and extragalactic sources." In: *Series of Books in Astronomy and Astrophysics, San Francisco: Freeman, 1970*.

Palmese, A. et al. (Jan. 2023). "A Standard Siren Measurement of the Hubble Constant Using Gravitational-wave Events from the First Three LIGO/Virgo Observing Runs and the DESI Legacy Survey." In: *ApJ* 943, p. 56. DOI: 10.3847/1538-4357/aca6e3.

Papovich, C. et al. (June 2016). "The Spitzer-HETDEX Exploratory Large-area Survey." In: *ApJS* 224. ADS Bibcode: 2016ApJS..224...28P, p. 28. DOI: 10.3847/0067-0049/224/2/28.

Peebles, P. J. E. (Jan. 1993). *Principles of Physical Cosmology*. DOI: 10.1515/9780691206721.

Penzias, A. A. and R. W. Wilson (July 1965). "A Measurement of Excess Antenna Temperature at 4080 Mc/s." In: *ApJ* 142, pp. 419–421. DOI: 10.1086/148307.

Perley, R. A. and B. J. Butler (May 2017). "An Accurate Flux Density Scale from 50 MHz to 50 GHz." en. In: *ApJS* 230.1, p. 7. DOI: 10.3847/1538-4365/aa6df9.

Perlmutter, S. et al. (Jan. 1998). "Discovery of a supernova explosion at half the age of the Universe." en. In: *Nature* 391.6662. Number: 6662 Publisher: Nature Publishing Group, pp. 51–54. DOI: 10.1038/34124.

Persson, S. E. et al. (June 2013). "FourStar: The Near-Infrared Imager for the 6.5 m Baade Telescope at Las Campanas Observatory." en. In: *PASP* 125.928, pp. 654–682. DOI: 10.1086/671164.

Planck Collaboration, Collaboration et al. (Sept. 2020). "Planck 2018 results. VI. Cosmological parameters." en. In: *A&A* 641, A6. DOI: 10.1051/0004-6361/201833910.

Poudel, Suraj et al. (Jan. 2018). "Early metal enrichment of gas-rich galaxies at z = 5." In: *MNRAS* 473.3, pp. 3559–3572. DOI: 10.1093/mnras/stx2607.

Priddey, R. S. and R. G. McMahon (June 2001). "The far-infrared-submillimetre spectral energy distribution of high-redshift quasars." en. In: *MNRAS* 324.1, pp. L17–L22. DOI: 10.1046/j.1365-8711.2001.04548.x.

Prochaska, J. et al. (Dec. 2020). "PypeIt: The Python Spectroscopic Data Reduction Pipeline." In: *JOSS* 5, p. 2308. DOI: 10.21105/joss.02308.

Pâris, I. et al. (June 2011). "A principal component analysis of quasar UV spectra at z ~ 3." en. In: *A&A* 530, A50. DOI: 10.1051/0004-6361/201016233.

Pâris, Isabelle et al. (May 2018). "The Sloan Digital Sky Survey Quasar Catalog: Fourteenth data release." en. In: *A&A* 613, A51. DOI: 10.1051/0004-6361/201732445.

Ramos Almeida, Cristina and Claudio Ricci (Oct. 2017). "Nuclear obscuration in active galactic nuclei." In: *NatAs* 1, pp. 679–689. DOI: 10.1038/s41550-017-0232-z.

Ravindranath, Swara et al. (June 2020). "The Semiforbidden C III] λ1909 Emission in the Rest-ultraviolet Spectra of Green Pea Galaxies." In: *ApJ* 896, p. 170. DOI: 10.3847/1538-4357/ab91a5.

Reed, S. L. et al. (Aug. 2019). "Three new VHS-DES quasars at 6.7 < z < 6.9 and emission line properties at z > 6.5." In: *MNRAS* 487, pp. 1874–1885. DOI: 10.1093/mnras/stz134110.48550/arXiv.1901.07456.

Regan, John A et al. (July 2019). "Super-Eddington accretion and feedback from the first massive seed black holes." en. In: *MNRAS* 486.3, pp. 3892–3906. DOI: 10.1093/mnras/stz1045.

Retana-Montenegro, E. and H. J. A. Röttgering (Apr. 2017). "Probing the radio loud/quiet AGN dichotomy with quasar clustering." en. In: *A&A* 600, A97. DOI: 10.1051/0004-6361/201526433.

Riess, Adam G. et al. (Sept. 1998). "Observational Evidence from Supernovae for an Accelerating Universe and a Cosmological Constant." In: *AJ* 116, pp. 1009–1038. DOI: 10.1086/300499.

Riess, Adam G. et al. (Feb. 2021). "Cosmic Distances Calibrated to 1% Precision with Gaia EDR3 Parallaxes and Hubble Space Telescope Photometry of 75 Milky Way Cepheids Confirm Tension with LCDM." In: *ApJ* 908, p. L6. DOI: 10.3847/2041-8213/abdbaf.

Roberts-Borsani, Guido et al. (Mar. 2022). "The Physical Properties of Luminous $z \gtrsim 8$ Galaxies and Implications for the Cosmic Star Formation Rate Density from 0.35 deg2 of (Pure-)Parallel HST Observations." In: *The Astrophysical Journal* 927. ADS Bibcode: 2022ApJ...927..236R, p. 236. DOI: 10.3847/1538-4357/ac4803.

Robertson, B. E. et al. (Dec. 2022). "Discovery and properties of the earliest galaxies with confirmed distances." In: *2022arXiv221204480R*. DOI: Publication Title: arXiv e-prints ADS Bibcode: Type: article. DOI: 10.48550/arXiv.2212.04480.

Rojas-Ruiz, Sofía et al. (Mar. 2020). "Probing the Bright End of the Rest-frame Ultraviolet Luminosity Function at z = 8–10 with *Hubble* Pure-parallel Imaging." en. In: *ApJ* 891.2, p. 146. DOI: 10.3847/1538-4357/ab7659.

Rojas-Ruiz, Sofía et al. (Oct. 2021). "The Impact of Powerful Jets on the Far-infrared Emission of an Extreme Radio Quasar at z 6." In: *ApJ* 920, p. 150. DOI: 10.3847/1538-4357/ac1a13.

Romani, Roger W. et al. (July 2004). "Q0906+6930: The Highest Redshift Blazar." In: *ApJL* 610, pp. L9–L11. DOI: 10.1086/423201.

Rudnick, Lawrence, Debora M. Katz-Stone, and Martha C. Anderson (Feb. 1994). "Do Relativistic Electrons either Gain or Lose Energy, outside of Extragalactic Nuclei?" In: *ApJS* 90, p. 955. DOI: 10.1086/191931.

Ryden, Barbara (Jan. 2003). *Introduction to cosmology*.

Salmon, Brett et al. (Aug. 2018). "RELICS: A Candidate $z \sim 10$ Galaxy Strongly Lensed into a Spatially Resolved Arc." en. In: *ApJL* 864.1, p. L22. DOI: 10.3847/2041-8213/aadc10.

Salpeter, Edwin E. (Jan. 1955). "The Luminosity Function and Stellar Evolution." In: *ApJ* 121, p. 161. DOI: 10.1086/145971.

Sandage, Allan (May 1965). "The Existence of a Major New Constituent of the Universe: the Quasistellar Galaxies." In: *ApJ* 141, p. 1560. DOI: 10.1086/148245.

Sargsyan, L. et al. (June 2014). "STAR FORMATION RATES FROM [C II] 158 $\upmu$m AND MID-INFRARED EMISSION LINES FOR STARBURSTS AND ACTIVE GALACTIC NUCLEI." en. In: *ApJ* 790.1, p. 15. DOI: 10.1088/0004-637X/790/1/15.

Satyavolu, Sindhu et al. (May 2023). "The need for obscured supermassive black hole growth to explain quasar proximity zones in the epoch of reionization." In: *MNRAS* 521, pp. 3108–3126. DOI: 10.1093/mnras/stad729.

Sbarrato, T. et al. (Oct. 2012). "SDSS J102623.61+254259.5: the second most distant blazar at z = 5.3." In: *MNRAS* 426, pp. L91–L95. DOI: 10.1111/j.1745-3933.2012.01332.x.

Schindler, Jan-Torge et al. (Dec. 2022). "The Pan-STARRS1 $\mathbf{z>5.6}$ Quasar Survey: III. The $\mathbf{z\approx6}$ Quasar Luminosity Function." In: *ApJ* 2022arXiv221204179S.

Schlafly, Edward F. and Douglas P. Finkbeiner (Aug. 2011). "Measuring Reddening with Sloan Digital Sky Survey Stellar Spectra and Recalibrating SFD." In: *ApJ* 737, p. 103. DOI: 10.1088/0004-637X/737/2/103.

Schmidt, M. (Mar. 1963). "3C 273 : A Star-Like Object with Large Red-Shift." In: *Nature* 197, p. 1040. DOI: 10.1038/1971040a0.

Schmidt, M. and R. F. Green (June 1983). "Quasar evolution derived from the Palomar bright quasar survey and other complete quasar surveys." In: *ApJ* 269, pp. 352–374. DOI: 10.1086/161048.

Schöier, F. L. et al. (Mar. 2005). "An atomic and molecular database for analysis of submillimetre line observations." en. In: *A&A* 432.1, pp. 369–379. DOI: 10.1051/0004-6361:20041729.

Shao, Yali et al. (Aug. 2017). "Gas Dynamics of a Luminous z = 6.13 Quasar ULAS J1319+0950 Revealed by ALMA High-resolution Observations." In: *The Astrophysical Journal* 845. ADS Bibcode: 2017ApJ...845..138S, p. 138. DOI: 10.3847/1538-4357/aa826c.

Shao, Yali et al. (May 2019). "Star Formation and ISM Properties in the Host Galaxies of Three Far-infrared Luminous Quasars at $z \sim 6$." en. In: *ApJ* 876.2, p. 99. DOI: 10.3847/1538-4357/ab133d.

Shao, Yali et al. (Mar. 2022). "The radio spectral turnover of radio-loud quasars at z > 5." en. In: *A&A* 659, A159. DOI: 10.1051/0004-6361/202142489.

Shapley, Alice E. et al. (May 2003). "Rest-Frame Ultraviolet Spectra of z~3 Lyman Break Galaxies." In: *ApJ* 588, pp. 65–89. DOI: 10.1086/373922.

Simcoe, Robert A. et al. (Nov. 2020). "Interstellar and Circumgalactic Properties of an Unseen $z=6.84$ Galaxy: Abundances, Ionization, and Heating in the Earliest Known Quasar Absorber." In: *2020arXiv201110582S*.

Simpson, Chris et al. (Aug. 2014). "No excess of bright galaxies around the redshift 7.1 quasar ULAS J1120+0641." en. In: *MNRAS* 442.4, pp. 3454–3461. DOI: 10.1093/mnras/stu1116.

Somerville, Rachel S. et al. (Dec. 2008). "A semi-analytic model for the co-evolution of galaxies, black holes and active galactic nuclei." In: *MNRAS* 391, pp. 481–506. DOI: 10.1111/j.1365-2966.2008.13805.x.

Springel, Volker et al. (June 2005). "Simulations of the formation, evolution and clustering of galaxies and quasars." In: *Nature* 435, pp. 629–636. DOI: 10.1038/nature03597.

Sramek, R. A. and D. W. Weedman (June 1980). "The radio properties of optically discovered quasars." In: *ApJ* 238, pp. 435–444. DOI: 10.1086/158000.

Steidel, Charles C. et al. (Aug. 1996). "Spectroscopy of Lyman Break Galaxies in the Hubble Deep Field." In: *AJ* 112. ADS Bibcode: 1996AJ....112..352S, p. 352. DOI: 10.1086/118019.

Steidel, Charles C. et al. (Aug. 2016). "Reconciling the Stellar and Nebular Spectra of High-redshift Galaxies." In: *ApJ* 826, p. 159. DOI: 10.3847/0004-637X/826/2/159.

Suzuki, Nao (Mar. 2006). "Quasar Spectrum Classification with Principal Component Analysis (PCA): Emission Lines in the Lya Forest." en. In: *ApJS* 163.1, p. 110. DOI: 10.1086/499272.

Tacchella, Sandro et al. (Mar. 2022). "On the Stellar Populations of Galaxies at z = 9-11: The Growth of Metals and Stellar Mass at Early Times." In: *ApJ* 927, p. 170. DOI: 10.3847/1538-4357/ac4cad.

Taylor, Edward N. et al. (Dec. 2011). "Galaxy And Mass Assembly (GAMA): stellar mass estimates." In: *MNRAS* 418.3, pp. 1587–1620. DOI: 10.1111/j.1365-2966.2011.19536.x.

Thorne, Jessica E. et al. (Feb. 2022a). "Deep Extragalactic VIsible Legacy Survey (DEVILS): identification of AGN through SED fitting and the evolution of the bolometric AGN luminosity function." In: *MNRAS* 509. ADS Bibcode: 2022MNRAS.509.4940T, pp. 4940–4961. DOI: 10.1093/mnras/stab3208.

Thorne, Jessica et al. (Mar. 2022b). "AGN Unification Diagram." In: *Zenodo*. DOI: 10.5281/zenodo.6381013.

Tisanić, K. et al. (Jan. 2019). "The VLA-COSMOS 3 GHz Large Project: Average radio spectral energy distribution of highly star-forming galaxies." en. In: *A&A* 621, A139. DOI: 10.1051/0004-6361/201834002.

Tisanić, K. et al. (Nov. 2020). "The VLA-COSMOS 3 GHz Large Project: Average radio spectral energy distribution of active galactic nuclei." en. In: *A&A* 643, A51. DOI: 10.1051/0004-6361/201937114.

Tonry, J. L. et al. (May 2012). "THE Pan-STARRS1 PHOTOMETRIC SYSTEM." en. In: *ApJ* 750.2, p. 99. DOI: 10.1088/0004-637X/750/2/99.

Trenti, M. and M. Stiavelli (Apr. 2008). "Cosmic Variance and Its Effect on the Luminosity Function Determination in Deep High-z Surveys." In: *ApJ* 676, pp. 767–780. DOI: 10.1086/528674.

Trenti, M. et al. (Feb. 2011). "The Brightest of Reionizing Galaxies Survey: Design and Preliminary Results." In: *ApJ* 727, p. L39. DOI: 10.1088/2041-8205/727/2/L39.

Urry, C. Megan and Paolo Padovani (Sept. 1995). "Unified Schemes for Radio-Loud Active Galactic Nuclei." In: *PASP* 107, p. 803. DOI: 10.1086/133630.

Venemans, B. P. et al. (May 2012). "DETECTION OF ATOMIC CARBON [C II] 158 {\ensuremath{\mu}}m AND DUST EMISSION FROM A z = 7.1 QUASAR HOST GALAXY." en. In: *ApJL* 751.2, p. L25. DOI: 10.1088/2041-8205/751/2/L25.

Venemans, B. P. et al. (Dec. 2013). "Discovery of Three z > 6.5 Quasars in the VISTA Kilo-Degree Infrared Galaxy (VIKING) Survey." In: *ApJ* 779, p. 24. DOI: 10.1088/0004-637X/779/1/24.

Venemans, B. P. et al. (Mar. 2015). "The Identification of Z-dropouts in Pan-STARRS1: Three Quasars at 6.5< z< 6.7." In: *ApJ* 801, p. L11. DOI: 10.1088/2041-8205/801/1/L11.

Venemans, Bram P. et al. (Jan. 2016). "BRIGHT [C ii] AND DUST EMISSION IN THREE z > 6.6 QUASAR HOST GALAXIES OBSERVED BY ALMA." en. In: *ApJ* 816.1, p. 37. DOI: 10.3847/0004-637X/816/1/37.

Venemans, Bram P. et al. (Dec. 2017a). "Copious Amounts of Dust and Gas in a z = 7.5 Quasar Host Galaxy." en. In: *ApJL* 851.1, p. L8. DOI: 10.3847/2041-8213/aa943a.

Venemans, Bram P. et al. (Aug. 2017b). "Molecular Gas in Threez$\sim$ 7 Quasar Host Galaxies." en. In: *ApJ* 845.2, p. 154. DOI: 10.3847/1538-4357/aa81cb.

Venemans, Bram P. et al. (Oct. 2018). "Dust Emission in an Accretion-rate-limited Sample of z $\gtrsim$ 6 Quasars." en. In: *ApJ* 866.2, p. 159. DOI: 10.3847/1538-4357/aadf35.

Venemans, Bram P. et al. (Apr. 2019). "400 pc Imaging of a Massive Quasar Host Galaxy at a Redshift of 6.6." en. In: *ApJ* 874.2, p. L30. DOI: 10.3847/2041-8213/ab11cc.

Venemans, Bram P. et al. (Nov. 2020). "Kiloparsec-scale ALMA Imaging of [C ii] and Dust Continuum Emission of 27 Quasar Host Galaxies at z $\sim$ 6." en. In: *ApJ* 904.2, p. 130. DOI: 10.3847/1538-4357/abc563.

Volonteri, Marta, Mélanie Habouzit, and Monica Colpi (Sept. 2021). "The origins of massive black holes." In: *NatRP* 3, pp. 732–743. DOI: 10.1038/s42254-021-00364-9.

— (May 2023). "What if young z > 9 JWST galaxies hosted massive black holes?" In: *MNRAS* 521. ADS Bibcode: 2023MNRAS.521..241V, pp. 241–250. DOI: 10.1093/mnras/stad499.

Volonteri, Marta and Martin J. Rees (Oct. 2006). "Quasars at z=6: The Survival of the Fittest." In: *ApJ* 650, pp. 669–678. DOI: 10.1086/507444.

Volonteri, Marta, Joseph Silk, and Guillaume Dubus (May 2015). "THE CASE FOR SUPERCRITICAL ACCRETION ONTO MASSIVE BLACK HOLES AT HIGH REDSHIFT." en. In: *ApJ* 804.2, p. 148. DOI: 10.1088/0004-637X/804/2/148.

Wang, Feige et al. (Oct. 2019a). "Exploring Reionization-era Quasars. III. Discovery of 16 Quasars at $6.4 \lesssim z \lesssim 6.9$ with DESI Legacy Imaging Surveys and the UKIRT Hemisphere Survey and Quasar Luminosity Function at $z \sim 6.7$." en. In: *ApJ* 884.1, p. 30. DOI: 10.3847/1538-4357/ab2be5.

Wang, Feige et al. (Jan. 2021). "A Luminous Quasar at Redshift 7.642." In: *ApJ* 907, p. L1. DOI: 10.3847/2041-8213/abd8c6.

Wang, Ran et al. (July 2013). "STAR FORMATION AND GAS KINEMATICS OF QUASAR HOST GALAXIES ATz$\sim$ 6: NEW INSIGHTS FROM ALMA." en. In: *ApJ* 773.1, p. 44. DOI: 10.1088/0004-637X/773/1/44.

Wang, T. et al. (Aug. 2019b). "A dominant population of optically invisible massive galaxies in the early Universe." en. In: *Nature* 572.7768, pp. 211–214. DOI: 10.1038/s41586-019-1452-4.

Weiß, A. et al. (Oct. 2008). "LABOCA observations of nearby, active galaxies." en. In: *A&A* 490.1, pp. 77–86. DOI: 10.1051/0004-6361:200809909.

Willott, Chris J., Jacqueline Bergeron, and Alain Omont (Mar. 2015). "STAR FORMATION RATE AND DYNAMICAL MASS OF 108SOLAR MASS BLACK HOLE HOST GALAXIES AT REDSHIFT 6." en. In: *ApJ* 801.2, p. 123. DOI: 10.1088/0004-637X/801/2/123.

Wyithe, J. Stuart B., Abraham Loeb, and Chris Carilli (Aug. 2005). "Improved Constraints on the Neutral Intergalactic Hydrogen surrounding Quasars at Redshifts z > 6." In: *ApJ* 628, pp. 575–582. DOI: 10.1086/430874.

Yang, Jinyi et al. (June 2019). "Exploring Reionization-era Quasars. IV. Discovery of Six New z > 6.5 Quasars with DES, VHS, and unWISE Photometry." In: *ApJ* 157, p. 236. DOI: 10.3847/1538-3881/ab1be110.48550/arXiv.1811.11915.

Yang, Jinyi et al. (July 2020). "Pōniuā'ena: A Luminous z = 7.5 Quasar Hosting a 1.5 Billion Solar Mass Black Hole." In: *ApJ* 897, p. L14. DOI: 10.3847/2041-8213/ab9c26.

Yang, Jinyi et al. (Dec. 2021). "Probing Early Supermassive Black Hole Growth and Quasar Evolution with Near-infrared Spectroscopy of 37 Reionization-era Quasars at 6.3 < z < 7.64." In: *ApJ* 923, p. 262. DOI: 10.3847/1538-4357/ac2b3210.48550/arXiv.2109.13942.

Yip, C. W. et al. (Dec. 2004). "Spectral Classification of Quasars in the Sloan Digital Sky Survey: Eigenspectra, Redshift, and Luminosity Effects." en. In: *AJ* 128.6, p. 2603. DOI: 10.1086/425626.

Yue, Minghao et al. (Nov. 2021). "A Candidate Kiloparsec-scale Quasar Pair at z = 5.66." In: *ApJ* 921, p. L27. DOI: 10.3847/2041-8213/ac31a9.

Yun, Min S. and C. L. Carilli (Mar. 2002). "Radio–to–Far-Infrared Spectral Energy Distribution and Photometric Redshifts for Dusty Starburst Galaxies." en. In: *ApJ* 568.1, pp. 88–98. DOI: 10.1086/338924.

Zheng, W. et al. (Apr. 2006). "An Overdensity of Galaxies near the Most Distant Radio-loud Quasar*." en. In: *ApJ* 640.2, p. 574. DOI: 10.1086/500167.

Zheng, Zheng et al. (May 2010). "RADIATIVE TRANSFER MODELING OF Lya EMITTERS. I. STATISTICS OF SPECTRA AND LUMINOSITY." en. In: *ApJ* 716.1. Publisher: The American Astronomical Society, p. 574. DOI: 10.1088/0004-637X/716/1/574.

Zibetti, Stefano, Stéphane Charlot, and Hans-Walter Rix (Dec. 2009). "Resolved stellar mass maps of galaxies – I. Method and implications for global mass estimates." In: *MNRAS* 400.3, pp. 1181–1198. DOI: 10.1111/j.1365-2966.2009.15528.x.